Computations of extreme wave impact events on wave energy converter attached to coastal protection structures

Marc Batlle Martin

Normandie Université

THESE

Pour obtenir le diplôme de doctorat

Spécialité Mécanique des fluides

Préparée au sein de l'Université Le Havre Normandie

Computations of extreme wave impact events on wave energy converter attached to coastal protection structures

Présentée et soutenue par

Marc BATLLE MARTIN

Thèse soutenue publiquement le 06/07/2021 devant le jury composé de		
Mr Jeffrey Harris	Chargé de recherche (HDR), École nationale des ponts et chaussées	Rapporteur
Mr Philippe Sergent	Directeur de recherche, CEREMA	Rapporteur
Mr François Marin	Professeur, Université Le Havre Normandie, Le Havre	Examinateur
Mr Vicente Negro Valdecantos	Professeur des universités, Universidad Politécnica de Madrid, Espagne	Examinateur
Mr Javier L. Lara	Professeur des universités, Universidad de Cantabria, Espagne	Examinateur
Mme Julie Lebunetel	Docteure, Entreprise - Ingérop	Examinateur
Mr Julien Reveillon	Professeur, Université de Rouen Normandie	Co-directeur de thèse
Mr Grégory Pinon	Maître de conférences (HDR), Université Le Havre Normandie, Le Havre	Directeur de thèse

Thèse co-dirigée par Grégory PINON, **Laboratoire CNRS UMR 6294 LOMC, Université Le Havre Normandie et** Julien REVEILLON, **Laboratoire CNRS UMR 6614 CORIA, Université de Rouen Normandie**

UNIVERSITÉ LE HAVRE NORMANDIE

ED PSIME

LABORATOIRE ONDES et MILIEUX COMPLEXES

RÉGION NORMANDIE

Contents

Acknowledgements

This piece of work is the result of three years of personal efforts and cooperation with multiple individuals who deserve proper recognition. First, the person without whom this would not be possible in the first place, my PhD director, Grégory Pinon. His guidance and support were crucial all along this research period and his predisposition for debating freely the daily challenges was a great source of motivation. Secondly, my co-supervisor, Julien Reveillon, who was there anytime I required his advice without hesitation.

On the other hand, external collaborations have helped develop this work. Notably, Olivier Kimmoun gave me important remarks and points of view which I appreciated. Moreover, a collaboration with Javier L. Lara and Gabriel Barajas from IH Cantabria deeply improved the quality of this work and I am very thankful for their predisposition to help in my research. A special thanks to the atomisation team, François-Xavier Demoulin, Benjamin Duret, Javier Anez, from the laboratory CORIA who introduced me to research and OpenFOAM and were always excited to discuss my thoughts. It is also worth mentioning other colleagues from the research community who helped me in different ways such as Vicente Negro Valdecantos, Dominique Mouaze, Guillaume Carpentier, Matthias Kudella, Diego Vicinanza, Gregorio Iglesias, among others. I would also like to thanks all the scientists and the research scholars of the Laboratory which have also been extremely helpful towards me during this period.

I thank the referees and the jury of my thesis for the valuable time they have spent examining my manuscript. I would like to thank all the personal from Le Havre who participated in one way or another in the realization of this project. I am grateful to the Region Normandie for funding my PhD, and to Labex, CNRS and PERCUSS, for funding the various research expeditions during these last three years.

Finally, I would like to thank my mum Dolors, my dad Enric, my brother Carles and all the family for their unconditional support along this exciting journey. Also to all my old friends from Torroella de Montgri for their warm friendship which makes life easier. Last but not the least, a special thanks to my partner and best friend Esmeralda who has been there in the ups and downs, giving wise advice and sincere support.

Introduction

Favoured by climate change, the global mean sea level rose eleven to sixteen centimeters in the twentieth-century, C. Hay *et al.* 2015 [1]. Predictions for the actual century are more alarming, with an estimation of half a meter rise if immediate cuts to carbon emissions are adopted, see L. Jackson *et al.* 2016 [2], A. Nauels *et al.* 2017 [3], D. Le Bars *et al.* 2017 [4] or R. Kopp *et al.* 2017 [5]. For higher emissions scenarios, this century sea rise may exceed two meters. This critical situation will expose a dramatic portion of the population to unprecedented conditions. On the other hand, the maritime commerce is growing fast and is forcing a tendency to increase the ships size. Consequently, a bast numbers of international ports are facing difficulties to accomodate the largest vessels. Therefore, actual sea-side infrastructures will need a close eye revision and a rising governmental interest for defensive coastal construction is to be expected. A major question to answer for port planners is rather to expand the infrastructures in deeper waters or to improve existing ones. Such kinds of structures have a long life expectancy design and the cost for those projects may exceed the order of billions. The structural design has to be, then, precise and effective.

Coastal structures range from dikes, breakwater, jetties, docks, artificial beaches and reefs, among others. Each of them has its own purpose, but they all have in common a sheltering objective against the sea. However, near-shore as well as off-shore conditions are still at a certain point unpredictable and occurrence of certain conditions may lead to severe damages on the infrastructures. For example, the cyclone Xynthia in 2010, see P. Quevauviller *et al.* 2017 [6], or the stormy winter season of 2013-2014, see M. Priestley *et al.* 2017 [7], caused dramatic social and economic losses on the western coast of Europe. Among all the environmental forces acting on coastal or ocean structures, those resulting from breaking waves impact are most likely the cause of the highest local pressures.

Oscillating water column

The necessity of reinforcing and constructing new coastal defensive structures, together with the global emissions objectives to increase the renewable energy sources, has motivated the present study to evaluate the performance of an oscillating water column (OWC) device facing extreme sea states. An oscillating water column is a wave energy converter (WEC) which makes use of the potential energy of waves for controlling a piston type mechanism within a chamber and cause a turbine rotation producing clean energy, see Fig. 1. It can be integrated within a breakwater caisson, see G.E. Jarlan *et al.* 1961 [8], S. Takahashi *et al.* 1985 and 1988 [9, 10], F. He *et al.* 2016 [11] or D. Vicinanza *et al.* 2019 [12], allowing some cost sharing between the harbor protection and energy generation functions. This engineering structure has been already tested in Toftestallen (Norway), Sakata harbour (Japan), Pico Island in Açores (Portugal) (F. Neumann *et al.* 2011 [13], A. Falcão *et al.* 2020 [14]), Mutriku (Spain) (Y. Torre-Enciso *et al* 2009 [15]) or in Limpet,

Islay (UK), among others.

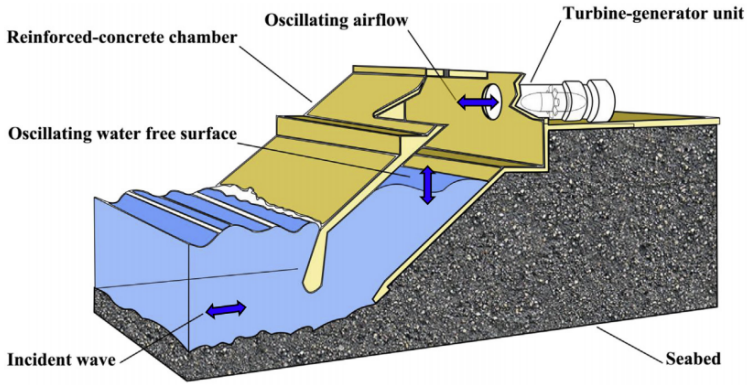

Figure 1: Sketch of an oscillating water column with axial turbine, extracted from [16]

From Fig. 1 it is easy to see the exposition of the front curtain wall making it a "fragile" part of such a massive structure. Experience from OWC prototypes deployments has shown that often the wave loads are underestimated on this kind of devices. And, this can lead to severe structural damages. For example: the disaster occurred on the PICO terminal in the Açores (see Fig. 2a) or the severe damage to four of the 16 OWC chambers, including the loss of the entire front wall of one chamber in Mutriku, Fig. 2b, see E. Medina-Lopez *et al.* 2015 [17]. These arise the necessity of revisiting the existing wave loads formulas for a proper assessment of the structure survivability. Moreover, there is a lack of quantitative experience when it comes to considering in-chamber loads which are most likely to occur during sloshing type situations.

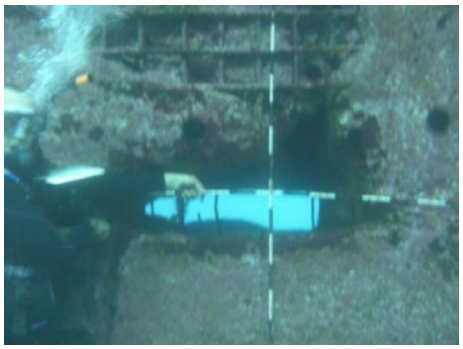

(a) OWC PICO, Portugal, extracted from F. Neumann *et al.* 2011 [13].

(b) OWC Mutriku, Spain, extracted from K. Pawitan *et al.* 2020 [18].

Figure 2: Examples of oscillating water column curtain wall damage

Breaking waves loads: an historical review

The prediction of wave loads has been a matter of interest for long time now. One of the first documentation of wave loading on caisson breakwaters dates from 1840 by T. Stevenson 1840 [19], where spring dynamometers and visual observation was employed on site at Dunbar, a UK harbour. At this time, it was already perceived the fact that when a water wave is not breaking, it will deflect upwards the vertical wall producing relatively

small pressure. It was G. Saintflou in 1928 [20] who proposed a first mathematical theory to calculate such kind of wave loads, which, at the time, were referred as *clapoti*. This kind of wave load rarely exceeds the intensity of the hydrostatic pressure corresponding to the wave height, i.e., $\rho g H$ being ρ the water density, g the gravitational acceleration and H the wave height. It wasn't until 1938, when stepped wave gauges and piezo-electric transducers were used by A. de Rouville *et al.* 1938 [21] in the port of Dieppe, France. During these in-situ experimental records, they verified the theoretical work presented by G. Saintflou. However, they also reported very large scale impact pressures attributed to violent waves impingement and they highlighted the localised and pulsating nature of this phenomenon.

The solid-fluid impact

In parallel, the study of a solid-fluid impact was also investigated from other perspectives, e.g. ditching or sloshing, and it is worth mentioning one of the first relevant studies by T. von Karmann in 1929 [22]. In his work he studied the water entry problem of a solid cone, see Fig. 3, and presented a theoretical description of the pressures related.

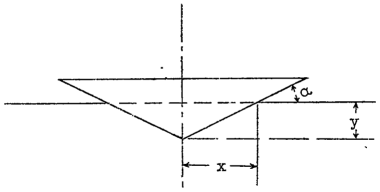

Figure 3: Original sketch of the water entry problem proposed by T. von Karmann in 1929 [22]

Continuing with the investigation carried out in Dieppe, these motivated to do controlled laboratory experiments and an initial attempt to calibrate an empirical model by R. A. Bagnold in 1939 [23]. In this work, the presence of air during a breaking wave impact was attributed as the major counterpoint for calculating the pressures related by using the water-hammer shock pressure theory. Bagnold made use of a piston type model to propose a first description of the air compression dynamics, Fig. 4a. During these experiments, it was also reported the difficult repeatability of apparently similar wave impacts, leading to wide number of different pressure records.

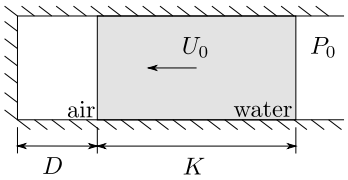

(a) Air compression model proposed by R. A. Bagnold

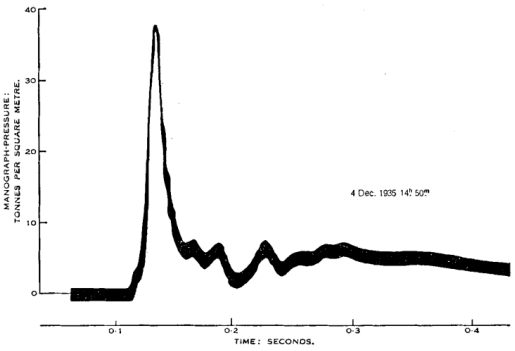

(b) In-situ wave impact pressure records in Dieppe, 1938

Figure 4: Images extracted from the report published by R. A. Bagnold in 1939 [23].

This was also reported by T. Hayashi *et al.* in 1958 [24] while in their work they also explored theoretically and experimentally the second pressure rebound of longer period after the "shock pressure", see Fig. 4b. More laboratory experimental investigations were carried out by D.F. Denny in 1951 [25] and J.R. Weggel *et al.* in 1970 [26] attempting to relate a fluid momentum length scale with the wave steepness to calculate the pressures exerted. The later, proposed a general rought relationship between the rise time (t_r) of the impulsive force and its magnitude (F_{imp}) reading

$$F_{imp} = a \cdot t_r^b \tag{1}$$

where a is an empirical coefficient and b en empirical exponent based on the experimental impact force. In 1966, H. Mitsuyasu [27] further developed the theory proposed by R.A. Bagnold to describe the dynamics of the air compression giving analytic solutions for the different conditions such as: small or finite compression of air.

General formulation for wave pressure on a caisson breakwater

In 1977, Yoshimi Goda published the first edition of *Random seas and design of maritime structures* in Japanese and it was translated in 1985 [28] with several re-editions. In this book, a revision of the relevant formulation for wave pressures exerted on upright sections of vertical breakwater was presented and it is still used as a guideline nowadays. The book also presented a general clarification of the types of failures modes for a vertical breakwater due to the waves action, Fig. 5.

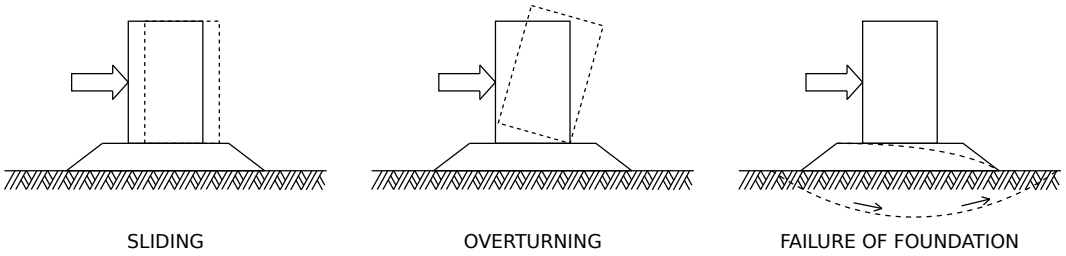

Figure 5: Modes of major failure of vertical breakwater

He pointed out the fact that impulsive breaking wave pressure of high intensity do not threaten the stability of the breakwater. However, in more recent editions, references to the work of Takahashi *et al.* 1993 [29] reported cases of steady sliding caissons, see Fig. 6, or breakage of a part of the front wall of caisson when unfavourable breaking conditions. These conditions are attributed to long berms or sea bottoms with steep slopes, which consequently may lead to plunging breakers. Takahashi extended the formulation proposed by Goda to take into account breaking waves effects.

Deep water breaking waves

The work of M.S. Longuet-Higgins *et al.* in 1976 [30] set a remarkable initial attempt to describe analytically the breaking process based on the potential flow. The increasing interest in off-shore structures inspired some authors to study the breaking wave loads phenomenon in deep water conditions. For example, S.S. Kjeldsen *et al.* in 1979 [31] studied experimentally deep water breaking waves loads on a suspended vertical plane. W.J. Easson *et al.* in 1984 [32] first employed laser-doppler anemometry to correlate the breaking wave fluid velocities with the impact force on an horizontal cylinder. Similarly,

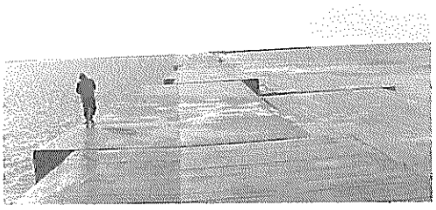

Figure 6: Slided caissons in Sakata Port. Image extracted from Takahashi *et al.* 1993 [29] giving courtesy to the 1st District Port Construction Bureau, MOT.

M.K. Ochi *et al.* 1984 [33] studied the deep water breaking wave impact on a vertical cylinder, proposing an empirical coefficient which related the pressure fields with the wave crest speed. These motivated the experiments of E.S. Chan *et al.* in 1988 [34] following similar techniques now using a vertical wall. The pressure records were much higher than the two previous studies and in the same order of magnitude with the experiments on shallow water conditions. In 1984, P.A. Blackmore *et al.* [35] published a report of field measurements of sea wave impact, where pressure values up to 10 times the hydrostatic head where recorded. Whereas, R.A. Bagnold [23] recorded much higher values up to 30 times the pressure head. This questioned the possibility to scale the laboratory results with prototypes.

Wave breaking air entrapment and classification of wave loads

In parallel with the physical experiments; theoretical and numerical studies to understand and model the wave-impact process started to flourish. Particularly, the computations by M.J. Cooker *et al.* in 1990 [36] using a potential boundary-integral code revealed that the most intense impacts in terms of pressure, similarly as it was measured by E.S. Chan *et al.* in 1988 [34], were generated by a breaking type enclosing small amount of air. This particular situation may occur when the wave front is almost flat and parallel to the wall. The model was further developed using the impulse theory by M.J. Cooker *et al.* in 1990 [37] and presented a semi-analytical solution for the impulse distribution for different relevant configurations. M. Hattori *et al.* in 1994 [38] used high-speed video to study the wave impact, putting special interest on the aforementioned wave impact with low air entrapment, see Fig. 7.

He attributed the reduction of pressure maximum value and the increase on the peak pressure rise time when large amounts of air are entrapped and highlighted the severity of the impact with low-aeration or air bubbles entrapment. His work also pointed out the lower pressure oscillations frequencies for large amount of air relating it to the resonant frequencies of the pulsating air pockets. According to H. Oumeraci *et al.* 1993 [39], the wave breaking shape was found to depend on three relevant parameters such as: the ratio of water depth breaking to the still water depth at the wall, the ratio of the horizontal velocity of the breaking wave to the vertical upward velocity of the water surface at the wall and the distance between the breaking point and the vertical wall boundary. Field measurements, reported by A.R. Crawford in 1999 [40] at the Alderney Breakwater, in the Channel Islands, used new measurement techniques and the experimental work of M.J.A. Walkden in 1999 [41] studied the effect of the water salinity as well as the presence of controlled aeration mixture.

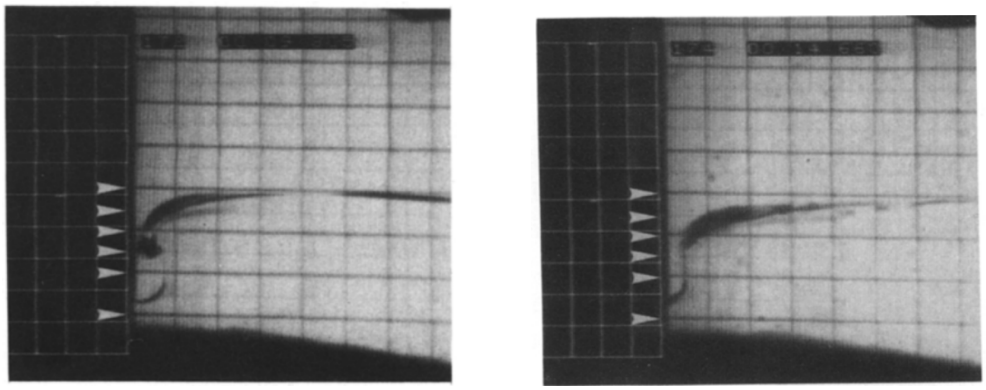

(a) Fully developed plunging breaker with a thick air pocket

(b) Plunging breaker with a thin air pocket

Figure 7: Images extracted from the experiments of M. Hattori *et al.* in 1994 [38]

Probabilistic design tools for vertical breakwaters

To the best of the author's knowledge, in 1996 the *Probabilistic design tools for vertical breakwaters* (PROVERS) project, started and ended up in 1999 by publishing a final report [42]. In this work, experimental analysis lead to a vastly known classification of the wave loads based on the force values rather than on the visual study, see Fig. 8.

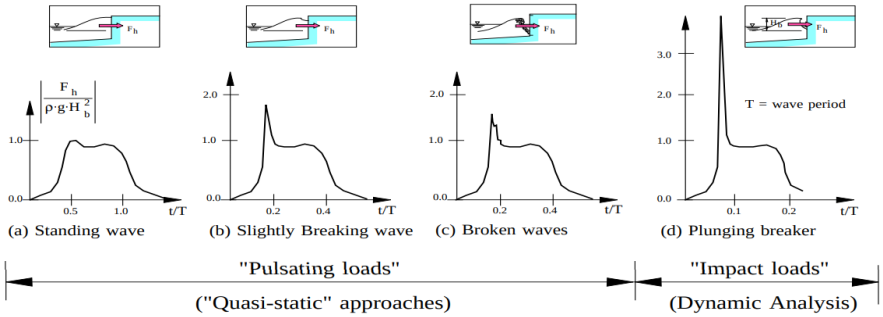

Figure 8: Distinction between "impact" and "pulsating" loads, extracted from [42]

This classification, distinguishes between the "pulsating" loads related to forces of lower magnitude than approximately 2 times the hydrostatic pressure head, and impact loads for which the duration/time history is most relevant for the dynamic response (vibrations) of the structure and which need the be handled with special care. Moreover, a description of the impact loads physics based on multiple experiments was presented, see Fig. 9. In this piece of work, it was also described a scaling procedure based on the separation of different components of the impact loads history, see upper right corner in Fig. 9. It was also remarked the importance of the amount of aeration and air entrapment to determine the compressibility of the impact fluid mixture.

After investigation by Bullock *et al.* of laboratory experiments [43, 44] and large scale experiments [45] a new classification was made for wave loads such as; slightly-breaking, low-aeration or flip-through, high-aeration or air-pocket and broken, see Fig. 10. This slightly differs from the one presented in PROVERS merging now together the so called standing wave and slightly breaking. Bullock reported very localised maximum pressure values for the impact close to the still water level and recorded pressure magnitudes up to

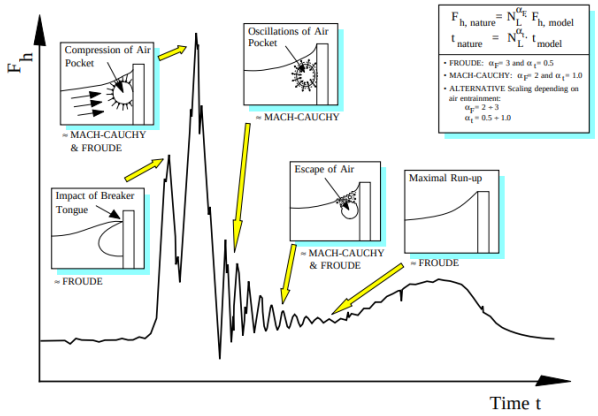

Figure 9: Physical processes involved in the wave impact load history and associated scaling problems, extracted from PROVERS [42]

150 times the wave height pressure head during a low-aerated impact.

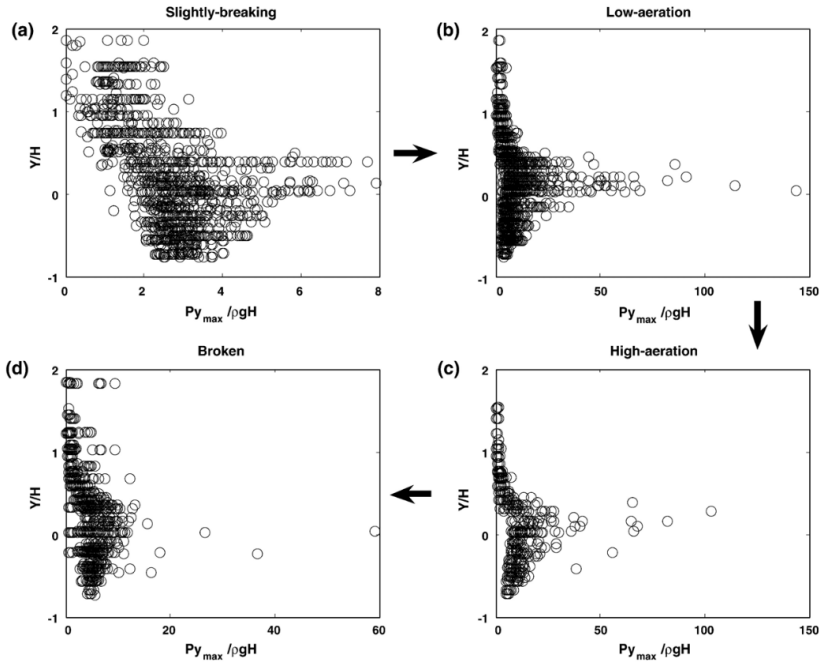

Figure 10: Classification of maximal pressures recorded during the experiments in the GWK by G.N. Bullock *et al.* in 2007 [45]. The pressure values are adimensionalised by the wave height hydrostatic component $Py_{max}/\rho gH$, where Py_{max} is the maximum pressure at each elevation y. (Note the different horizontal scales)

Breaking wave particle image velocimetry and recent work

The use of Particle Image Velocimetry (PIV) on the laboratory experimental work of O. Kimmoun *et al.* in 2009 [46] presented results of the phenomenon kinematics. In his work, it was reported quantitatively the surge of acceleration during a low aerated impact. According to C. Lugni *et al.* [47, 48], who used a sloshing depressurised tank, the flow evolution stages during an aerated impact are: the closure of the cavity onto the wall,

an isotropic compression/expansion of the cavity, an anisotropic compression/expansion and the rise of the air cavity up the wall. The ullage pressure demonstrated to be somehow proportional to the amount of air entrapped and the oscillations dampening largely dependant by the air leakage out of the cavity. More experimental work was carried out and reviewed by G. Cuomo *et al.* in 2010 [49] where existing formulae was revisited for calculating the impulsive force on the vertical wall. This new formula was based on the wave length and a parameter relating the water depth at the structure and the depth at breaking. Back in 2011, B. Hofland *et al.* [50] measured with relatively high spatial and temporal resolution large scale experiments of pressure fields on a vertical wall under wave impacts. A. Jensen in 2018 [51] made use of a solitary wave to study the flip-through impact utilising PIV in laboratory small scale experiments. Recent studies by T. Mai *et al.* in 2019 [52] using controlled aeration of the liquid using air injection reported a reduction of the pressure peak for impact cases, however, it was also reported the conservation of the impulse.

Computational coastal hydrodynamics

The last section presented a great historical effort for a proper evaluation of the wave loads, however, most of this experience was obtained on-site or experimentally. Recently, the workstations computational performance has grown exponentially allowing a new numerical perspective of the problematic. The water waves propagation and structure interaction initial progress was mainly developed using numerical algorithms based on the potential codes. For example, the Boundary Element Method (BEM) became specially popular due to its low computational requirements and is still of great use nowadays. Potential flows based models are extremely useful when dealing with wave propagation, involving refraction, diffraction and shoaling, and some popular examples are: FUNWAVE [53], COULWAVE [54], SWASH [55] among others. However, they present limitations derived from the assumption of the uniform (or piecewise linear) velocity profile along the water column, and, consequently, the modelling of vorticity, viscosity or two-phase effects is not recommended. This makes them a weak candidate for fluid-structure interaction problems, specially for plunging waves. Nevertheless, the wave overturning process is plausible and some authors explored new procedures to include the impact phenomenon, e.g. S. Zhang *et al.* 1996 [56] or B. Song *et al.* 2018 [57], among others. The fluid-solid impact process was also investigated using potential flows from other perspective, e.g. using the wedge entry configuration (N. de Divitiis *et al.* 2002 [58], G.D. Xu *et al.* 2010 [59]) or, as mentioned before, by simplifying the configuration similarly as M. Cooker [37] did.

Nonetheless, models based in the Navier-Stokes equations have demonstrated better capabilities for fluid structure interactions and, specifically, for breaking waves modelling. That is to say, by using much higher computational costs. This models make use of two main approaches depending on how the flow is treated, namely: Eulerian if the fluids are considered continuous in space. Or, Lagrangian, if the fluids are considered as an ensemble of different particles.

Eulerian Navier-Stokes models

The Reynolds Average Navier-Stokes (RANS) models consider the fluid as a continuous medium using highly nonlinear equations. This method makes use of a fixed mesh to solve and describe the fluid properties. In conjunction with the volume of fluid (VoF) method (see E. Berberovic *et al.* 2009 [60]) it can be easily extended for two-phase flows and many authors use it for marine hydrodynamics. Some of the most renown codes are:

Reef3D, Fluent, Star-CCM+, Neptune, ComFLOW or OpenFOAM (see H.G. Weller *et al.* 1998 [61]).

Wave generation in OpenFOAM

In the present work the open source CFD software `OpenFOAM` is used to model the numerical wave tank (NWT). This software have had a considerable effort by different authors to investigate most of the relevant process in coastal hydrodynamics. Firstly, the wave generation process has been developed by multiple perspectives and a recent general overview of the existing ones has been reported by C. Windt *et al.* in 2019 [62]. For example, N.G. Jacobsen *et al.* 2012 [63] in his work studied the relaxation zone technique where the waves are generated over a partition of the domain and can be absorbed using numerical "sponge layers". That said, P. Higuera *et al.* 2013 [64] introduced the static boundary condition for wave generation and absorption and also developed a "moving" boundary using a morphing mesh mimicking the experimental wave makers.

Wave propagation in OpenFOAM

On the other hand, some authors have focused on the propagation stage of water waves, for example, P.A. Wroniszewski *et al.* in 2014 [65] benchmarked the progression of a solitary wave using different navier-stokes codes. The work of B.T. Paulsen *et al.* 2014 [66] reported difficulties to maintain the wave heights for long propagation due to the numerical diffusion on the free surface. In his work, it was also reported the presence of spurious velocities near the interface which exacerbated the diffusion. Other authors out from the waves context, also reported the presence of these spurious velocities, e.g. S. Hysing 2006 [67] and this received considerably attention. More recent studies demonstrated developments on this direction, e.g. V. Vukčević *et al.* 2016 [68] pointing a momentum imbalance as the source. The wave propagation was also investigated, putting special interest on the different relevant numeric schemes, in the work of B.E. Larsen *et al.* 2018 [69]. Most of the aforementioned authors were also interested on the breaking process and their studies are extended on investigating the phenomenon, e.g. P. Higuera *et al.* 2013 [64], N. Jacobsen *et al.* 2014 [70] or G. Lupieri *et al.* 2015 [71]. Moreover, the turbulence mechanism have also been investigated by the community and recent studies apparently solved older issues related to the overproduction of turbulence near the interface B. Devolder 2017 [72] and B.E. Larsen *et al.* 2018 [73].

Breaking waves fluid-structure interaction using Eulerian Navier-Stokes codes

The breaking waves fluid-structure interaction has also been investigated before using Eulerian approaches. For example, Z.H. Ma *et al.* 2014 [74] used a compressible two-phase model to study a wide variety of impulsive configurations such as, a gravity-induced liquid piston, a free drop of a two-dimensional water column, water-air mixture shock tubes and also a plunging wave impact. According to his work, the air dynamics where out of the fluid incompressible assumption and remarked the necessity of a compressible solver. However, in this work, the simulated plunging wave induced pressures were not validated by experimental data. On the other hand, R. Wemmenhove *et al.* in 2015 [75] used the ComFLOW package using a two-phase compressible solver to study the sloshing internal loads with a newly gravity-consistent density averaging method. More recent studies further investigated in this direction and were of great interest for the present

work. For example, the work of I. Gatin *et al.* in 2020 [76] investigated the compressibility assumption for green sea loads using the newly developed Ghost Fluid Method to account for the interface jump. This was also employed for plunging waves interaction with a vertical wall by S. Liu *et al.* in 2019 [77] comparing the results with the experimental data of G.N. Bullock *et al.* 2007 [45].

Lagrangian Navier-Stokes models

This section introduces the Navier-Stokes models so-called Smooth Particle Hydrodynamics (SPH). These models do not depend on a mesh, eliminating certain numerical errors. The SPH methods were first developed for astronomical applications, such as galaxy collisions, and they present an inherent compressibility behaviour. On top of that, they are capable of handling high deformations of the interface which make them a great candidate for plunging waves modelling. However, they are high computational time consuming and not as developed as the previously introduced types for marine hydrodynamics.

The aforementioned advantages has pushed different authors to use them specially for breaking waves inducing impulsive loads. For example, P.M. Guilcher *et al.* 2010 [78] extended their previous work using a single fluid with SPH-flow enabling the treatment of interactions between several fluids. In his work several configurations where tested, such as: the gravity-induced liquid piston, which was compared with theoretical results J.F. Braeunig *et al.* 2009 [79]. Other authors compared incompressible and compressible models using Eulerian and Lagrangian methods during fluid impacts S. Marrone *et al.* 2015 [80]. However, their approach only accounted for one phase making it less relevant from a breaking waves perspective. Thus, the model was then extended to account for air dynamics and specifically compared with the single phase model S. Marrone *et al.* in 2016 [81]. More recently, X. Lu *et al.* 2021 [82] further studied the wave impact using single and two-phase phase model and coincided on the necessity to account for the light phase for aerated impacts.

Thesis outline

The rest of this thesis is organised as follows.

Ch. 1 present the governing equations for a general compressible two-phase flow. Two interface capturing methodologies, namely geometric and algebraic, are briefly described. The equations of state employed in the present work are introduced. A general presentation of two wave generation methods, namely the static boundary method and the relaxation zone method, closes this chapter.

Ch. 2 presents an analytic perspective of a fluid impact on a rigid body. First a pure fluid impact is described and utilised to validate the stability and convergence of both incompressible and compressible two-phase solvers against analytic solutions. Secondly, a confined air cavity undergoing a compression and expansion process is evaluated using a 1D liquid piston simulation and the results are compared with a semi-analytic solution. The last part of this chapter investigates an idealised aerated fluid impact and the effects of air on the exerted loads.

Ch. 3 presents computations of a solitary breaking wave impact on a vertical. First, a brief description of the Boussinesq solitary wave theory is presented and a 2D configuration of a solitary wave propagation is employed to perform a sensitivity analysis. Next, a Boussinesq solitary wave propagating over a sloped plane is used to reproduce two types of breaking waves namely: air-pocket and flip-through. Using the a 2D air-pocket breaking wave, the incompressible and compressible solvers are compared. Moreover, the simulated

2D compressible results are compared with the experimental data for both breaking conditions. The last section of this Chapter, compares the numerical and experimental results of an air-pocket impact using a 3D configuration.

Ch. 4 presents a validation of a large scale numerical wave flume generating waves and their interaction with an OWC. First, a brief description of the irregular wave theory is introduced and a rectangular 2D domain is employed to evaluate the *relaxation zone method* for generating random waves following a JONSWAP calibration. Next, the chapter focuses on comparative study of numerical and experimental data of waves interacting with an OWC. First, an OWC facing regular waves is validated by putting special interest on the chamber behaviour and a PTO modelling by using a porous medium. Finally, the interaction of irregular waves with an OWC is validated and the extreme wave loads on the structure front wall are analysed.

A closure chapter presents the summary and conclusion regarding this study and suggestions for future research are briefly discussed.

Chapter 1

Governing equations

In this chapter, the general Navier-Stokes equations are briefly introduced. Next, the numerical methodology employed in the present work is described focusing on some relevant aspects selected by the author such as; the interface treatment in multiphase problems. A compressible multiphase pressure-based solver within the `OpenFOAM` toolbox. And, finally, an overview of two different boundary conditions for wave generation.

1.1 Navier-Stokes equations

Regarding the fluid as a continuous medium where only macroscopic length scales (say $1\mu m$ or larger) are studied. Molecular structure of matter and molecular motion may be then ignored. The fluid behaviour is described in terms of macroscopic properties: velocity, pressure, density and temperature, as well as their respective space and time derivatives. These properties may be though of as averages over a suitable large number of molecules. A fluid particle or point in a fluid is then the smallest possible element of fluid whose macroscopic properties are not influenced by individual molecules. Here, the fluid particle will be represented in a two-dimension perspective and shaped as a square (Fig. 1.1) for geometric simplicity reasons.

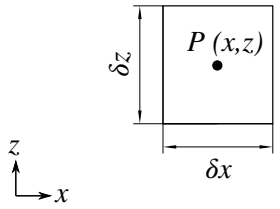

Figure 1.1: Fluid element

The element under consideration is so small that the fluid properties at the faces can be expressed accurately enough using the first two terms of a Taylor series expansion. For example, for a generic field φ at a face distancing $\delta x/2$ from the fluid element centre can be expressed as,

$$\varphi(x + \frac{\delta x}{2}) = \varphi(x) + \frac{\delta x}{2}\frac{\partial \varphi(x)}{\partial x} + O(x) \ .$$

1.1.1 Mass conservation

The mass of fluid is conserved in the fluid element. Consequently, the rate of increase of mass equals the net rate of flow of mass into the fluid element. The rate of increase of mass in the fluid element is:

$$\frac{\partial \rho}{\partial t}\delta x \delta z \ ,$$

where ρ introduces the fluid density and assuming the fluid element volume ($\delta x \delta z$) remains constant over time. The net rate of flow of mass into the fluid element is the summation of volume flux through the element surface. This volume flux, Fig. 1.2, corresponds to the product of density, surface area and the velocity component normal to the surface. Then the flux is positive when entering the fluid element or negative when leaving.

$$\frac{\partial \rho}{\partial t}\delta x \delta z = -\frac{\partial (\rho u)}{\partial x}\delta x \delta z - \frac{\partial (\rho w)}{\partial z}\delta x \delta z \tag{1.1}$$

Balancing the net rate of flow of mass with the rate of increase of mass and dividing all by the element volume yields

$$\frac{\partial \rho}{\partial t} + \nabla \cdot (\rho \mathbf{u}) = 0 \ . \tag{1.2}$$

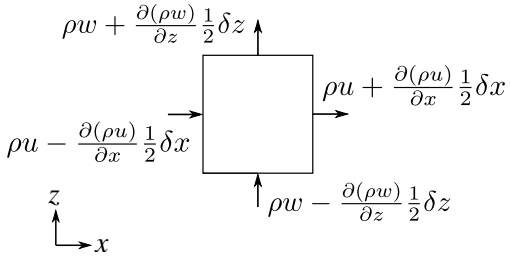

Figure 1.2: Mass conservation of a 2D fluid element

Equation (1.2) is the unsteady, three-dimensional mass conservation or continuity equation at a point in a compressible fluid. Here bold $\mathbf{u}$ represents a vector. For an incompressible fluid the density ρ is constant and eq. (1.2) becomes:

$$\nabla \cdot \mathbf{u} = 0 \ . \tag{1.3}$$

1.1.2 Momentum equation

The momentum conservation law make statements regarding changes of properties of a fluid particle. This is referred to as the Lagrangian approach. These properties are then functions of the position (x, z) of the particle and time (t). The total derivative $D\varphi/Dt$ of a generic field φ with respect to time of a fluid particle following the flow $(dx/dt = u,\ dz/dt = w)$ is

$$\frac{D\varphi}{Dt} = \frac{\partial \varphi}{\partial t} + \mathbf{u} \cdot \nabla \varphi \ .$$

This defines the rate of change of property φ per unit mass. However, the equations developed in this work evaluate the rates of change per unit volume. And, more precisely, the laws are concerned with changes in flow properties for a fluid element that is stationary in space, namely the Eulerian approach. Hence, the total or substantive derivative takes the form,

$$\rho \frac{D\varphi}{Dt} = \frac{\partial(\rho\varphi)}{\partial t} + \nabla \cdot (\rho\varphi \mathbf{u}) \ . \tag{1.4}$$

The rate of increase of momentum of the fluid particle, $\rho D\mathbf{u}/Dt$ will then be obtained by substituting the field φ with the particle velocity vector $\mathbf{u}$. By taking advantage of Newton's second law, the fluid particle rate of increase of momentum must be balanced by the sum of forces on the fluid particle. Expressing this relation using the Lagrangian form,

$$\rho \frac{D\mathbf{u}}{Dt} = \nabla \cdot \underline{\boldsymbol{\sigma}} + \boldsymbol{S} \ . \tag{1.5}$$

The first term on the right-hand side of the equation refers to the Cauchy stress tensor $\nabla \cdot \underline{\boldsymbol{\sigma}}$. Next a source term takes into account the body and the surface forces $\boldsymbol{S} = \boldsymbol{S_b} + \boldsymbol{S_s}$. Here, the body forces are reduced to the gravity $\rho\mathbf{g}$ and the surface force introduces the surface tension. The later has a little if any effect on the present work and, thus, will be neglected if not specified. The state of stress of an isotropic Newtonian fluid element is defined as,

$$\underline{\boldsymbol{\sigma}} = -p\underline{\boldsymbol{I}} + \underline{\boldsymbol{\tau}} = -p\underline{\boldsymbol{I}} + \lambda(\nabla \cdot \boldsymbol{u})\underline{\boldsymbol{I}} + 2\mu\underline{\boldsymbol{S}} \ . \tag{1.6}$$

Here p is the thermodynamic pressure, $\underline{\boldsymbol{I}}$ the identity tensor and $\underline{\boldsymbol{\tau}}$ the viscous stress tensor. The viscous stresses of a compressible Newtonian fluid involve two constants of proportionality: the first (dynamic) viscosity, μ, to relate stresses to linear deformations, and the bulk viscosity, λ, to relate stresses to volumetric deformation. The strain-rate tensor can be expressed as $\underline{\boldsymbol{S}} = 1/2[\nabla \boldsymbol{u} + (\nabla \boldsymbol{u})^T]$. The viscous stress τ is typically decomposed into the isotropic and deviatoric parts:

$$\underline{\boldsymbol{\tau}} = \left(\lambda + \frac{2}{3}\mu\right)(\nabla \cdot \mathbf{u})\underline{\boldsymbol{I}} + \mu\left(\nabla \boldsymbol{u} + (\nabla \boldsymbol{u})^T - \frac{2}{3}(\nabla \cdot \boldsymbol{u})\underline{\boldsymbol{I}}\right) , \tag{1.7}$$

introducing the second viscosity $\zeta \equiv \lambda + 2\mu/3$ which is usually neglected by explicitly assuming $\zeta = 0$. Not much is known about the second viscosity ζ which is supposed to have a small effect in practice. Recent studies signalled that may be relevant in specific processes such as shock waves or sound waves attenuation, e.g. [83]. Finally, introducing these terms into the momentum equation (1.5) leads to the so-called Navier-Stokes equation in the convective form,

$$\rho\left(\frac{\partial \boldsymbol{u}}{\partial t} + \boldsymbol{u} \cdot \nabla \boldsymbol{u}\right) = -\nabla p + \nabla \cdot \left[\mu\left(\nabla \boldsymbol{u} + (\nabla \boldsymbol{u})^T - \frac{2}{3}(\nabla \cdot \boldsymbol{u})\underline{\boldsymbol{I}}\right)\right] + \boldsymbol{S} . \tag{1.8}$$

Moreover, by assuming the fluid as incompressible, this last equation takes the general form,

$$\rho\left(\frac{\partial \boldsymbol{u}}{\partial t} + \boldsymbol{u} \cdot \nabla \boldsymbol{u}\right) = -\nabla p + \mu \nabla^2 \boldsymbol{u} + \boldsymbol{S} , \tag{1.9}$$

appropriate for a wide range of situations.

1.2 Numerical method

This section describes the numeric methodology employed in the present work to model multiphase, i.e. air and water, problems. First, the finite volume method and important related notation is briefly introduced. One of the major difficulties of this method relies on the fluids interface and here an attempt to clarify two major approaches is introduced in Sec. 1.2.2. Finally, the core equations of a pressure-based two-phase compressible solver are described with a final overview of the solving procedure.

1.2.1 Finite volume method

The basis of the finite volume method is the integral conservation law. The essential idea is to divide the numerical domain $\mathcal{D}$ into many control volumes and approximate the integral conservation law on each of the control volumes. Similarly, the time is also divided into many time steps Δt. By denoting a control volume Ω, its boundary by $\partial\Omega$ and its volume by V. The momentum conservation integral equation takes the form,

$$\begin{aligned}
&\int_t^{t+\Delta t}\left[\int_\Omega \frac{\partial(\rho \boldsymbol{u})}{\partial t} dV + \int_\Omega \nabla \cdot (\rho \boldsymbol{u} \otimes \boldsymbol{u}) dV\right] dt \\
&= \int_t^{t+\Delta t}\left[-\int_\Omega \nabla p dV + \int_\Omega \nabla \cdot (\mu \nabla \boldsymbol{u}) dV + \int_\Omega \nabla \cdot \left(\mu(\nabla \boldsymbol{u})^T - \frac{2}{3}(\nabla \cdot \boldsymbol{u})\underline{\boldsymbol{I}}\right) dV + \int_\Omega \boldsymbol{S} dV\right] dt ,
\end{aligned} \tag{1.10}$$

where $\otimes$ is the outer product. By making use of the Gauss theorem for the divergence terms,

$$\int_t^{t+\Delta t}\left[\int_\Omega \frac{\partial(\rho \boldsymbol{u})}{\partial t}dV + \int_{\partial\Omega}\Big(\nabla\cdot(\rho\boldsymbol{u}\otimes\boldsymbol{u})\Big)\cdot d\boldsymbol{S}\right]dt$$
$$= \int_t^{t+\Delta t}\left[-\int_\Omega \nabla p dV + \int_{\partial\Omega}(\mu\nabla\boldsymbol{u})\cdot d\boldsymbol{S} + \int_{\partial\Omega}\nabla\cdot\Big(\mu(\nabla\boldsymbol{u})^T - \frac{2}{3}(\nabla\cdot\boldsymbol{u})\underline{\boldsymbol{I}}\Big)\cdot d\boldsymbol{S} + \int_\Omega \boldsymbol{S}dV\right]dt\ . \tag{1.11}$$

The objective is to follow a discretisation practice on the above equation, as well as the integral form of the continuity equation, to obtain a system of algebraic equations. The solution of the system produces a set of values which correspond to the solution of the original equation at some pre-determined locations in space and time. The discretisation can be divided into two separate procedures: the discretisation of the solution domain using the aforementioned control volumes, and the equation discretisation.

The notation that will follow denotes the physical domain $\mathcal{D}$ which is divided into a large number of control volumes, Ω_i, for $i = 1, .., N_\Omega$. For instance, if $\mathcal{D} \in \mathbb{R}^3$ it seems appropriate to call Ω_i as a control volume, and, if $\mathcal{D} \in \mathbb{R}^2$ to call it control cell. If two cells i and j are adjacent, their shared boundary, $\partial\Omega_i \cap \partial\Omega_j$ is called an internal face. If cell i touches the domain boundary, the shared surface $\partial\Omega_i \cap \partial\mathcal{D}$, will consist of one or more boundary faces. All faces in the domain $\mathcal{D}$ are labelled with integers, $j = 1, .., N_f$, and the surface of face j is denoted $\mathcal{F}_j$. Then the boundary of cell i, may be represented by a list, B_i, of all the labels of faces belonging to its boundary, $\partial\Omega_i$.

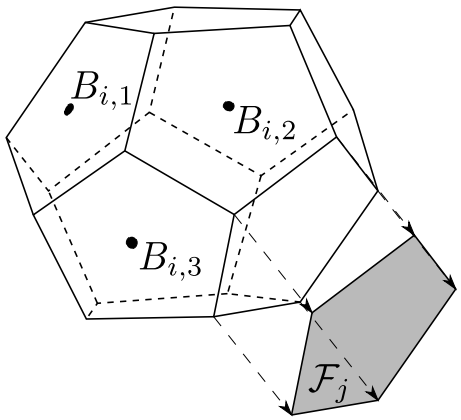

Figure 1.3: Sketch of control volume Ω_i

1.2.1.1 Spatial equation discretisation

Regarding eq. (1.9) it is clear that a series of volume and surface integrals need to be evaluated. The accuracy of the discretisation method depends on the assumed variation of the generic function $\varphi(\boldsymbol{x}, t)$ as it was introduced in eq. (1.1). The most relevant is the representation of the generic field in terms of cell averaged values

$$\int_{\Omega_i}\varphi(\boldsymbol{x}, t)dV = \varphi_i(t)V_i\ . \tag{1.12}$$

Considering the terms under the divergence operator. It is important to notice that the control volume is bounded by a series of flat faces. Then the surface integrals can be expressed, using the vector generic field $\boldsymbol{\varphi}(\boldsymbol{x}, t)$, as

$$\int_{\partial\Omega_i} \Big(\nabla \cdot \boldsymbol{\varphi}(\boldsymbol{x},t)\Big) \cdot d\boldsymbol{S} = \sum_{j\in\partial\Omega_i} \boldsymbol{\varphi}_j(t) \cdot \boldsymbol{S}_j \ . \tag{1.13}$$

where $\boldsymbol{S}_j$ is the face j area vector pointing outwards from the control volume. In the above equation, the face field $\boldsymbol{\varphi}_j(t)$ is required and should be calculated from the values in the cell centres. This interpolation is a key point when looking for accurate solutions and has been for long a matter of research. For further information on available interpolation schemes and spatial discretisation procedure, the reader is referred to [84].

1.2.1.2 Temporal equation discretisation

Assuming that the control volumes do not change in time. The temporal integrals and the time derivative, using a forward Euler scheme, can be calculated as,

$$\int_t^{t+\Delta t} \varphi(t)dt = \frac{1}{2}(\varphi^{n+1} + \varphi^n)\Delta t \tag{1.14}$$

and

$$\frac{\partial\varphi}{\partial t} = \frac{\varphi^{n+1} - \varphi^n}{\Delta t} \ , \tag{1.15}$$

where

$$\varphi^{n+1} = \varphi(t + \Delta t) \tag{1.16}$$

$$\varphi^n = \varphi(t) \tag{1.17}$$

More complex discretisation schemes are available and the reader is again referred to [84] for further information.

1.2.2 The two phase problem

Considering the numerical domain, $\mathcal{D}$, composed of two immiscible phases $\mathcal{A}$ and $\mathcal{B}$, e.g. air and water. There is necessary condition of a surface, $\mathcal{S}$, assumed negligible thick acting as an interface between both regions. Consequently, the union of these two phases will be the entire domain, $\mathcal{A} \cup \mathcal{B} = \mathcal{D}$, and their intersection the surface, $\mathcal{A} \cap \mathcal{B} = \mathcal{S}$. Each phase has its properties, on the one hand, the phase $\mathcal{A}$ has a density ρ_A and the phase $\mathcal{B}$ a density ρ_B. Then the density field $\rho(\mathbf{x},t)$ has a discontinuity at the surface $\mathcal{S}$. One could use an interpolation procedure to obtain the density at the surface, for example, $\rho = 1/2(\rho_A + \rho_B)$, however, under the negligible thickness assumption, this has a zero volume and the density value on $\mathcal{S}$ is then immaterial.

Let us then define an indicator field $\mathbb{I}(\mathbf{x},t)$,

$$\mathbb{I}(\mathbf{x},t) \equiv \frac{\rho(\mathbf{x},t) - \rho_{\mathcal{B}}}{\rho_{\mathcal{A}} - \rho_{\mathcal{B}}} \ , \tag{1.18}$$

which is independent of the properties of the phases and can be used to describe the density field as,

$$\rho(\mathbf{x},t) = \rho_{\mathcal{A}}\mathbb{I}(\mathbf{x},t) + \rho_{\mathcal{B}}(1 - \mathbb{I}(\mathbf{x},t)) \ . \tag{1.19}$$

This artificial field $\mathbb{I}$ captures the nature of the interface and results in a discontinuity function,

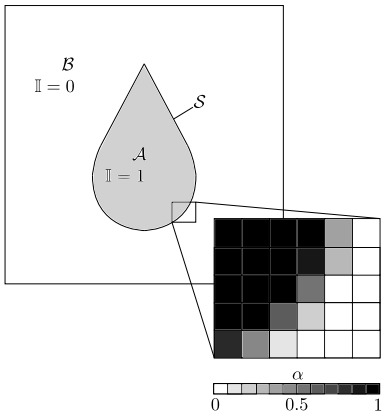

Figure 1.4: Volume of fluid sketch

$$\mathbb{I}(\mathbf{x}, t) = \begin{cases} 1 & for\ \mathbf{x} \in \mathcal{A}(t) \\ 0 & for\ \mathbf{x} \in \mathcal{B}(t) \end{cases} . \tag{1.20}$$

The integration of this quantity over a control volume Ω_i, similarly as eq. (1.12), yields the volume fraction α,

$$\alpha_i \equiv \frac{1}{V_i} \int_{\Omega_i} \mathbb{I}(\mathbf{x}, t) dV \ , \tag{1.21}$$

Now making use of the conservation of mass, eq. (1.2), and substituting the yet defined density field in terms of the indicator field eq. (1.19),

$$\frac{\partial}{\partial t}\Big[\rho_{\mathcal{A}}\mathbb{I}(\mathbf{x}, t) + \rho_{\mathcal{B}}(1 - \mathbb{I}(\mathbf{x}, t))\Big] = -\nabla \cdot \Big[\big(\rho_{\mathcal{A}}\mathbb{I}(\mathbf{x}, t) + \rho_{\mathcal{B}}(1 - \mathbb{I}(\mathbf{x}, t))\big) \cdot \mathbf{u}(\mathbf{x}, t)\Big] \ . \tag{1.22}$$

Integrating the above equation over Ω_i and assuming a constant value of $\rho_{\mathcal{A}}$ and $\rho_{\mathcal{B}}$ in each respective phase within the control volume results in

$$\int_{\Omega_i} \frac{\partial}{\partial t}\Big[(\rho_{\mathcal{A}} - \rho_{\mathcal{B}})\mathbb{I}(\mathbf{x}, t) + \rho_{\mathcal{B}}\Big] dV = -\int_{\Omega_i} \nabla \cdot \Big[(\rho_{\mathcal{A}} - \rho_{\mathcal{B}})\mathbb{I}(\mathbf{x}, t)\mathbf{u}(\mathbf{x}, t)\Big] + \rho_{\mathcal{B}} \nabla \cdot \mathbf{u}(\mathbf{x}, t) dV \ . \tag{1.23}$$

Finally, adopting the fluids as incompressible and the control volume to be constant in time, without mesh deformation, results

$$\frac{\partial}{\partial t} \int_{\Omega_i} \mathbb{I}(\mathbf{x}, t) dV = -\int_{\Omega_i} \nabla \cdot \Big[\mathbb{I}(\mathbf{x}, t)\mathbf{u}(\mathbf{x}, t)\Big] dV \ . \tag{1.24}$$

The left side term can now be substituted using the volume fraction definition eq. (1.21) and making use of the Gauss theorem for the divergence term. Yields to the fundamental equation from which one can derive any consistent interface advection method

$$\frac{\partial \alpha_i}{\partial t} = -\frac{1}{V_i} \int_{\partial\Omega_i} \mathbb{I}(\mathbf{x}, t)\mathbf{u}(\mathbf{x}, t) \cdot d\boldsymbol{S} \ . \tag{1.25}$$

We stress that this equation is exact with no numerical approximations introduced yet. Different solution methodologies focus now specifically on the right-hand side term and here two of them, namely algebraic and geometric, will be briefly introduced.

1.2.2.1 The algebraic method

The algebraic method (see [85, 86]) does not attempt to keep the singular nature of the indicator field within the control volume for phase transport. Instead, it relies on the control volume averaged value of it using the liquid volume fraction field. Going back to the transport term (right hand side) in eq. (1.24). Making use of the Leibniz integral rule and the definitions from eq. (1.12) and (1.21) the divergence term can be expressed as

$$\int_{\Omega_i} \nabla \cdot \Big[\mathbb{I}(\mathbf{x},t)\mathbf{u}(\mathbf{x},t)\Big] dV = \nabla \cdot \Big[\mathbf{u}_i \int_{\Omega_i} \mathbb{I}(\mathbf{x},t) dV\Big] = \nabla \cdot (\alpha_i \mathbf{u}_i) \ . \tag{1.26}$$

However, there is a necessity to modify this term due to serious numerical diffusion issues which are opposed to the discontinuous nature of indicator field $\mathbb{I}(\mathbf{x},t)$. Now the liquid volume fraction transport equation can be rewritten in the integral form as

$$\int_{\Omega_i} \frac{\partial \alpha_i}{\partial t} dV + \int_{\partial\Omega_i} \alpha_i \mathbf{u}_i \cdot d\boldsymbol{S} \ = 0 \ , \tag{1.27}$$

or its discrete counterpart

$$\frac{\alpha_i(t+\Delta t) - \alpha_i(t)}{\Delta t} = -\frac{1}{V_i} \sum_{j \in \partial\Omega_i} (F_u + \lambda_M F_c)(t) \tag{1.28}$$

where the unsteady term is discretised using the forward Euler scheme for simplicity and the advection term appears as a summation over all the cells faces. Here the term λ_M takes the role of a delimiter implemented in the MULES solver (Multidimensional Universal Limiter with Explicit Solution). It will take a value of one in the transition region (interface) and zero elsewhere. The terms F_u and F_c represent liquid fraction volume fluxes and are expressed by

$$F_u = \phi_j \alpha_j \tag{1.29}$$

$$F_c = \phi_j \alpha_j + \phi_{rj} \alpha_j (1 - \alpha_j) - F_u \tag{1.30}$$

where ϕ_j (volume flux) is assigned by

$$\phi_j = \mathbf{u}_j \cdot \mathbf{S}_j \ , \tag{1.31}$$

and the subscript j, as noted before, means that the quantity is being evaluated at the faces. Away from the interface, $\lambda_M = 0$, the advective term is equal to F_u and the face interpolation of the liquid volume fraction, α_j, will use low order schemes. However, surrounding the fluids interface, $\lambda_M = 1$, the term takes the following form

$$(F_u + \lambda_M F_c) = \phi_j \alpha_j + \phi_{rj} \alpha_j (1 - \alpha_j) \ . \tag{1.32}$$

The right side term is commonly known as the interfacial compression flux. Here the volume flux, ϕ_{rf}, is given by

$$\phi_{rf} = min\left(C_\alpha \frac{|\phi_j|}{|\mathbf{S}_j|}, max\left[\frac{|\phi_j|}{|\mathbf{S}_j|}\right]\right)(\mathbf{n}_j \cdot \mathbf{S}_j) \tag{1.33}$$

where the max operation is performed over the entire domain, while the min operation only locally at each face $j \in \partial\Omega_i$. The constant C_α is a user-specified value to restrict interface smearing. And $\mathbf{n}_j$ is the face-centered interface normal vector given by

$$\mathbf{n}_j = \frac{(\nabla\alpha)_j}{|(\nabla\alpha)_j|} = \left[\frac{(\nabla\alpha)_P + (\nabla\alpha)_N}{2}\right] \Bigg/ \left|\frac{(\nabla\alpha)_P + (\nabla\alpha)_N}{2}\right| \tag{1.34}$$

which points always towards the highest concentration zone of liquid fraction.

1.2.2.2 The geometric method

The geometric method (see [87]) is highly dependent on the local distribution of fluid $\mathcal{A}$ and $\mathcal{B}$ inside the control volume i. Therefore, the method aims to come up with a subgrid model for this "intracellular" distribution from the given volume fraction data. With this information, the volume fluxes on the control volume faces are related to the face wet area. The idea can be easily interpreted if eq. (1.25) is integrated from time t to time $t + \Delta t$ obtaining the equation for the updated volume fraction of cell i

$$\alpha_i(t + \Delta t) = \alpha_i(t) - \frac{1}{V_i} \sum_{j \in \partial\Omega_i} \int_t^{t+\Delta t} \int_{\mathcal{F}_j} \mathbb{I}(\mathbf{x}, \tau)\mathbf{u}(\mathbf{x}, \tau) \cdot d\mathbf{S} d\tau \ . \tag{1.35}$$

The surface of face j is denoted $\mathcal{F}_j$. In most of the two-phase Navier-Stokes solvers the interface advection is resolved before the calculation of the main transport equations and the available fields, such as the velocity, are only known up to time t. The evolution of the velocity field is then approximated as constant (in time) during the whole time step, $\mathbf{u}(\mathbf{x}, \tau) \approx \mathbf{u}(\mathbf{x}, t)$. And the velocity on the face $\mathcal{F}_j$ can be approximated in terms of the volumetric face flux as follows,

$$\mathbf{u}(\mathbf{x}, t) \cdot d\mathbf{S} \approx \frac{\phi_j(t)}{|\mathbf{S}_j|} dS \ for \ \mathbf{x} \in \mathcal{F}_j \ , \tag{1.36}$$

Moreover, the time integral on the right side of eq. (1.35) is the total volume of $\mathcal{A}$ transported across face j during the time interval, defined as $\Delta V_j(t, \Delta t)$.

$$\Delta V_j(t, \Delta t) \approx \frac{\phi_j(t)}{|\mathbf{S}_j|} \int_t^{t+\Delta t} \int_{\mathcal{F}_j} \mathbb{I}(\mathbf{x}, \tau) dS d\tau \ , \tag{1.37}$$

and the surface integral is then simply the instantaneous area of face j submerged in fluid $\mathcal{A}$, from now on denoted as $A_j(\tau)$

$$A_j(\tau) = \int_{\mathcal{F}_j} \mathbb{I}(\mathbf{x}, \tau) dS \ . \tag{1.38}$$

Substituting this into the advection eq. (1.35) leads to

$$\alpha_i(t + \Delta t) = \alpha_i(t) - \frac{1}{V_i} \sum_{j \in \partial\Omega_i} \frac{\phi_j(t)}{|\mathbf{S}_j|} \int_t^{t+\Delta t} A_j(\tau) d\tau \ . \tag{1.39}$$

It is important to highlight that the above equation would be exact if the velocity field is constant both in space and time. For instance, if the cells become sufficiently small compared to the velocity gradients, and the time steps sufficiently small compared to the temporal variations. One can extract from eq. (1.39) that the challenge here is to estimate the time evolution within a time step of the submerged (in fluid $\mathcal{A}$) area of a face, and then integrate this area in time. For doing this, the so-called isoAdvector [87–89] implemented in OpenFOAM makes use of the internal control volume interface, namely isoface, in the cell *upwind* of the studied face j at time t, because this is the cell from which the face receives fluid during the time step. The motion of this isoface *within* the

time step $[t, t+\Delta t]$ is approximated by using the velocity fields on the surrounding control volumes. One of the main difficulties in this process relies on interface *reconstruction schemes* for the definition of the orientation and centre position of the interface within the control volume. The reconstruction techniques remain out of the scope of this work and the reader is referred to the cited articles for further information.

1.2.3 Pressure-based segregated finite volume method

The following sections overview a pressure-based solver for transient two-phase flows using compressible fluids undergoing isentropic processes with barotropic equations of state. The solver makes use of three differential equations such as two independent mass phase balance equations and one momentum equation. And, three algebraic equations such as an algebraic constraint relating the volume fractions and two equations of state related to each phase. By using this system, the objective is to solve the six unknown variables: $\{\alpha_{\mathcal{A}}, \alpha_{\mathcal{B}}, \boldsymbol{u}, p, \rho_{\mathcal{A}}, \rho_{\mathcal{B}}\}$. Under the isentropic process assumption the energy equation is then neglected in the present work if not specified. A cell-centred, co-located finite volume method will be used, which is implemented in OpenFOAM. Here only an overall solution procedure will be explained and further details of the numerics can be found in [84,90–94]. The solver uses a segregated projection algorithm which has many similarities with the PISO (Pressure-Implicit with Splitting of Operators) algorithm; however, here a pressure equation will be solved rather than a pressure corrector equation. This solver adopts and extends the incompressible two-phase algorithm [63, 68, 72, 95] to compressible flows.

1.2.3.1 Mass balance

The mass balance (1.2) in a two-phase problem can be rewritten in terms of each phase k volume fraction as

$$\frac{\partial \rho_k \alpha_k}{\partial t} + \nabla \cdot (\rho_k \alpha_k \mathbf{u}) = 0, \qquad k = \{\mathcal{A}, \mathcal{B}\} \ , \tag{1.40}$$

where ρ_k corresponds to a phase density and α_k to a phase volume fraction. Due to the homogeneous model assumption, there is a single velocity field. The total mass balance (1.2) can be obtained by summing the phasic mass balances over both phases k. Moreover, the volume fractions obey the algebraic relationship

$$\alpha_{\mathcal{A}} + \alpha_{\mathcal{B}} = 1 \ , \tag{1.41}$$

and the density, similarly as in eq. (1.19), can be expressed as

$$\rho = \rho_{\mathcal{A}} \alpha_{\mathcal{A}} + \rho_{\mathcal{B}} \alpha_{\mathcal{B}} \ . \tag{1.42}$$

Now the phase mass balance eq. (1.40) can be expanded as

$$\alpha_k \left(\frac{\partial \rho_k}{\partial t} + \boldsymbol{u} \cdot \nabla \rho_k \right) + \alpha_k \rho_k \nabla \cdot \boldsymbol{u} + \rho_k \left(\frac{\partial \alpha_k}{\partial t} + \boldsymbol{u} \cdot \nabla \alpha_k \right) = 0 \ . \tag{1.43}$$

Regarding the phase density as a function of pressure $\rho_k = \rho_k(p)$ and applying the chain rule to the derivatives of density leads to

$$\left(\frac{\partial \alpha_k}{\partial t} + \boldsymbol{u} \cdot \nabla \alpha_k \right) = -\frac{\alpha_k}{\rho_k} \frac{\partial \rho_k}{\partial p} \left(\frac{\partial p}{\partial t} + \boldsymbol{u} \cdot \nabla p \right) - \alpha_k \nabla \cdot \boldsymbol{u} \tag{1.44}$$

This last equation exist for each phase, thus, for $k = \mathcal{A}$ and $k = \mathcal{B}$. By summing over both phases the total mass balance takes then the form

$$\left(\frac{\alpha_{\mathcal{A}}}{\rho_{\mathcal{A}}}\frac{\partial \rho_{\mathcal{A}}}{\partial p}+\frac{\alpha_{\mathcal{B}}}{\rho_{\mathcal{B}}}\frac{\partial \rho_{\mathcal{B}}}{\partial p}\right)\left(\frac{\partial p}{\partial t}+\boldsymbol{u}\cdot\nabla p\right)+\nabla\cdot\boldsymbol{u}=0 \tag{1.45}$$

This is equation will be further developed in Sec. 1.2.3.4 and solved in the last instance for pressure.

1.2.3.2 Liquid volume fraction equation

The liquid volume fraction is transported using a single equation derived from the mass balance. First in eq.(1.45) the pressure terms are isolated as

$$\frac{\partial p}{\partial t}+\boldsymbol{u}\cdot\nabla p=-\left(\frac{\rho_{\mathcal{A}}\rho_{\mathcal{B}}}{\rho_{\mathcal{B}}\alpha_{\mathcal{A}}\psi_{\mathcal{A}}+\rho_{\mathcal{A}}\alpha_{\mathcal{B}}\psi_{\mathcal{B}}}\right)\nabla\cdot\boldsymbol{u}\ , \tag{1.46}$$

where $\psi_k=\partial\rho_k/\partial p$ is a compressibility factor. Next the right side term is introduced into eq. (1.44) for phase $\mathcal{A}$ and after some rearrangements the following equation is obtained

$$\frac{\partial \alpha_{\mathcal{A}}}{\partial t}+\nabla\cdot(\alpha_{\mathcal{A}}\boldsymbol{u})=\alpha_{\mathcal{A}}\alpha_{\mathcal{B}}\left(\frac{\psi_{\mathcal{A}}\rho_{\mathcal{B}}-\psi_{\mathcal{B}}\rho_{\mathcal{A}}}{\alpha_{\mathcal{A}}\psi_{\mathcal{A}}\rho_{\mathcal{B}}+\alpha_{\mathcal{B}}\psi_{\mathcal{B}}\rho_{\mathcal{A}}}\right)\nabla\cdot\boldsymbol{u} \tag{1.47}$$

Finally, by substituting the velocity divergence on the right side using eq. (1.45), derived now from both phases the final equation reads

$$\frac{\partial \alpha_{\mathcal{A}}}{\partial t}+\nabla\cdot(\alpha_{\mathcal{A}}\boldsymbol{u})=\alpha_{\mathcal{A}}(1-\alpha_{\mathcal{A}})\left(\frac{\psi_{\mathcal{B}}}{\rho_{\mathcal{B}}}-\frac{\psi_{\mathcal{A}}}{\rho_{\mathcal{A}}}\right)\left(\frac{\partial p}{\partial t}+\boldsymbol{u}\cdot\nabla p\right) \tag{1.48}$$

Treatment of the divergence of liquid volume fraction flux is needed using one of the presented methods in Sec. 1.2.2.

1.2.3.3 Momentum equation

The general momentum equation is now adapted by reformulating two terms. Firstly, a modified pressure is introduced to simplify the specification of the pressure boundary conditions. It is defined as:

$$p_d=p-\mathbf{g}\cdot\mathbf{x}\rho \tag{1.49}$$

where p_d stands for the modified pressure, which is obtained by removing the hydrostatic pressure. When calculating the gradient of this new dependant variable it will introduce a density gradient near the interface enabling an efficient treatment of the steep density jump

$$\nabla p_d=\nabla p-\rho\mathbf{g}-\mathbf{g}\cdot\mathbf{x}\nabla\rho\ , \tag{1.50}$$

which has to be account on the momentum equation. On the other hand, the viscous tress term is reformulated. It reads:

$$\begin{aligned}\nabla\cdot\underline{\boldsymbol{\tau}}&=\nabla\cdot\left(\mu\left(\nabla\boldsymbol{u}+(\nabla\boldsymbol{u})^T\right)-\frac{2}{3}(\nabla\cdot u)\underline{\boldsymbol{I}}\right)\\&=\nabla\boldsymbol{u}\cdot\nabla\mu+\nabla\cdot\left(\mu(\nabla\boldsymbol{u}-\frac{2}{3}tr(\nabla\boldsymbol{u})\underline{\boldsymbol{I}})^T\right)\ .\end{aligned} \tag{1.51}$$

Here $tr()$ represents the trace of a vector gradient which is equal to the divergence of that vector. Being more meaningful when accounting for stresses related to volumetric deformation. The final form of the momentum equation is assembled and it reads:

$$\frac{\partial(\rho \boldsymbol{u})}{\partial t}+\nabla\cdot(\rho \boldsymbol{u}\otimes\boldsymbol{u}) = -\nabla p_d-\boldsymbol{g}\cdot\boldsymbol{x}\nabla\rho+\nabla\boldsymbol{u}\cdot\nabla\mu+\nabla\cdot\left(\mu(\nabla\boldsymbol{u}-\frac{2}{3}tr(\nabla\boldsymbol{u})\underline{\boldsymbol{I}})^T\right)+\boldsymbol{S}\ . \quad (1.52)$$

The convective non-linear term is now linearized by using the last iteration values of the velocity within an iteration loop. For notation, the iteration procedure is indexed by superscripts m, with $m = 0$ corresponding to the initial iteration and of the actual time-step t^n. The new time-step is denoted using the superscript $n+1$. Time derivatives will be approximated via forward Euler to facilitate the comprehension. The linearized momentum equation is,

$$\begin{aligned}&\frac{\rho^m\boldsymbol{u}^{n+1}-\rho^n\boldsymbol{u}^n}{\Delta t}+\nabla\cdot(\rho^m\boldsymbol{u}^m\otimes\boldsymbol{u}^{n+1})\\&=-\nabla p_d^{n+1}-\boldsymbol{g}\cdot\boldsymbol{x}\nabla\rho^m+\nabla\boldsymbol{u}^m\cdot\nabla\mu+\nabla\cdot\left(\mu(\nabla\boldsymbol{u}^m-\frac{2}{3}tr(\nabla\boldsymbol{u}^m)\underline{\boldsymbol{I}})^T\right)+\boldsymbol{S}\ .\end{aligned} \quad (1.53)$$

A system of linear algebraic equations will now arise from the discretisation of the integral form of the above standard transport equation. As it was discussed in Sec. 1.2.1.1 and 1.2.1.2 there are multiple discretisation procedures, however, the cell fields will most likely depend on the values of the neighbouring cells. Thus, the system of linear algebraic equations will have one equation for each control volume. Following the procedure proposed by [96] the pressure gradient, as well as the source terms, are not discretised at this stage. This system of linear algebraic equations can be expressed in a matrix form as:

$$[A][\boldsymbol{u}] = [R]\ , \quad (1.54)$$

where $[A]$ is a sparse square matrix. The term $[R]$ is a source vector containing all the terms that can be evaluated without knowing the new $\boldsymbol{u}$, namely, the parts of the temporal derivative, convection and diffusion terms corresponding to the old time-level. The description of $[\boldsymbol{u}]$ and $[R]$ as "vectors" comes from matrix terminology, however, they are a list of values defined at the centres of the control volumes. The matrix $[A]$ can now be decomposed into two matrices containing the diagonal $[D]$ and off-diagonal $[N]$ coefficients, such that:

$$[A] = [D] + [N]\ , \quad (1.55)$$

allowing to define the "H" operator as

$$[H] \equiv [N][\boldsymbol{u}] + [R]\ . \quad (1.56)$$

Finally, then the linear algebraic equation can be written using the above operator as

$$A_P\boldsymbol{u}_P^{n+1} = \sum_{\forall N} A_N\boldsymbol{u}_N^m + E_P^n = H(\boldsymbol{u}^m)\ , \quad (1.57)$$

where the matrix coefficients A_P on the diagonal of $[A]$ and A_N off the diagonal. Here the subscripts P refer to the solving cell and N to its neighbouring cells. Now including the neglected pressure and source terms, leads to

$$\boldsymbol{u}_P^{n+1} = A_P^{-1}H(\boldsymbol{u}^m) - A_P^{-1}\boldsymbol{g}\cdot\boldsymbol{x}\nabla\rho^m + A_P^{-1}\boldsymbol{S} - A_P^{-1}\nabla p_d^{n+1}\ . \quad (1.58)$$

Grouping the first three terms on the right side together, the velocity reads

$$\boldsymbol{u}_P^{n+1} = \tilde{\boldsymbol{u}}^r - A_P^{-1}\nabla p_d^{n+1} \ , \tag{1.59}$$

and the velocity $\tilde{\boldsymbol{u}}^r$ is

$$\tilde{\boldsymbol{u}}^r = A_P^{-1}H(\boldsymbol{u}^r) - A_P^{-1}\boldsymbol{g}\cdot\boldsymbol{x}\nabla\rho^m + A_P^{-1}\boldsymbol{S} \ . \tag{1.60}$$

Due to the issues with collocated variable arrangements that were observed when the phase fractions changes abruptly and the densities of the two fluids are very different [90]. Equation (1.59) is interpolated to the cell faces j and associated with the volume fluxes ($\phi_j = \boldsymbol{u}_j \cdot \boldsymbol{S}_j$) as

$$\phi_j^{n+1} = \tilde{\phi}_j^m - (A_P^{-1})_j |S_j| \nabla_j^{\perp} p_d^{n+1} \ , \tag{1.61}$$

where $\nabla_j^{\perp}$ refer to the face gradient. And the first term of the right side is

$$\tilde{\phi}_j^m = \left(A_P^{-1}H(\boldsymbol{u}^m)\right)_j - (A_P^{-1})_j |S_j| \boldsymbol{g}\cdot\boldsymbol{x}\nabla_j^{\perp}\rho^m + \left(A_P^{-1}\boldsymbol{S}\right)_j \cdot \boldsymbol{S}_j \ . \tag{1.62}$$

1.2.3.4 Pressure equation

The modified pressure fields are obtained using the mass balance derived equation (1.45). Following a similar procedure, using now the modified pressure, the equation is linearized and discretised first as

$$\left(\frac{\alpha_{\mathcal{A}}^m}{\rho_{\mathcal{A}}^m}\psi_{\mathcal{A}}^m + \frac{\alpha_{\mathcal{B}}^m}{\rho_{\mathcal{B}}^m}\psi_{\mathcal{B}}^m\right)\left(\frac{p_d^{n+1} - p_d^n}{\Delta t} + \nabla\cdot(p_d^{n+1}u^m) - p_d^{n+1}\nabla\cdot u^m + \lambda\right) + \nabla\cdot\boldsymbol{u}^{n+1} = 0 \ , \tag{1.63}$$

where $\psi_k = \partial\rho_k/\partial p$ and λ is given by

$$\lambda = \frac{(\rho\boldsymbol{g}\cdot\boldsymbol{x})^m - (\rho\boldsymbol{g}\cdot\boldsymbol{x})^n}{\Delta t} + \nabla(\rho\boldsymbol{g}\cdot\boldsymbol{x})^m\boldsymbol{u}^m - (\rho\boldsymbol{g}\cdot\boldsymbol{x})^m\nabla\cdot\boldsymbol{u}^m \ . \tag{1.64}$$

It is observable how the last divergent term uses the new velocity which will be used as a link with equation (1.59). The terms coming from the pressure gradient have a little impact on low Mach flows and will be neglected in the present work, if not indicated. Now following the collocated approach, the divergence term is discretised and substituted using the volume flux as

$$\left(\frac{\alpha_{\mathcal{A}}^m}{\rho_{\mathcal{A}}^m}\psi_{\mathcal{A}}^m + \frac{\alpha_{\mathcal{B}}^m}{\rho_{\mathcal{B}}^m}\psi_{\mathcal{B}}^m\right)\left(\frac{p_d^{n+1} - p_d^n}{\Delta t} + \lambda\right) + \sum_{j\in\partial\Omega_i}\phi_j^{n+1} = 0 \ , \tag{1.65}$$

which is subsituted using eq. (1.59). Finally, the pressure p_d^{n+1} can be solved implicitly.

Regarding the code in `compressibleInterFoam` it is observable how the solving matrix for pressure is assembled using three terms. The first term is the flux divergence in eq. (1.65), which is defined as `p_rghEqnIncomp` and it reads

$$\begin{aligned}\texttt{p\_rghEqnIncomp} = &+ \sum_{j\in\partial\Omega_i}\tilde{\phi}_j^m \\ &- \sum_{j\in\partial\Omega_i}(A_P^{-1})_j|\boldsymbol{S}_j|\nabla_j^{\perp}p_d^{n+1} \ .\end{aligned} \tag{1.66}$$

The first term will be treated explicitly and the second implicitly. Next, the compressible term in the derived continuity equation (1.65) is calculated for each phase using the next equations

$$\begin{aligned}\texttt{p\_rghEqnComp1} = \texttt{pos}(\alpha_{\mathcal{A}})*\\ (\\ &+\frac{1}{\rho_{\mathcal{A}}}\left(\frac{\partial \alpha_{\mathcal{A}}}{\partial t}+\sum_{j\in\partial\Omega_i}(\alpha_{\mathcal{A}}\rho_{\mathcal{A}}\phi)_j\right)\\ &-\frac{\partial \alpha_{\mathcal{A}}}{\partial t}-\sum_{j\in\partial\Omega_i}(\alpha_{\mathcal{A}}\phi)_j\\ &+\left(\frac{\alpha_{\mathcal{A}}\psi_{\mathcal{A}}}{\rho_{\mathcal{A}}}\right)_j\cdot correction(\frac{\partial p_d}{\partial t})\\ ) .\end{aligned} \tag{1.67}$$

and

$$\begin{aligned}\texttt{p\_rghEqnComp2} = \texttt{pos}(\alpha_{\mathcal{B}})*\\ (\\ &+\frac{1}{\rho_{\mathcal{B}}}\left(\frac{\partial \alpha_{\mathcal{B}}}{\partial t}+\sum_{j\in\partial\Omega_i}(\alpha_{\mathcal{B}}\rho_{\mathcal{B}}\phi)_j\right)\\ &-\frac{\partial \alpha_{\mathcal{B}}}{\partial t}-\sum_{j\in\partial\Omega_i}(\alpha_{\mathcal{B}}\phi)_j\\ &+\left(\frac{\alpha_{\mathcal{B}}\psi_{\mathcal{B}}}{\rho_{\mathcal{B}}}\right)_j\cdot correction(\frac{\partial p_d}{\partial t})\\ ) .\end{aligned} \tag{1.68}$$

In the first part of these equations, the function `pos()` is introduced which activates or desactivate the `p_rghEqnComp` by taking values of 1 if the argument is bigger than 0 or a value of 0 elsewhere. Thus, activating the phase compression effects only for cells within that phase. The second term is explicit and it will reinforce the mass conservation which has been highlighted as a major issue in similar solvers, i.e. [97]. This would be zero if a perfect mass balance is obtained according to eq. (1.40). The third and the fourth term together resemble eq. (1.44) for a non-transonic flow. Thus, on a perfect conservation situation would be also zero. Essentially, the `correction()` function is a correction to the general continuity equation, eq. (1.2), introduced by changes in pressure which are neglected by the momentum equation origin of the velocity and density fields. The term λ, eq. (1.64), should appear inside this correction however is neglected for faster convergence solutions.

It is important to highlight the fact that the volume flux employed to calculate ϕ_j^{n+1} depends on eq. (1.62) which comes from the momentum equation and, thus, it does not necessarily fulfil the mass conservation. Then, a final correction using the newly calculated pressure is introduced using eq. (1.59).

$$\phi_j^{n+1} = \tilde{\phi}_j^m - (A_P^{-1})_j |S_j| \nabla_j^{\perp} p_d^{n+1} \ , \tag{1.69}$$

And, following a flux reconstruction process, the new velocity $\boldsymbol{u}_P^{n+1}$.

1.2.4 Equation of state

To close the system of equations, as mentioned previously, an equation of state is needed to determine the fluid density based on the pressure. To model the lighter phase, air, the ideal gas equation of state is used. To avoid the additional energy conservation equation, the air behaviour undergoing compression and expansions is assumed to be isentropic. Under these assumptions, the equation of state for an ideal gas undergoing an adiabatic pressure compression/expansion reads:

$$\frac{p}{\rho^{\gamma}} = a_c = const. \ , \tag{1.70}$$

where $\gamma = 1.4$ denotes the ratio of (constant) specific heats and a_c is the isentropic constant. From this equation, one can derive the compressibility factor ψ:

$$\psi = \left(\frac{\partial \rho}{\partial p}\right)\bigg|_s = \frac{1}{a_c \gamma}\left(\frac{p}{a_c}\right)^{\frac{1-\gamma}{\gamma}} \ . \tag{1.71}$$

On the other hand, the water can be modelled as incompressible in most situations because the compressible pressure waves will not be present. Nevertheless, a weakly compressible or stiffened equation of state is employed under certain conditions. This equation of state is derived from the work initially proposed by Cole in 1948 [98] assuming a constant entropy and is commonly used by the Smooth Particle Hydrodynamics (SPH) community. It takes the name of Tait's equation and it reads

$$\rho = \rho_0 \left(\frac{p + B}{p_0 + B}\right)^{\frac{1}{\gamma}} \ , \tag{1.72}$$

where $\gamma = 7$ is the adiabatic constant, p_0 is the reference pressure and $B = (\rho_0 c^2/\gamma) - p_0$ with c being the constant speed of sound. Then, the compressibility factor ψ is

$$\psi = \left(\frac{\partial \rho}{\partial p}\right)\bigg|_s = \frac{\rho_0}{\gamma(p_0 + B)}\left(\frac{p + B}{p_0 + B}\right)^{\frac{1-\gamma}{\gamma}} \ . \tag{1.73}$$

Finally, using the updated pressure one can simply resolve the algebraic relation given by the selected equations of state $\rho_k = \rho_k(p)$ for each phase obtaining the new phase densities ($\rho_{\mathcal{A}}$ refers to the liquid density. And, finally, the averaged density can be calculated using

$$\rho = \alpha_{\mathcal{A}} \rho_{\mathcal{A}} + \alpha_{\mathcal{B}} \rho_{\mathcal{B}} \ , \tag{1.74}$$

where $\rho_{\mathcal{A}}$ refers to the liquid density and $\rho_{\mathcal{B}}$ to the gas density.

1.2.5 Solution procedure

The solution procedure employed in the present work is the PIMPLE algorithm. It consists of an iterative method reminiscent of the PISO algorithm (Pressure-Implicit with Splitting of Operators) [99,100] that solve each linearized equation sequentially, with the possibility of multiple outer correctors within one time-step. For multiphase flows, the momentum predictor step, part of the PISO algorithm, has shown not to be essential for improving the convergence behaviour and it is left as a user decision.

It was presented in eq. (1.53) that the discrete equations are linearized by using the solution of the previous iterations in the non-linear term of the momentum equation. This

can lead to a large change of the velocity and, thus, a divergence. For solving this, the Patankar's implicit under relaxation [101] is introduced commonly used in the SIMPLE (Semi-Implicit Method for Pressure Linked Equations) procedure. This is the main reason to call this loop PIMPLE (PISO+SIMPLE).

The global algorithm is graphically presented in Fig. 1.5 and the pressure corrector sub-cycle in Fig. 1.6. The workflow can be summarised as follows:

1. Set up the initial conditions for all fields values.
2. Start the calculation of the new time step.
3. Go through the PIMPLE loop for `nOuterCorrectors`.
   (a) Start a liquid volume fraction loop for updating the α values until the tolerance is reached, eq. (1.48). Calculate an initial value for densities.
   (b) Assemble and solve the momentum predictor equation with the available face fluxes. If this option is switched off, the velocity field from the previous time step will be used instead. Relax the momentum equation.
   (c) Go through the PISO loop until the tolerance for the pressure-velocity system is reached
      i. Calculate initial volume flux prediction, eq. (1.62).
      ii. Assemble phase compressibility pressure terms `p_rghEqnComp`, eq. (1.67), (1.68).
      iii. Go through a non-orthogonality corrector loop at least for one iteration.
         - Assemble incompressible continuity term `p_rghEqnIncomp`, eq. (1.66). Solve the pressure equation.
      iv. Calculate a new compressibility term for alpha transport, right side eq. (1.48).
      v. Correct flux, eq. (1.59), and reconstruct internal velocity field.
      vi. Update densities from equations of state. Calculate the average density, eq. (1.42).
   (d) If the flow is turbulent, calculate the effective viscosity from the turbulence variables.
4. If the final time is not reached, return to step 2.

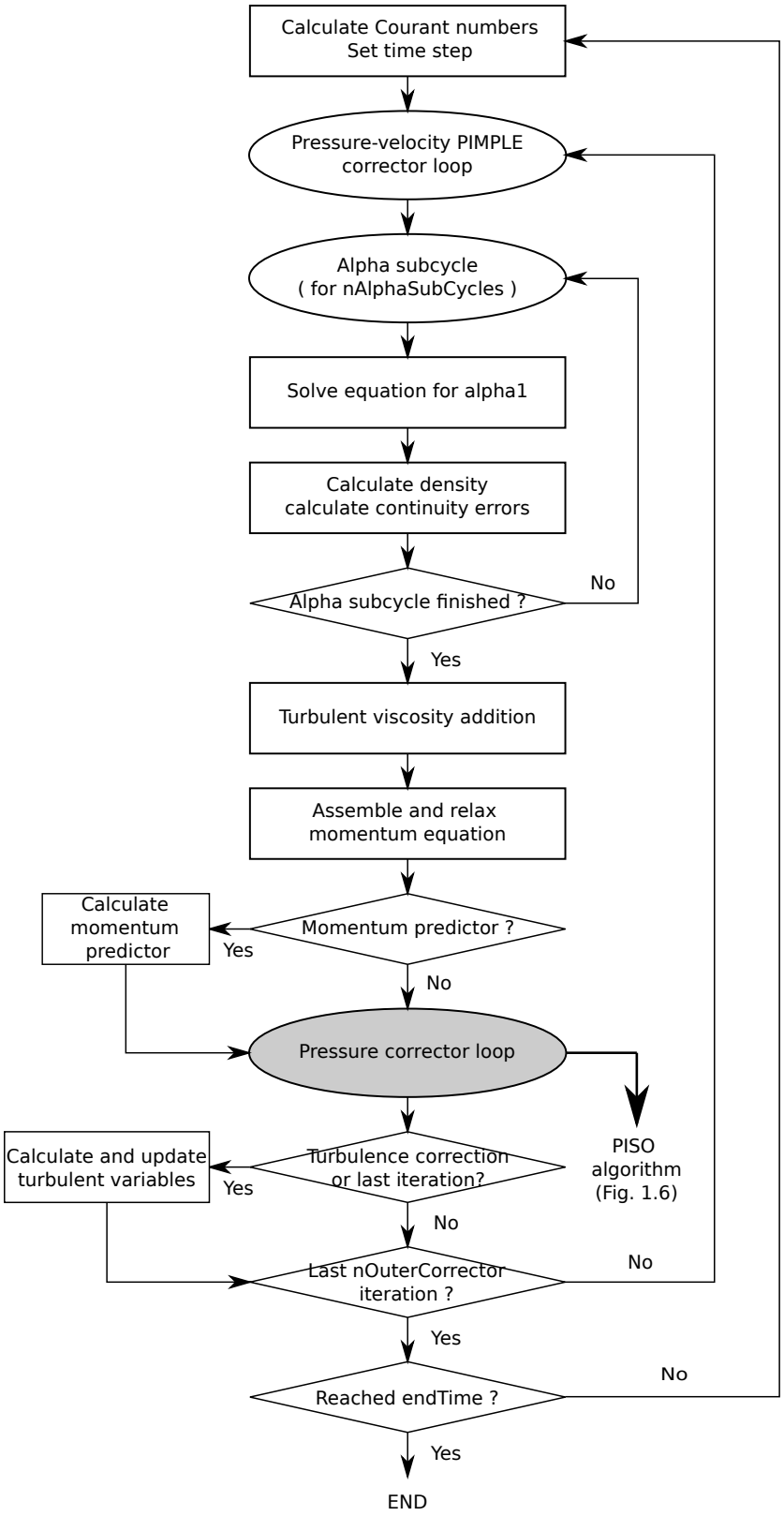

Figure 1.5: Global algorithm

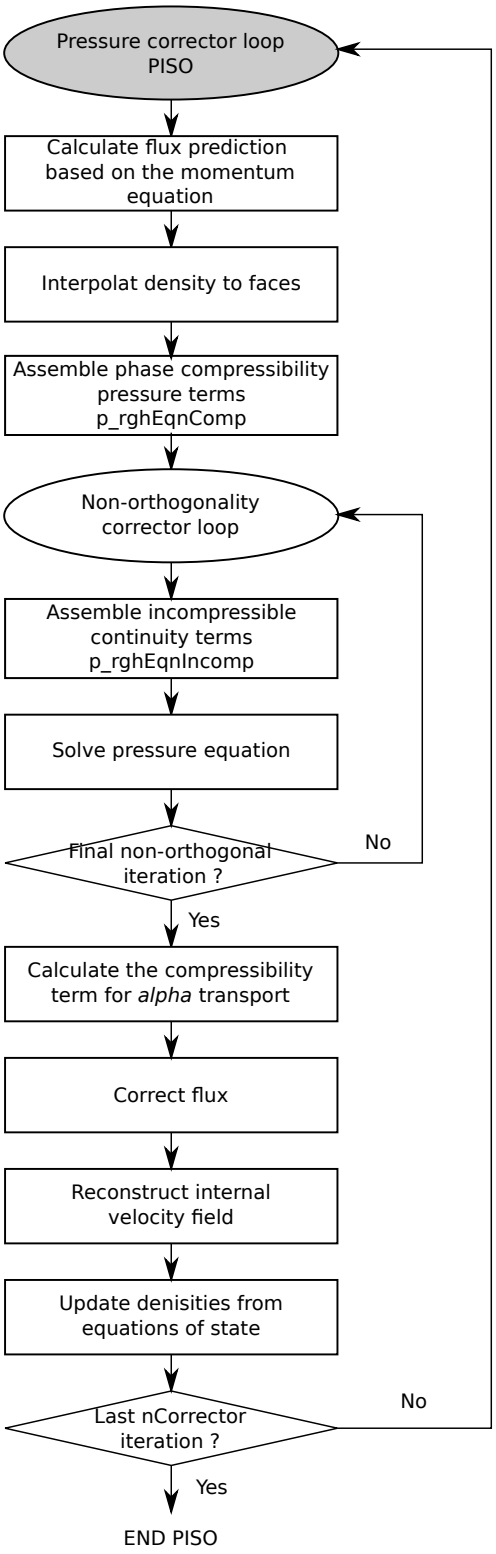

Figure 1.6: PISO algorithm

1.3 Wave generation

Wave generation is a critical point regarding numerical coastal engineering simulations. To obtain realistic representations of waves in a numerical domain, there is the necessity of defining proper kinematic and free surface elevation conditions. Here these conditions will be introduced by means two types of generation conditions, namely: *static boundary method* [64, 95] and *relaxation zone method* [63].

1.3.1 Static boundary method

The static boundary method prescribes the velocity and liquid volume fraction fields as Dirichlet (i.e. fixed value) conditions at the fixed generation boundary. These fields are analytically calculated using a wide range of wave theories as to the particle velocities and free surface elevation. On the other hand, the pressure has shown to present stability problems if overspecified and is calculated using the existing fields.

The velocities will point towards the domain when generating a wave crest, thus, a positive flux of water will be entering the domain. However, when generating a wave through the flux will be leaving the domain. This will generate an excess of water every wave period periodically rising the water level. Consequently, static wave generators must be linked with active wave absorption.

The present model uses the active absorption which was initially developed by [102]. It is based on linear shallow-water theory, thus, the velocity along the water column height is constant. The concept consists of generating a correction velocity equal to the incident one in the opposite direction. The correction velocity U_c which is horizontal vertically integrated (uniform) reads

$$U_c\, h = c\, \eta_R \ , \tag{1.75}$$

where c is the wave celerity based on the shallow water assumption and h the water depths. These parameters are measured and the reflected wave height η_R is calculated by subtracting the measured elevation at the wavemaker from the analytic elevation.

One of the main advantages of this technique is the possibility to handle all the processes (i.e. generation and absorption) at the boundary. Thus, reducing the computational costs compared to other methods which need to extend the domain or need mesh deformations.

The static boundary method is used in Sec. 3 for generating and absorbing a solitary wave using the Boussinesq theory waves. Sec. 3.1.3 describes the fundamentals of the Boussinesq solitary wave theory.

1.3.2 Relaxation zone method

The relaxation zone method [63] uses blending functions to generate waves and dampen reflected waves within a domain region. It can be seen as an extension of the sponge layer technique [103] which uses damping functions for waves absorption.

The relaxation zone works as a blend between a target φ_{target} and a computed $\varphi_{computed}$ solution. This blend is applied explicitly each time step on the velocity and the liquid volume fraction fields by using a wide variety of waves theories. The blending function acts in the following way

$$\varphi(\boldsymbol{x}, t) = \alpha_R(x)\varphi_{computed}(\boldsymbol{x}, t) + (1 - \alpha_R(x))\varphi_{target}(\boldsymbol{x}, t) \ , \tag{1.76}$$

where the weight field, based on the work of [104], reads

$$\alpha_R = 1 - \frac{exp(\chi^{3.5}) - 1}{exp(1) - 1} \ . \tag{1.77}$$

Then, the target solution will be fully imposed at the boundaries $\alpha_R = 0$. Towards the domain interior, α_R changes smoothly to 0 to force the full computed solution. In this approach, the dynamic pressure is calculated in the usual manner from the continuity equation.

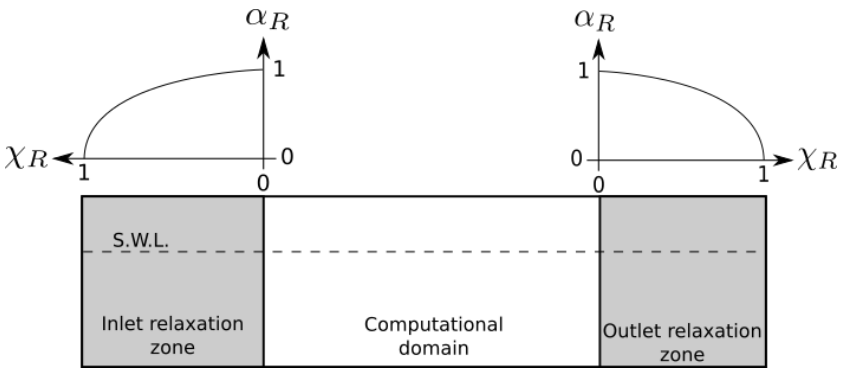

Figure 1.7: Caption

This technique is also used for wave absorption where the target velocity will be then set to 0 and the liquid volume fraction towards the location of the still water level.

The relaxation zone method is used in Sec. 4 for generating and absorbing regular and irregular waves. Sec. 4.1 describes the fundamentals on these two waves conditions.

Chapter 2

Idealised fluid impact

This chapter objective is to investigate the performance of the present numerical approach for modelling an impulsive fluid-structure interaction and describe some of the mechanisms involved. To do this, the next sections are intended to avoid any complexity which is not related to the specified interest. Initially, in Sec. 2.2, a 2D pure liquid impact mimicking the configuration presented by M. Cooker [105] is investigated. The stability and convergence of the compressible `compressibleInterFoam` and incompressible `interFoam` two phase solvers are tested using this configuration. Next, the compressible behaviour of air compressed by water is described utilising a 1D air-liquid piston configuration (Section 2.3). Finally, a situation involving a conceptualised aerated liquid block undergoing an impact is studied in Section 2.4 using a 2D configuration. This work has been partly published in the scientific Journal of Coastal Engineering, see [106].

2.1 Objectives and impact definition

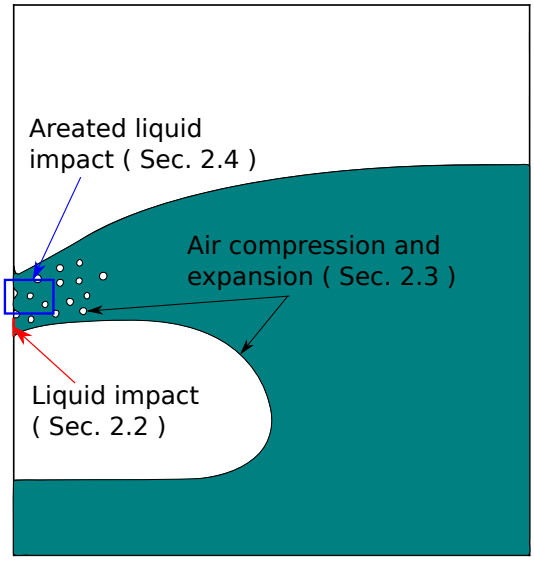

Figure 2.1: Sketch of a wave impact.

When a fluid strikes a body at rest, very large forces are generated over a very short period of time. This situation can be observed when a wave overturns in a certain way that a large number of the fluid particles velocity points perpendicularly to the body, see Fig. 2.1. These particles are rapidly decelerated and the momentum is balanced by a sudden pressure rise, see Fig. 2.2. The very short time related to a wave impact makes the instantaneous Newton's Second Law of little use. Instead, it looks more convenient to use the pressure impulse I theory introduced by Lagrange in 1811 [107], defined as:

$$I(\mathbf{x}) = \int_{t_b}^{t_a} p(\mathbf{x}, t)dt \ , \tag{2.1}$$

where t_b and t_a are the instants before and after the impact respectively.

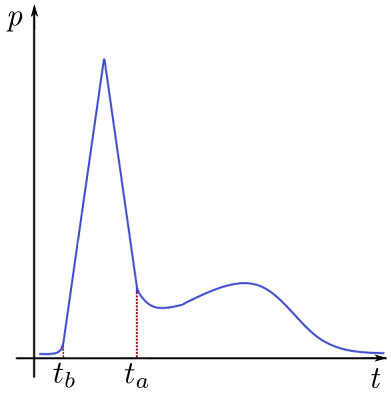

Figure 2.2: Typical pressure record during wave impact

The objective of the present section is to study by simplification the mechanisms involved in producing the observed pressure signals, Fig. 2.2, during a wave breaking impact situation. Multiple factors intervene in this process and they can be roughly

summarized as the wave shape, the velocities and the fluid properties. In the following Section 2.2, the wave shape and the velocities, which are highly dependant on the wave transformation process, are idealised by using basic geometries and constant velocities. However, the fluid properties are kept as a relevant parameter.

In real conditions, the formation of breaking waves usually involves continuous destruction of the free surface. The "fluid" that strikes the bodies is no longer a single fluid but a mixture of air and water. Moreover, during the wave overturning process, air cavities are often entrapped between the water and the solid. Fig. 2.1 intends to represent this situation. The presence of air during an impact is especially relevant due to the lower density and higher compressibility of air compared to water. This has a great effect on the impulsive pressure magnitudes and arises the presence of two differentiated temporal scales during an aerated wave impact. While the phenomenons involving the compressibility of water happen at the scale of microseconds (μs), for air occur in the order of milliseconds (ms). This is further investigated in the next sections.

2.2 2D liquid impact

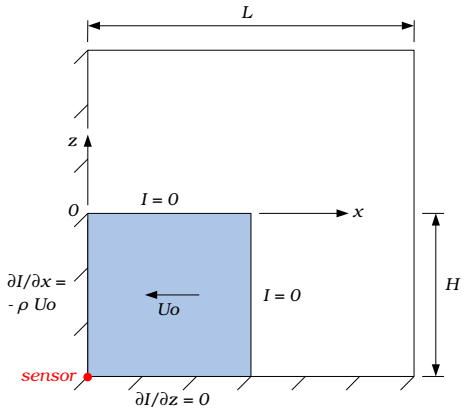

Figure 2.3: Boundary problem proposed by M. Cooker [105]. I refers to the pressure impulse defined in eq. 2.1

This section has two objectives, on the one hand, to study a pure liquid impact similar to the well known *water hammer* phenomenon and secondly, to analyse the stability and convergence of the incompressible and compressible solvers in a fluid-solid impact interaction. For this, a simple configuration is employed which was first presented by M. Cooker in 1995 [105]. The test case consists of a squared liquid block impinging on a vertical wall in a two-dimensional problem, see Fig. 2.3. The fluid is in contact with the bottom and left-hand walls. An initial constant value of velocity U_0 normal to the wall is set in all the liquid domain and the gravity is set to zero. Under these circumstances, the change in velocity is supposed to take place over such a short time that one can assume:

- The nonlinear convective terms in the equation of motion are negligible compared with the time derivative
- The viscosity can be neglected
- The surface tension effects are neglected

This configuration is quite useful for multiple reasons. First, its simplicity allows to perform high-resolution simulations. Secondly, the fact that the relevant phenomenon, the

impact, occurs at the initialization avoids the interference of any other event. Moreover, as is explained in the next sections, the availability of an analytic solution for the pressure impulse under the incompressible assumption and the acoustic pressure solution for the compressible assumption makes this configuration suitable for a complete analysis. Finally, as the liquid phase is already in contact with the left wall from the start of the simulation; this makes the solution independent from the interface jump.

2.2.1 Incompressible formulation

Here the configuration is simulated using the incompressible two phase solver `interFoam`. The analytic solution proposed by M. Cooker in 1995 [105] is first briefly developed. The initial liquid velocity magnitude is constrained by the assumption of a much lower impact speed than the speed of sound, to make the incompressible assumption realistic. After all the mentioned simplifications, the momentum equation can be reduced to

$$\frac{\partial u}{\partial t} = -\frac{1}{\rho}\nabla p \ . \tag{2.2}$$

By integrating this equation with respect to time through the impact interval $[t_a, t_b]$, see Fig. 2.2, and using the pressure impulse definition, eq. 2.1, the resultant equation reads,

$$u_a - u_b = -\frac{1}{\rho}\nabla I \ . \tag{2.3}$$

By making use of the incompressible continuity equation, taking the divergence of the last equation state that,

$$\nabla^2 I = 0 \ , \tag{2.4}$$

the pressure impulse satisfies the Laplace's equation. Using the boundary problem presented in Fig. 2.3. The analytical solution of Laplace's equation can be found using separation of variables and Fourier analysis:

$$I(x,z) = \rho H \sum_{n=1}^{\infty} a_n sin(\lambda_n z/H) \frac{sinh[\lambda_n(b-x)/H]}{cosh(\lambda_n b/H)} \ , \tag{2.5}$$

with $-H \leqslant z \leqslant 0$ and $0 \leqslant x \leqslant b$, where $\lambda_n = (n-0.5)\pi$ and the constants a_n are:

$$a_n = 2U_0 \frac{cos(\lambda_n) - 1}{\lambda_n^2} \ . \tag{2.6}$$

This configuration is modelled with two different phases (water and air), as depicted in Figure 2.3, with $H = 0.05$ m and $L = 0.1$ m. The boundary conditions are set to a solid wall for left and bottom boundaries, and as open boundaries for top and right edges. The separation between the open boundaries and the water region is chosen largely to avoid any influence on the solution. An uniform orthogonal mesh is equally distributed in all the domain, with mesh sizes ranging from $2.5 \times 10^{-4} \leq \Delta x/H = \Delta z/H \leq 4 \times 10^{-3}$. An initial velocity $U_0 = 1\,\mathrm{m/s}$ is set in the water region. Only the first few time steps are computed to capture the impact phenomenon, and the wall pressure distribution is recorded in all the cell face centres of the left boundary at each time step.

The pressure impulse, eq. (2.1), is highly dependant on the definition of t_b and t_a. In the present section, the impulse area is approximated by an isosceles triangle and the rise time as half of the triangle base (see Fig.2.2). In the present simulations, the maximum peak

pressure is reached after the first computed time step and thus, the rise time is equal to the initial time step. Using these definitions, the computed impulse distribution is shown in Fig.2.4 and compared with its analytical counterpart, all divided by a characteristic linear momentum of the liquid block. A perfect agreement is obtained in terms of magnitude and wall distribution between the computed and the analytic solution proposed by [105] for the mesh discretisation $\Delta x/H = 2 \times 10^{-3}$ and a variable time discretisation constrained by a maximum Courant number $\texttt{maxCo} = U \cdot \Delta t/\Delta x = 0.01$.

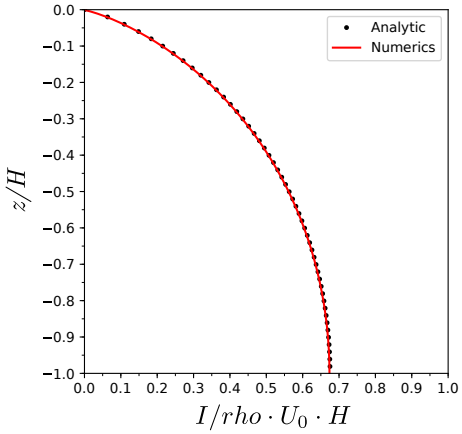

Figure 2.4: Wall pressure impulse distribution compared with the analytic solution, $\Delta x/H = 2 \times 10^{-3}$ and $\texttt{maxCo} = 0.01$.

Figure 2.5 displays maps of the dimensionless pressure impulse (Fig. 2.5a) and the velocity field (Fig. 2.5b) at the impact instant for the water phase only ($\alpha < 0.5$). The pressure gradient (Fig. 2.5a) decelerates the liquid from an initial velocity field U_0 to a new one (Fig. 2.5b), generating a strong liquid jet. This last feature was also described analytically by Cooker and Peregrine as a velocity singularity when $x \to 0$ at the upper water surface.

$\Delta x/H$	t_{imp} $[s]$	p $[bar]$	$I/(\rho \cdot U_0 \cdot H)$
4×10^{-3}	1×10^{-6}	336	0.672042
2×10^{-3}	4.54×10^{-7}	741	0.673706
1×10^{-3}	2.04×10^{-7}	1 652	0.674537
5×10^{-4}	9.34×10^{-8}	3 611	0.674954
2.5×10^{-4}	4.31×10^{-8}	7 831	0.675167

Table 2.1: Simulation results of an idealised wave impact for different spatial discretisations. Results extracted from the numerical pressure sensor presented in Fig. 2.3

In order to check convergence, different spatial (Table 2.1) and temporal (Table 2.2) discretisations have been tested. Table 2.1 presents the results while refining the mesh, where Δx refers to the cell length, t_{imp} the first time step or the rise time, p the peak pressure and I the impulse. The successive mesh refinements result in an asymptotic behaviour of the velocities and, when the maximum Courant Number $\texttt{maxCo}$ is imposed, this results in a time step Δt drop as observed in Table 2.1. The small domain and the very few time steps employed for these computations allow affordable computational costs, even when using such fine discretisations as $\Delta x = 0.0125$ mm ($\Delta x/H = 2.5 \times 10^{-4}$). In these simulations, the maximum Courant number was fixed at $\texttt{maxCo} = 0.01$ and, thus, when reducing the cell size the time step decreased proportionally. Reasonably good stability

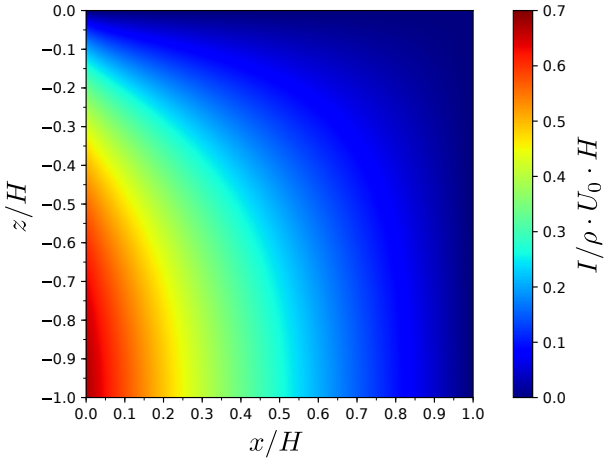

(a) Adimensional pressure impulse

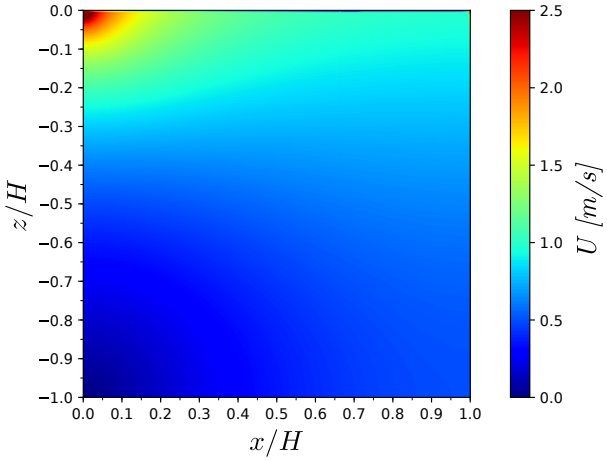

(b) Velocity magnitude

Figure 2.5: Adimensional impulse and velocity magnitude in the liquid region using a cell size $\Delta x/H = 2 \times 10^{-3}$

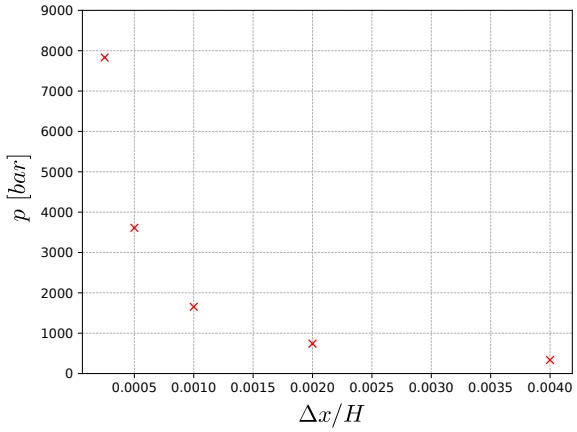

Figure 2.6: Maximum peak pressure at the wall for different spatial discretisations

and convergence of the impulse towards the analytic value of $0.675314(\rho U_0 H)$ is presented. From Fig. 2.6, one can observe that the peak pressure keeps increasing, by approximately a factor of two as the cell length decreases by a fixed factor of 0.5.

maxCo	t_{imp} $[s]$	p $[bar]$	$I/(\rho U_0 H)$
0.1	5×10^{-6}	67	0.673783
0.05	2.5×10^{-6}	134	0.673742
0.01	4.54×10^{-7}	741	0.673706
0.005	2.22×10^{-7}	1515	0.673702
0.001	4.45×10^{-9}	75588	0.673697

Table 2.2: Simulation results of an idealized wave impact for different temporal discretisations

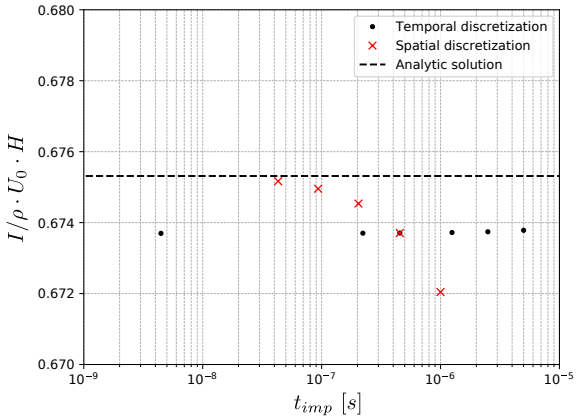

Figure 2.7: Spatial and temporal discretization comparison regarding the dimensionless pressure impulse

Table 2.2 presents the results while modifying the time step by limiting the maximum Courant number and using $\Delta x = 0.1$ mm as cell length. The pressure peak also diverges while refining the time discretization. Finally, Fig. 2.7 presents the results of both tables in terms of adimensional impulse and initial time step. The analytic solution is also represented using a dashed black line. This graph depicts the fact that only lowering the time step will not improve the pressure impulse towards the analytic solution. Although, a combination of both spatial and temporal refinement present a tendency towards the solution proposed by Cooker and Peregrine. It is also important to remark the fact that fixing the time step and refining the cell length stabilises the pressure peak, although, this will not be realistic as it would strongly depend on the selected time step. To conclude, this analysis arises the stability of the solver dealing with an impulsive situation employing the impulse convergence. However, the pressure fields are presented as unreliable under the incompressible assumption for this kind of computations.

2.2.2 Compressible formulation

The idealised wave case is employed here with the same configuration and boundaries as shown in Fig. 2.3. The main difference now is the compressibility of phases with a time-dependant density. To the best of the author's knowledge, similar numerical studies comparing incompressibe and compressibile fluids during impulsive events have been studied using Lagrangian codes, e.g. [80]. As presented in Sec. 1.2.4, the liquid follows now a Tait's equation and the air an ideal gas equation of sate. The system temperature is 20 ° C and the initial pressure is set to atmospheric $p_0 = 1$ bar. The air properties are, $\rho_{air} = 1.2$ kg/m^3 for initial density and a constant specific heat ratio of $\gamma_{air} = 1.4$. For

water, $\rho_{water} = 1000$ kg/m^3, a constant specific heat ratio of $\gamma_{water} = 7$ and a speed of sound of $C_{water} = 1500$ m/s. An initial velocity U_0 pointing perpendicularly to the left boundary is imposed on the water region. An implicit second-order pure Crank-Nicolson scheme is employed for the time derivative in all the simulations. These computations will run using a fixed time step related to the Courant number and the speed of sound, following the relation $C \cdot \Delta t < n \cdot \Delta x$ presented by [79], where C is the speed of sound, Δt the time step, n a user defined value which is set as 0.1 and Δx the cell length.

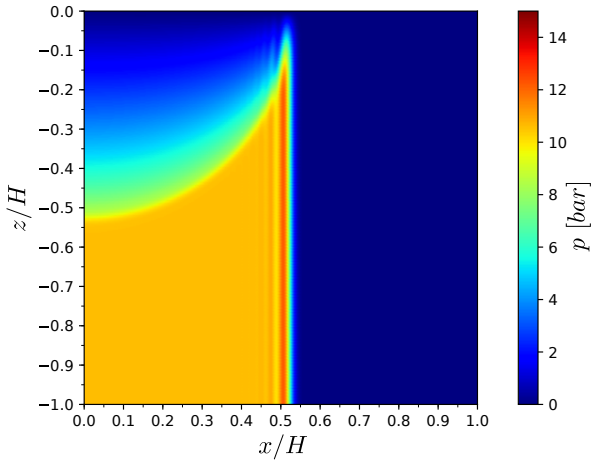

(a) Pressure

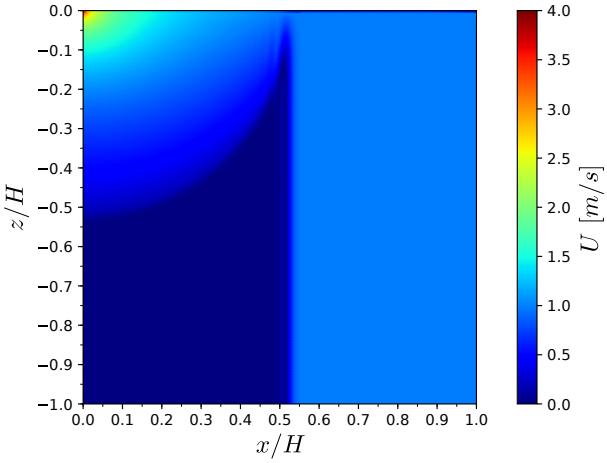

(b) Velocity magnitude

Figure 2.8: Pressure and velocity magnitude on the liquid region using a cell size $\Delta x/H = 2 \times 10^{-3}$ at $t = 2.5 \times 10^{-5}\, s$

In this situation, the water volume impinges the wall with an abrupt pressure rise and an increase of water density in the vicinity of the wall. This produces a pressure wave which propagates through the water domain similarly as a sound wave. As the pressure wave moves away from the impacted wall, it trails a small region of the liquid that starts a fast compression-expansion behaviour. A pressure gradient will form from the free surface top edge advancing towards the bottom boundary as the pressure wave moves, allowing gradually the entrapped water to gain velocity upwards. In Fig. 2.8a it is observable the pressure wave in the water region at $t = 2.5 \times 10^{-5}$ s advancing symmetrically to the bottom boundary with an approximate speed of 1100 m/s. Fig. 2.8b presents the velocity field magnitude at the same instant. Here the region unaffected by the pressure wave still

has initial inertial velocity of 1 m/s pointing towards the left wall. The compressed region has almost a null velocity, and, at the free boundary top edge the water jet is gaining velocity upwards (top left of Fig. 2.8b).

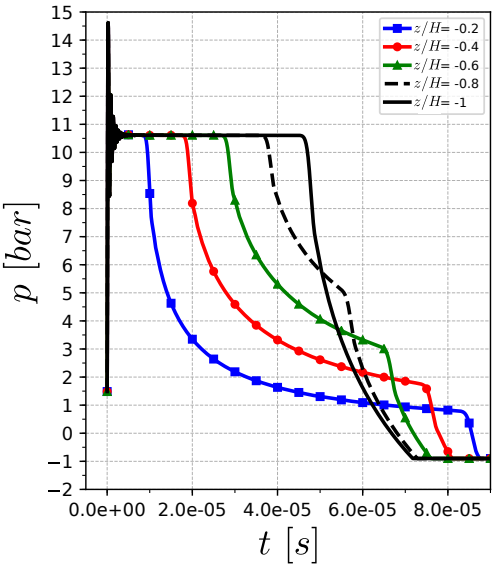

Figure 2.9: Different elevations ($\Delta x/H = 2 \times 10^{-3}$)

Figure 2.9 depict different gauge pressure ($p = p_{abs} - p_0$) series from different locations of the left wall. During the very first impact times ($0 < t < 2 \times 10^{-6}$ s), high pressure oscillations with small period (≈ 1 µs) are recorded on the different locations, simultaneously for all the impact region. As the pressure wave moves forward it decelerates the incoming fluid and liberates gradually the entrapped liquid behind. The liquid region close to the bottom wall will remain under pressure until the pressure wave front is far enough. The situation presented here, as the water domain is square shaped the pressure drop at $z/H = -1$ occurs approximately at $t = 4.5 \times 10^{-5}$ s when the pressure wave reaches the right liquid boundary. At this instant an expansion front moves vertically, from the bottom boundary towards the free surface, dropping the pressure into subatmospheric values which may lead to a phase change.

The second graph, Fig. 2.10, presents the pressure impact results at $z/H = -1$ for different spatial discretisations and linked time steps (see Table 2.3). This study depicts a good convergence of the results in terms of the peak pressure, which is close to the acoustic pressure solution of $p = \rho \cdot C \cdot u = 15$ bar. On the other hand, the rise time t_{imp} decreases as the mesh is refined with the same factor. The oscillations frequency increases as the cell length decreases, as well as the compression-expansion trailing region becomes smaller.

Finally, Fig. 2.11, presents the pressure impact results at $z/H = -1$ for different temporal discretisations using $\Delta x/H = 4 \times 10^{-3}$ mesh. It is observable a direct relation between the peak pressure and the simulation time step. When the time step is reduced the peak pressure slightly increases within an error $E = (p_{acoustic} - p_{numeric})/p_{acoustic}$ lower than 10%. Time step values in the order of $n \cdot (\Delta x/C)$ present good results with an error of 2.6% if selecting the constant $n = 0.1$, as in [79]. Although, a value of $n = 0.0375$ presents in this case a perfect agreement with the acoustic pressure prediction of 15 bar (see Table.2.4). The simulation using $\Delta t = 5 \times 10^{-10}$ s takes 920 steps before the peak pressure and, thus, the numerical diffusion should be taken into account.

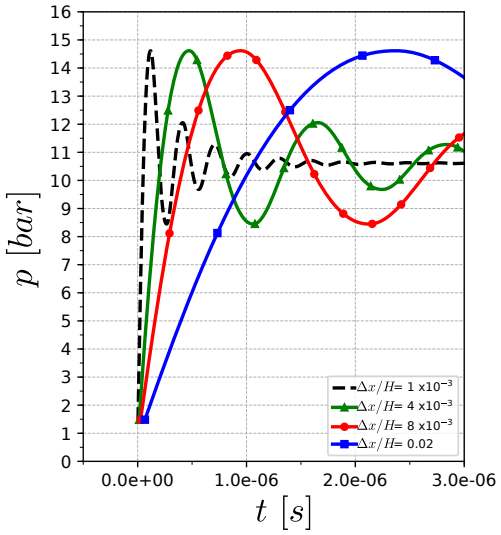

Figure 2.10: Mesh convergence ($z/H = -1$)

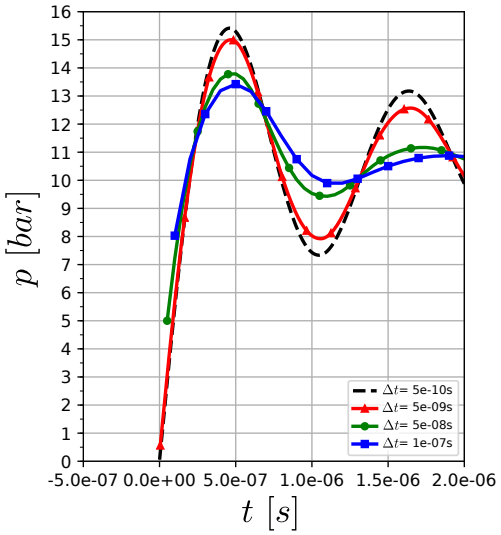

Figure 2.11: Time step convergence ($z/H = -1$)

$\Delta x/H$	Δt $[s]$	t_{imp} $[s]$	p $[bar]$
0.02	6.66×10^{-8}	2.4×10^{-6}	14.613
8×10^{-3}	2.66×10^{-8}	9.6×10^{-7}	14.614
4×10^{-3}	1.33×10^{-8}	4.8×10^{-7}	14.614
1×10^{-3}	3.33×10^{-9}	1.16×10^{-7}	14.612

Table 2.3: Spatial discretisation convergence

Table 2.3 presents a good convergence in terms of peak pressure while refining the spatial discretisation, where, Δx refers to the cell length, Δt the time step, t_{imp} the rise time and p the peak pressure. On the other hand, Table 2.4 presents the peak pressure results while refining the temporal discretisation. This section presented the robustness of the solver to evaluate fluid impulsive pressures when taking into account the compressibility effects.

Δt $[s]$	n	t_{imp} $[s]$	p $[bar]$
1×10^{-7}	0.75	5×10^{-7}	13.42
5×10^{-8}	0.375	5×10^{-7}	13.78
5×10^{-9}	0.0375	4.7×10^{-7}	15
5×10^{-10}	0.00375	4.6×10^{-7}	15.41

Table 2.4: Temporal discretisation convergence

2.3 1D air-liquid piston

This section introduces a configuration of a 1D water piston with an initial velocity compressing and expanding an air cavity. The problem presented here is based on the configuration initially proposed by Bagnold in 1939 [23]. The setup for this liquid-piston problem is shown in Fig.2.12.

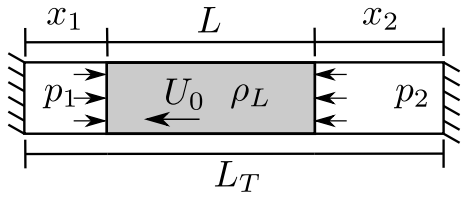

Figure 2.12: 1D liquid piston scheme

A similar problem has been used to benchmark compressibility effects by the liquid sloshing community, see [78, 79, 108, 109]. In the present work, gravity is neglected and the origin of motion is an initial velocity U_0. This initial velocity on the liquid region causes a compression of the air phase x_1 and consequently an increase of pressure p_1, gas density and temperature. During this compression stage, certain conditions can lead to condensation on the air region (see [108]). However, the present model does not take into account such a phenomenon. On the other hand, the gas region x_2 is being expanded reducing pressure p_2 and gas density. Both gas regions gradually reduce the liquid velocity to zero and finally change the motion sense, inverting the process. There are no restitution forces and, under the isentropic assumption, the system oscillates infinitely. The governing equation of motion is obtained from basic principles, reading:

$$\frac{d^2x}{dt^2} = \frac{1}{\rho_{water} L}\Big(p_1(t) - p_2(t)\Big) \tag{2.7}$$

where p_1 and p_2 are respectively the pressures in the left and the right gas regions, ρ_{water} is the liquid density and L the liquid length. This non-linear differential equation can be solved numerically by a time-domain discretisation. The first-order explicit Euler method is employed to calculate a semi-analytic solution. The quantities at time step n are labelled with n and the new time-step is labelled with $n+1$. Assuming an adiabatic evolution for the gas and using the ideal gas equation of state, the pressures can be calculated as

$$p_1^{n+1} = p_1^n\Big(\frac{x_1^n}{x_1^{n+1}}\Big)^\gamma \qquad\qquad p_2^{n+1} = p_2^n\Big(\frac{x_2^n}{L_T - L - x_1^{n+1}}\Big)^\gamma \tag{2.8}$$

where L_T is the total length and γ the specific heat ratio. The initial conditions are $x_1(0) = x_1^0$ and $dx/dt(0) = U_0$. The liquid region has a density of $\rho_{water} = 1000$ kg/m^3. The gas has an initial density of $\rho_{air} = 1.2$ kg/m^3 and an specific heat ratio of $\gamma = 1.4$. The initial velocity is set to $U_0 = 0.5$ m/s and the geometric dimensions are $L_T = 0.1$ m and

$L = 0.05$ m. The violence of the impact can be defined using the *impact number related to the initial velocity* by $S_B = \frac{\rho_{water} L U_0^2}{p_0(x_1^0 + x_2^0)}$. This is the dimensionless number of the initial Bagnold problem (the B index stands for Bagnold). In this situation, the impact number is $S_B = 2.5 \times 10^{-3}$ and based on the work [109] for $S_B < 8$ the liquid can be assumed as incompressible. Using these conditions, the semi-analytic solution using different time steps Δt is calculated and a converged solution is obtained using $\Delta t = 1 \times 10^{-6}$ s.

For solving this situation numerically, the mesh used is one cell length in both perpendicular directions (OY and OZ) and 100 equally distributed cells in the horizontal direction. The time discretisation is fixed at $\Delta t = 1 \times 10^{-6}$ s and an explicit first-order Euler scheme is used for the time derivative. The boundaries are defined as solid walls for both, left and right. With a Dirichlet condition for the velocity of zero, a pressure gradient of zero and an alpha gradient of zero. The OX parallel boundaries are defined as empty to indicate a one-dimensional problem. The pressure values are recorded in all the cell centres at every time step. The diffusion term is neglected as well as the surface tension. It is important to notice that the liquid volume fraction transport equation is solved using MULES and the artificial compression term is not taken into account (i.e. `cAlpha` $= 0$). The compression of the interface has shown to increase the numeric diffusion, presenting an important dampening of the system.

Fig. 2.13 presents the obtained results and these are compared with the semi-analytic solution. The series presented are recorded at the extreme cells, where the red depicts the region x_1 and the blue the region x_2. A good agreement is obtained between the numeric and the semi-analytic solution which is not surprising for this simple configuration. The oscillations periods are in the order of ≈ 10 ms. Nevertheless, slight numeric diffusion can be observed after a few oscillations and high frequency oscillations during the initialisation, see Fig. 2.13a, 2.13b and 2.13c .

Finally, a representation of the pressure values over time along a vertical line is presented in Fig. 2.14. The present situation can be classified as a non-impulsive interaction. Although the air presents a compressible behaviour, the incompressible assumption for water is appropriated as there are no visible pressure waves. Moreover, the gradient of pressure along the water region is linear.

This section has successfully reproduced an air compression/expansion process and presented a first idea of the time scales related. Moreover, it ensured the possibility to appropriately model the free surface during this phenomena.

2.4 2D aerated liquid impact

The present section introduces tentative modelling of an aerated fluid impact. The gained experience obtained from the last two Sec. 2.2 and Sec. 2.3 is used here to define the numerical setup and analyse the obtained results. The employed configuration is similar to the one presented in the idealised liquid impact Sec. 2.2 and it basically consists of a gas-liquid mixture region surrounded by three walls and an air region, see Fig. 2.15 for details. The aerated liquid is defined by uniformly distributed (49 columns $\times$ 19 rows) circular areas of air ($\alpha = 0$) over the liquid region mimicking the presence of bubbles. The bubbles closer to the impact wall are half-split by diameter, see Fig. 2.15. The main geometric parameters are summarised in Tab. 2.5, where D is the bubbles diameter, d the separation between the bubbles centre, L the domains length, L_{fluid} the liquid length and H the domains height. Finally, the whole aerated fluid has an initial velocity U_0 pointing perpendicularly towards the left boundary.

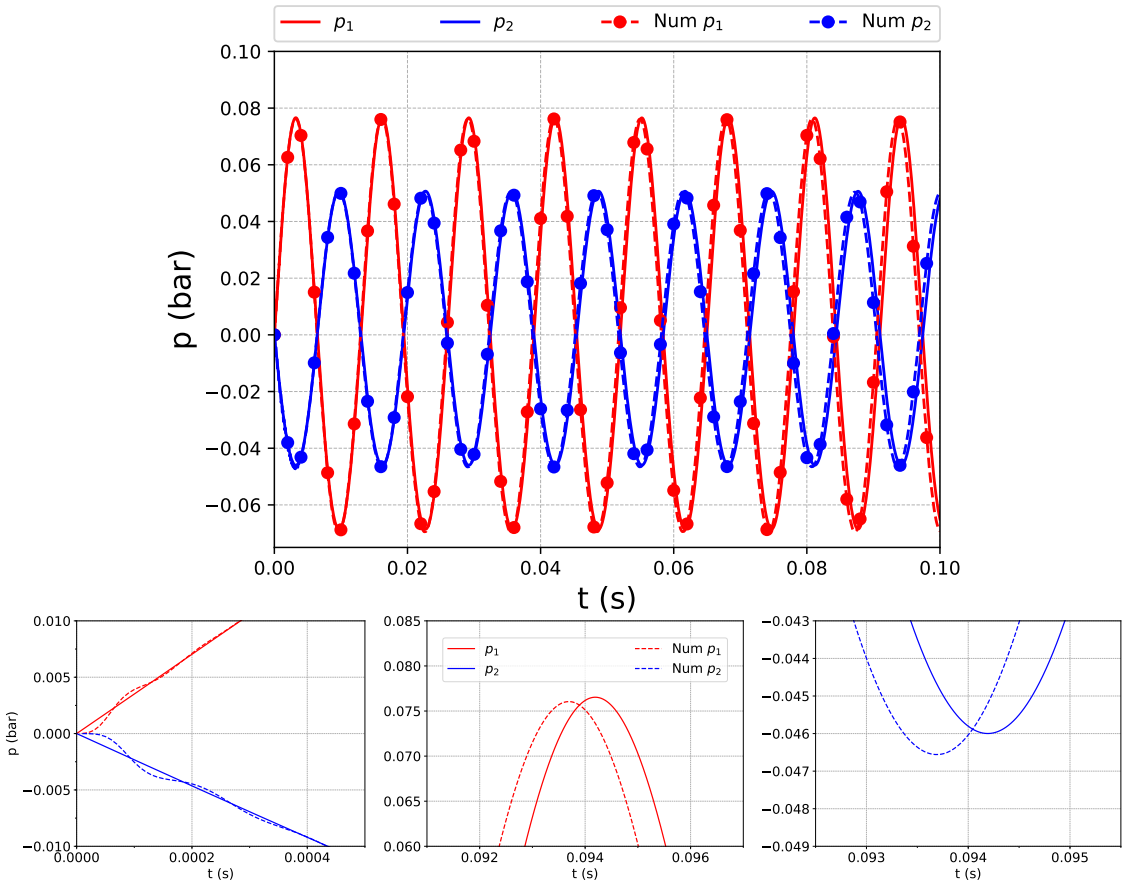

Figure 2.13: Pressure values recorded at the highest and lowest cells compared with the semi-analytic solution using $\Delta t = 1 \times 10^{-6}$ s.

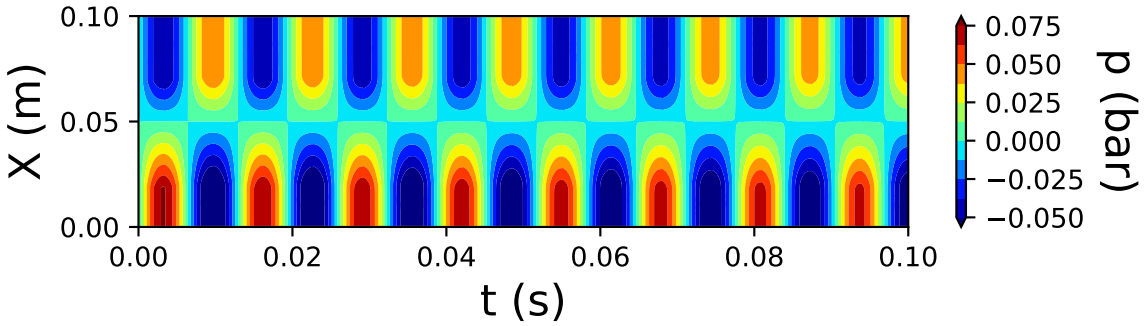

Figure 2.14: Pressure values recorded at the highest and lowest cells compared with the semi-analytic solution using $\Delta t = 1 \times 10^{-6}$ s

The boundary conditions are defined as solid walls for the bottom, left and top edges using a slip condition for velocity, a gradient of zero for pressure and a gradient of zero for the liquid volume fraction. The right boundary is kept as an open boundary with a total pressure condition where air and water can freely flow out and only air can flow in, and the lateral sides are set to indicate a two-dimensional problem.

The mesh is orthogonal and uniform with square-shaped cells $\Delta x = \Delta z$. It consists of 800.000 cells and the bubbles are discretised using a ratio of $D/\Delta x = 10$, see Fig. 2.15.

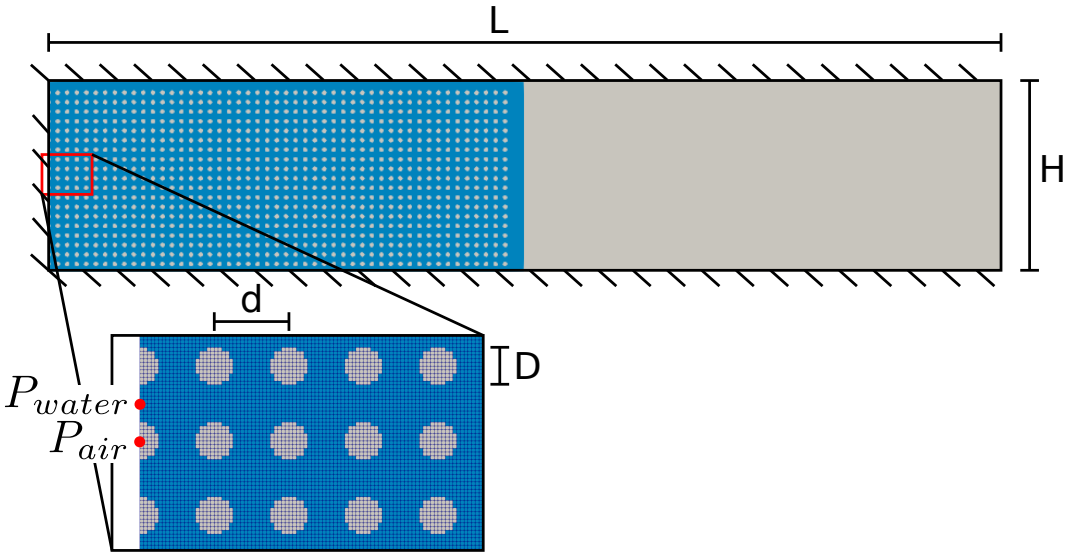

Figure 2.15: Detail of the liquid region initialisation.

Table 2.5: Configuration parameters

D (mm)	0.25
d (mm)	0.5
L (mm)	100
L_{fluid} (mm)	50
H (mm)	20
U_0 (m/s)	1

These computations will run using a fixed time step $\Delta t = 3 \times 10^{-9}$ s related to the Courant number and the water speed of sound. Sec. 2.2.2 concluded this time step to be small enough to capture the water compressibility effects. An implicit second-order pure Crank-Nicolson scheme is employed for the time derivative. Similarly as in Sec. 2.3, the compression term is not taken into account in the liquid volume fraction transport equation `cAlpha` $= 0$.

The configuration is solved using a compressible solver. The equation of state for the liquid region follows Tait's equation and the air an ideal gas equation of state. The system temperature is $20\,°C$ and the initial pressure is set to atmospheric $p_0 = 1$ bar. The air properties are, $\rho_{air} = 1.2$ kg/m^3 for initial density and a constant specific heat ratio of $\gamma_{air} = 1.4$. For water, $\rho_{water} = 1000$ kg/m^3, a constant specific heat ratio of $\gamma_{water} = 7$ and a speed of sound of $C_{water} = 1500$ m/s. It is assumed that the fluid viscosity is irrelevant in this inertial problem. Similarly, the surface tension is neglected and, as in previous sections, the gravity is set to zero.

The objective for the following paragraphs is the description of the results obtained. The arguments that support the following analysis are based on Figs. 2.16, 2.18a, 2.18b and 2.17. Fig. 2.16 presents the recorded gauge pressure ($p = p_{abs} - p_0$) values at two locations on the impact wall, one in the liquid region and the other in the air region, see Fig. 2.15. Next, Fig. 2.18a represents the pressure fields related to the first pressure peaks using a logarithmic scale for pressure and Fig. 2.18b the pressure fields with a different scale immediately after the initial impact. Finally, Fig. 2.17 presents the evolution of the bubbles volumes that are in contact with the impact wall.

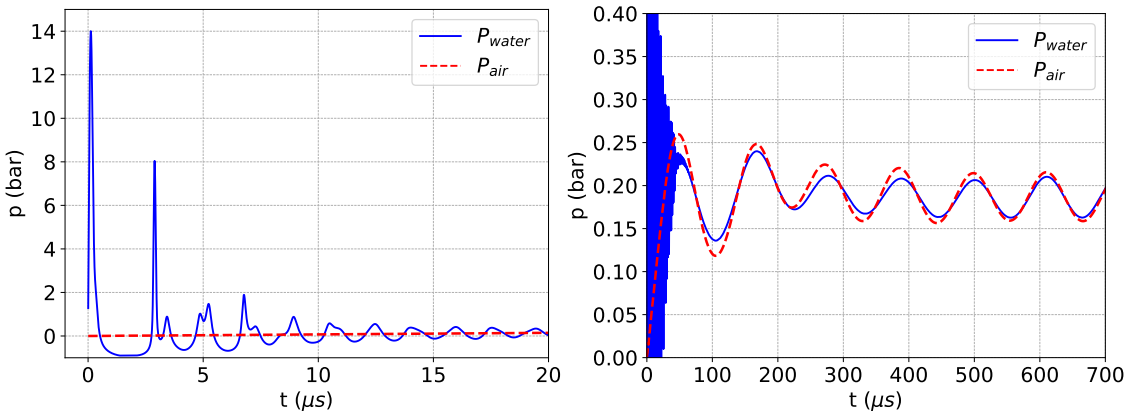

(a) Liquid compressiblity scale

(b) Air compressibility scale

Figure 2.16: Pressures series at two locations referenced in Fig. 2.15. Note the different pressure and time scales.

At $t = 0.1$ µs, the highest pressure value of 14 bar is observed in the liquid sensor P_{water}. This value is related to the acoustic pressure theory $p = \rho C u$ for water and agrees with the results presented in Sec. 2.2.2. Regarding the pressure fields and the pressure temporal series, the momentum is being fully absorbed by the liquid-solid contact and the sensor located inside the air bubbles barely presents a pressure rise. Moreover, by looking at Fig. 2.17 one can extract that the wall bubbles volume is unchanged at this stage.

At $t = 1$ µs, the liquid pressure sensor reaches the minimum value immediately after the first peak pressure in Fig. 2.16a following a liquid expansion process. It is important to notice that at this stage, the pressure values fall rapidly and the solver limits the value to 0.1 bar as a minimum threshold. Trespassing this value would probably lead to a phase change of water and this is not taken into account in the present model. On the other hand, a pressure wave starts travelling away from the impact region through the liquid medium and the air bubble in contact with the wall experiences a gradual pressure rise and a volume reduction.

Following this stage, at $t = 2.9$ µs, the pressure wave starts a complex interaction process of reflection and diffraction with the air bubbles. This is most likely the origin of the forthcoming pressure peaks in Fig. 2.16a. The air bubbles in contact with the wall only reduced their volume by less than 2% under compression at this points.

The following relevant processes are related to the air behaviour and the time scale is approximately two orders of magnitude bigger ≈ 0.1 ms. Looking at the pressure signal from Fig. 2.16b, the highest pressure at the air sensor P_{air} is 0.26 bar. Whereas, the sensor at the liquid contact experiences a similar rebound this has a slightly lower magnitude of approximately 0.23 bar. The pressure fields in Fig. 2.18b present a uniformly distributed pressurisation along a vertical plane. This has a visible effect on the bubbles by reducing their initial volume by 30%.

This new pressure wave, with an approximate period of ≈ 0.1 ms, starts travelling away from the impact plane trailing an expansion which increases the bubbles volume, see Fig. 2.18b at $t = 100$ µs. Again, this expansion wave is followed by a new compression of the impact plane.

From the complex phenomenon described in this section, one can conclude that the air inclusion during a fluid impact has a major effect in the exerted load. The pressure signals inside and outside the air impact area are extremely different during the first stages of the

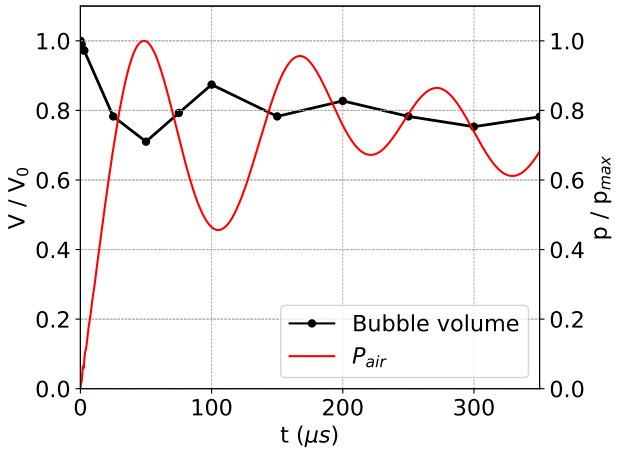

Figure 2.17: Air area evolution over time

impact and the compressible properties of the liquid are of great importance. After the initial instants, the whole fluid mixture behaves similarly and the air compressibility is an important actor at the stage. Two differentiated time scales are appreciated and these are related to the compressibility of the different fluids. It is important to notice that this last section is considered as a concept proof and it has not been directly taken into account in the forthcoming chapters.

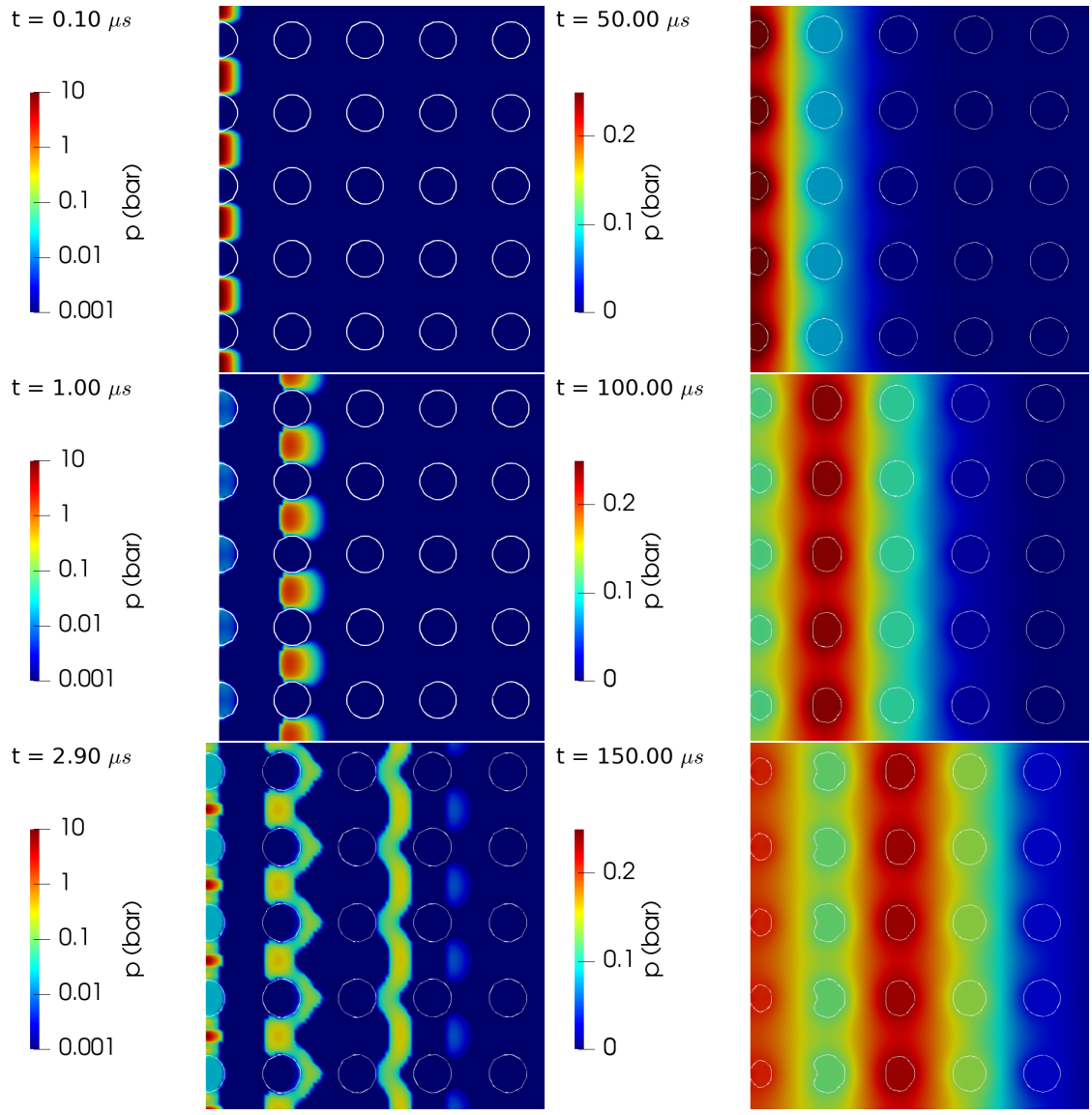

(a) Pressure fields evolution during the liquid impact.

(b) Pressure fields evolution during the air compression/expansion phase.

Figure 2.18: Evolution of the pressure fields during an 2D aerated fluid impact.

Chapter 3

Solitary wave impact

This chapter presents a complete validation study of local pressure fields related to a solitary breaking wave impact. This work has been partly published in the scientific Journal of Coastal Engineering, see [106]. After a short recall of the solitary wave theory, the performance of the solver for generation and propagation of solitary wave over an horizontal plane is presented. Next, an overview of the experimental setup is presented extending the previous configuration by adding a sloped plane causing the wave overturning. Finally, making use of all the acquired experience, two main configurations of wave breaking impacts are compared with the experiments. An air-pocket or high aerated impact is modeled numerically comparing the results against the experiment for an incompressible and a compressible solver. This is first evaluated in a two dimensions configuration and the compressible simulation is finally extended to a three dimensions geometry. Then a flip-through or low aerated impact is also compared with experimental data using a compressible solver in a two dimensions configuration.

3.1 Solitary wave generation and propagation

The objectives of this section are to evaluate the performance of various relevant aspects necessary for accurate reproduction of a numerical solitary wave based on the Boussinesq theory. Initially, a brief description of the Boussinesq solitary wave equations is introduced. Secondly, a test case is employed to evaluate the performance of wave generation and propagation on a general 2D rectangular numerical wave tank.

3.1.1 Solitary wave theory

A solitary wave is classified as a gravity translational wave, meaning the horizontal velocity over a cross-section is almost uniform on the contrary to the surface waves, where the motion decreases from the surface downward. Solitary wave free surface and velocity equations were first derived by Joseph Bousinnesq in 1871 [110]. The present section start the development of these equations from the general system of equations at the free surface elevation $z = \eta(x,t)$ for incompressible and irrotational water waves in the 2D plane (x,y). The first equation states that the surface is always made up of the same fluid particles and may be called the *kinematic boundary condition*:

$$\frac{\partial \eta}{\partial t} + \left(\frac{\partial \Phi}{\partial x}\right)_{z=\eta} \frac{\partial \eta}{\partial x} - \left(\frac{\partial \Phi}{\partial z}\right)_{z=\eta} = 0 \ , \tag{3.1}$$

where Φ is the velocity potential. The second equation is derived from the *Bernoulli's equation* and states that the pressure at the free surface is equal to the atmospheric pressure. It is often referred to as the *dynamic boundary condition*,

$$\frac{\partial \Phi}{\partial t} + \frac{1}{2}\left[\left(\frac{\partial \Phi}{\partial x}\right)^2 + \left(\frac{\partial \Phi}{\partial z}\right)^2\right]_{z=\eta} + g\eta = 0 \ , \tag{3.2}$$

where $u = \partial\Phi/\partial x,\ v = \partial\Phi/\partial z$ are the horizontal and vertical flow velocity components respectively and g is the gravity acceleration. The essential idea in the Boussinesq approximation is the elimination of vertical coordinates from these equations, eq. (3.1) and (3.2), by using a Taylor expansion of the velocity potential and the following three steps.

1. Consider the Taylor expansion of the velocity potential $\Phi(x,y,t)$ around the bed level $z = -h$ (h is the water depth) :

$$\Phi = \Phi(x,-h,t) + (z+h)\left[\frac{\partial \Phi}{\partial z}\right]_{z=-h} + \frac{1}{2}(z+h)^2\left[\frac{\partial^2 \Phi}{\partial z^2}\right]_{z=-h} + \frac{1}{6}(z+h)^3\left[\frac{\partial^3 \Phi}{\partial z^3}\right]_{z=-h} + \frac{1}{24}(z+h)^4\left[\frac{\partial^4 \Phi}{\partial z^4}\right]_{z=-h} + ...$$

2. Using the incompressible continuity assumption, the vertical partial derivatives are substituted with horizontal velocities:

$$\Phi = \Phi(x,-h,t) - \frac{1}{2}(z+h)^2\left[\frac{\partial^2 \Phi}{\partial x^2}\right]_{z=-h} + \frac{1}{24}(z+h)^4\left[\frac{\partial^4 \Phi}{\partial x^4}\right]_{z=-h} + ... + (z+h)\left[\frac{\partial \Phi}{\partial z}\right]_{z=-h} - \frac{1}{6}(z+h)^3\frac{\partial^2}{\partial x^2}\left[\frac{\partial \Phi}{\partial z}\right]_{z=-h} + ...$$

3. Finally, considering the vertical velocity at the bottom to be zero $\partial\Phi/\partial z = 0$:

$$\Phi = \Phi_b - \frac{1}{2}(z+h)^2 \left[\frac{\partial^2\Phi}{\partial x^2}\right]_{z=-h} + \frac{1}{24}(z+h)^4 \left[\frac{\partial^4\Phi}{\partial x^4}\right]_{z=-h} + ...$$

Substituting this development into the flow equations, eq. (3.1) and (3.2), leads to Boussinesq set of equations which read,

$$\frac{\partial\eta}{\partial t} + \frac{\partial}{\partial x}[(h+\eta)u_b] = \frac{1}{6}h^3\frac{\partial^3 u_b}{\partial x^3} \quad \text{and} \tag{3.3}$$

$$\frac{\partial u_b}{\partial t} + u_b\frac{\partial u_b}{\partial x} + g\frac{\partial\eta}{\partial x} = \frac{1}{2}h^2\frac{\partial^3 u_b}{\partial t\partial x^2}\ , \tag{3.4}$$

where u_b is the velocity at the bottom.

3.1.2 Numeric solitary wave generation

The set of equations, eq. (3.3) and (3.4), have had multiple solutions, however, the present work uses those proposed in Lee *et al.* 1982 [111]. For the free surface this reads,

$$\eta = a\ sech^2\left[\sqrt{\frac{3a}{4h^3}}X\right] \quad \text{(in which } X = -c\ t + x + t_s)\ , \tag{3.5}$$

where a is the solitary wave amplitude and $c = \sqrt{g(h+a)}$ is the wave celerity according to the shallow water theory. The wave generation boundary is assumed to be at $x = 0$ and t_s is a time lag. This last term t_s is necessary to avoid initialising the solitary wave from the highest point. The natural selection of this term is the propagation time of half of the wavelength, however, the long wave condition assumes the solitary wave to have an infinite wavelength. Then, an effective wavelength is defined by using a percentage of the wave amplitude which is usually around 1%, leading to values of $t_s \approx 3.5h/\sqrt{a/h}$. Finally, the velocity components are straightforward, although they involve derivatives of the free surface. The velocity components are:

$$\frac{u}{\sqrt{gh}} = \frac{\eta}{h}\left[1 - \frac{1}{4}\frac{\eta}{h} + \frac{h^2}{\eta}\left(1 - \frac{3}{2}\frac{z^2}{h^2}\right)\frac{d^2\eta}{dX^2}\right] \quad \text{and} \tag{3.6}$$

$$\frac{v}{\sqrt{gh}} = -\frac{z}{h}\left[\left(1 - \frac{1}{2}\frac{\eta}{h}\right)\frac{d\eta}{dX} + \frac{1}{3}h^2\left(1 - \frac{1}{2}\frac{z^2}{h^2}\right)\frac{d^3\eta}{dX^3}\right] \tag{3.7}$$

The present work uses a static boundary method (see Sec. 1.3.1) as a boundary condition to generate the Boussinesq solitary wave. This boundary condition mimics a piston wave maker to impose the free surface elevation according to eq. 3.5 and the velocity components from eq. 3.6 and 3.7.

3.1.3 Numerical performance of a solitary wave propagation

In this section, the incompressible two-phase solver `interFoam` is evaluated in a solitary wave propagation process over a horizontal plane. The initial configuration is kept by default from the one proposed in `tutorials`. However, the length of the domain is extended to a larger wave propagation stage. The numerical wave channel length is 20 m and has a height of 1.5 m. The water depth is kept constant with $h = 0.7$ m. Fig. 3.1 presents the

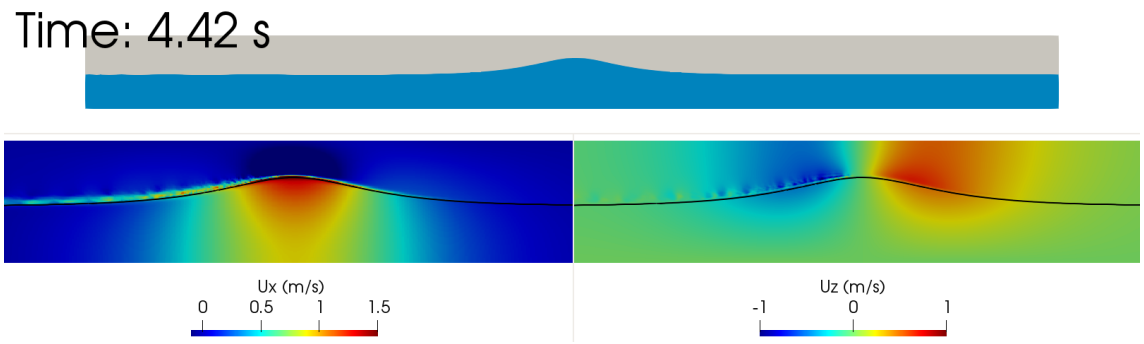

Figure 3.1: Boussinesq solitary wave horizontal and velocity fields detail. The black line is an isocontour of the liquid volume fraction ($\alpha = 0.5$).

solution obtained at an intermediate instant with a representation of liquid fraction, horizontal and vertical velocity fields. From the horizontal velocity field, it is observable the almost constant values along the transverse planes characteristic of a translational wave. The second relevant aspect, is the air drag effect caused by the traveling wave which is not taken into account by the theory based on a single fluid.

The mesh is structured and uniform keeping the same cell size over the entire domain. The cells size is directly related to the solitary wave amplitude, with an initial ratio of $a/\Delta z = 30$. The cell are rectangular with an aspect ratio between the horizontal Δx and vertical Δz cell length of $\Delta x/\Delta z = 2$. Regarding the time discretisation, the time step is limited using a maximum Courant number `maxCo` $= 0.65$ and a `maxAlphaCo` $= 0.65$ around the interface. The boundary conditions, are kept as a static wave generation boundary for the inlet, imposing velocities and alpha values, and an absorbing boundary for the outlet. The top boundary is kept as an open boundary imposing a total pressure condition and the bottom boundary is set to a solid wall with a slip condition for velocities.

Different wave amplitudes are initially tested, starting from the tutorial value of $a = 0.3$ m. The wave relative depth is an important parameter that has to be evaluated before proceeding into any analysis. In the current case, using $a = 0.3$ m the solitary wave has an equivalent wave length, using the aforementioned approximation of 1% of the wave amplitude, of $\lambda = 7.76$ m and then a relative depth of $h/\lambda = 0.09$. This value remains out of the shallow water range $h/\lambda < 0.05$ inducing a non-negligible frequency dispersion effect, see Fig. 3.2a. In this figure, the numerical free surface elevation 10 m away from the wave generator is compared with the analytic solution using eq. (3.5). If reducing the solitary wave amplitude to $a = 0.1$ m, the equivalent wavelength is $\lambda = 13.4$ m and the agreement with the analytical solution is greatly improved, see Fig. 3.2b.

The upcoming analysis makes use of the relative error comparing the analytical and numerical solutions for the solitary wave amplitude and celerity:

$$Err(\eta) = \frac{|\eta_{analy} - \eta_{num}|}{\eta_{analy}} \cdot 100 \qquad Err(c) = \frac{|c_{analy} - c_{num}|}{c_{analy}} \cdot 100 \ ,$$

where η_{num} and c_{num} are calculated using the highest elevation of the free surface and $\bullet_{analy}$ represents the analytical counterparts.

Next, Fig. 3.3 presents these errors for different relative depths 10 m away from the wave generator, similarly as in Fig. 3.2. Globally, all the relative depths tested have errors below 10% for both amplitude and solitary wave celerity. Nevertheless, the error decreases using smaller relative depth configurations which make sense based on the shallow water

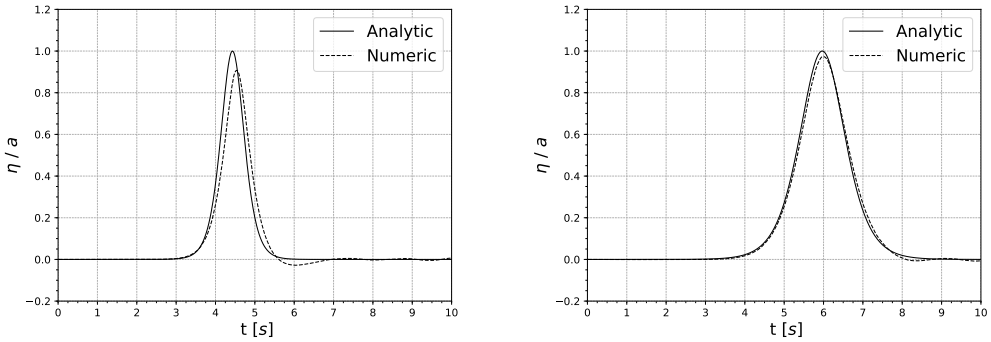

(a) $h/\lambda = 0.09$ (b) $h/\lambda = 0.05$

Figure 3.2: Free surface elevation 10m away from the wave generator for two different relative depths.

theory. The highest relative depth appears to be out of the general trend and this is caused by initialisation of wave breaking.

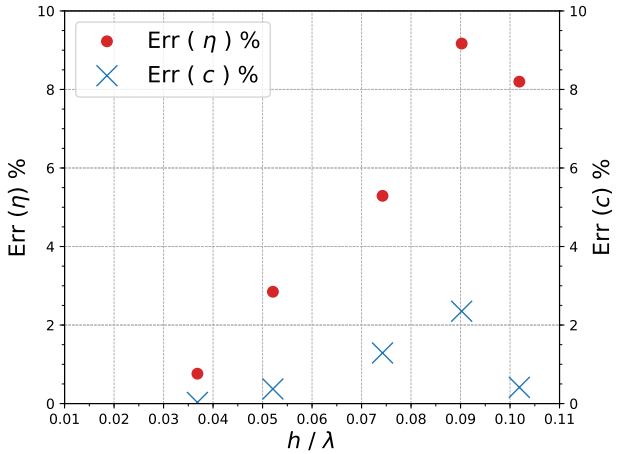

Figure 3.3: Solitary wave amplitude and celerity errors for different relative depths 10m away from the wave generation boundary.

Fig. 3.4 presents different free surface elevations over time captured at different distances from the wavemaker. Using this information, conservation of the solitary wave amplitude and celerity can be studied. Thus, a spatial and temporal convergence analysis is now presented using a wave configuration with an amplitude $a = 0.1$ m, a depth $h = 0.7$ m, an equivalent wave length $\lambda = 13.4$ m and a relative depth $h/\lambda = 0.052$.

Fig. 3.5a presents the corresponding relative errors at different locations using different spatial discretisations. The smaller ratio of cells per wave amplitude $a/\Delta z = 15$ can keep errors under a 5% threshold although these are doubled over a 15 m length propagation. The higher refinements reduce the errors compared with the analytical solution and can maintain the wave amplitude with an error smaller than 2% for the last wave gauge. Regarding the wave celerity there is, apparently, no remarkable improvement while refining the spatial discretisation. These results are in agreement with the literature [112], where 15 cells per wave height have shown to be sufficient to maintain the wave height over a long propagation. Fig. 3.5b presents the horizontal velocity 10 m away from the wavemaker when the free surface reaches its maximum elevation. Comparing the numerical results with the analytical solution, the agreement is fairly good for all the discretisations. While

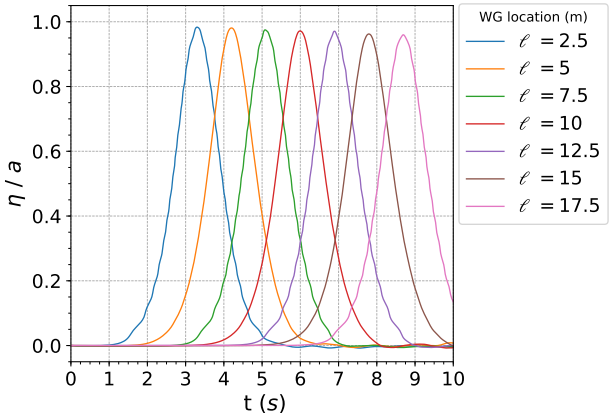

Figure 3.4: Propagation of a Boussinesq solitary wave. Wave parameters: $a = 0.1$ m and $h = 0.7$ m. l corresponds to the wave gauge (WG) distance from the wave maker.

refining the spatial discretisation, a slight improvement of the numerical results towards the analytical solution is reported. Nevertheless, the horizontal velocities close to the interface cells experience a sudden increase represented as a horizontal overshot. This is not surprising and repeatedly observed during this whole work. However, cell sizes reduction, which consequently refines the interface region, tends to reduce this horizontal velocity overshot. The main cause of this phenomenon is attributed to the huge air and water density difference which leads to a local imbalance of the momentum equation near the interface. As mentioned in previous sections, this has been investigated by other authors, one of the relevant study being [68].

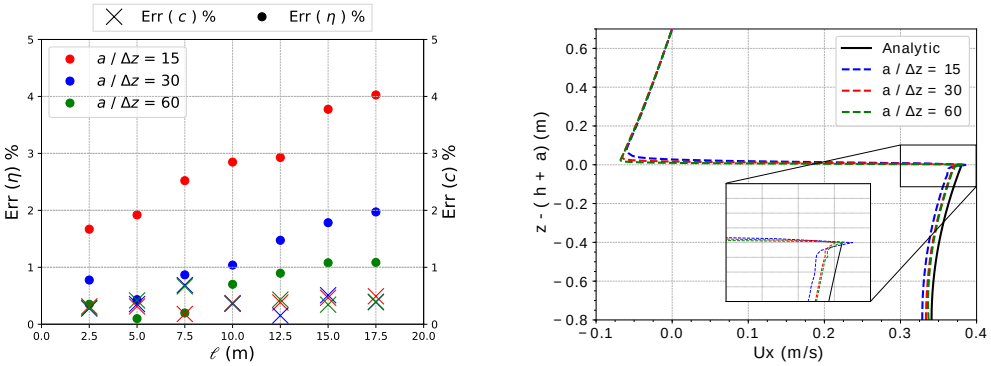

(a) Relative errors

(b) Horizontal velocities at $l = 10$ m

Figure 3.5: Spatial convergence analysis of (left) wave amplitude and celerity relative errors at different distances from the wave maker and (right) horizontal velocities at $l = 10$ m when $\eta = \eta_{max}$. Wave parameters: $a = 0.1$ m and $h = 0.7$ m.

Now, the solitary wave propagation and horizontal velocities are compared using different temporal discretisations in Fig. 3.6. These results are obtained using the spatial refinement $a/\Delta z = 15$. Again, from Fig. 3.6a, one can conclude that the temporal refinements do not have a remarkable effect on the wave celerity. Nevertheless, a great improvement in the wave amplitude conservation is observed when reducing the `maxCo` with a relative error maintained close to 1% for the smaller time steps. Fig. 3.6b presents a slight improvement of the horizontal velocity profile using high temporal refinements. Regarding the horizontal velocity peak near the interface, the time step refinement does

not seem to improve the solution.

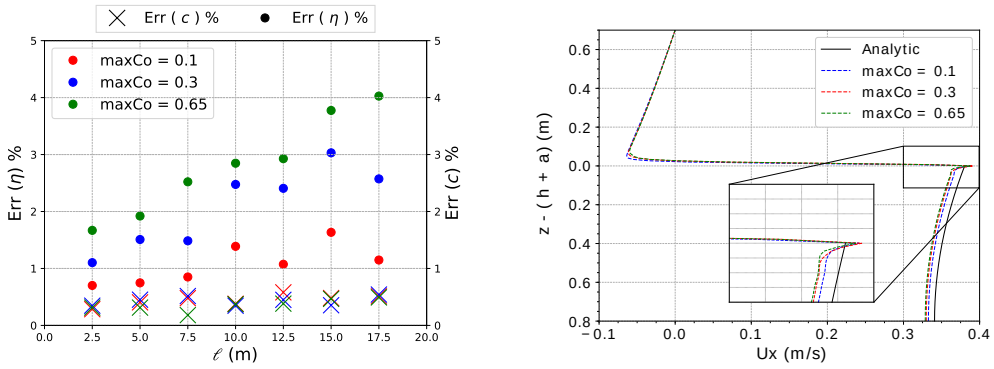

(a) Relative errors

(b) Horizontal velocities at $l = 10$ m

Figure 3.6: Temporal refinement analysis of (left) wave amplitude and celerity relative errors at different distances from the wave maker and (right) horizontal velocities at $l = 10$ m when $\eta = \eta_{max}$. Wave parameters: $a = 0.1$ m and $h = 0.7$ m.

This section presented the range of applicability for generating and propagating a Boussinesq solitary wave using a static wave generation boundary and MULES for maintaining a sharp interface. The following sections will make use of these results as a basis for a more detailed study of the different aspects when simulating more complex configurations.

3.2 Experimental setup

The next section focuses into a laboratory configuration wave impact phenomenon using experimental data from [46]. The experimental setup and results are introduced here to contextualise the numerical work. The experiments were performed in a 17 m long, 0.65 m width and 1.2 m height wave flume, with a 1/15 slope starting at 3.95 m away from the wave generator, see Fig.3.7 and Fig.3.8.

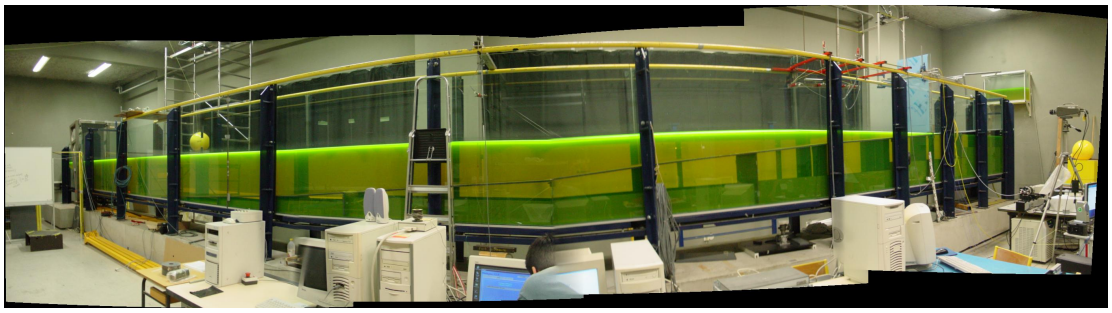

Figure 3.7: Panoramic view of the wave tank

A Boussinesq solitary wave was generated using a flap type wave maker. This will propagate along the wave channel and, under certain conditions, overturn by the presence of the sloped plane. A flexible plate with an embedded base and a simple support was located 14.5 m away from the wave generator, see Fig.3.9a. Multiple pressure gauges were added on the plate to record pressure series with an acquisition frequency of 16 kHz. One of the objectives during the experiments was the study of the plate deflection and, to allow this, two backlashes of 2 mm were left between the plate and the lateral walls Fig.3.9b.

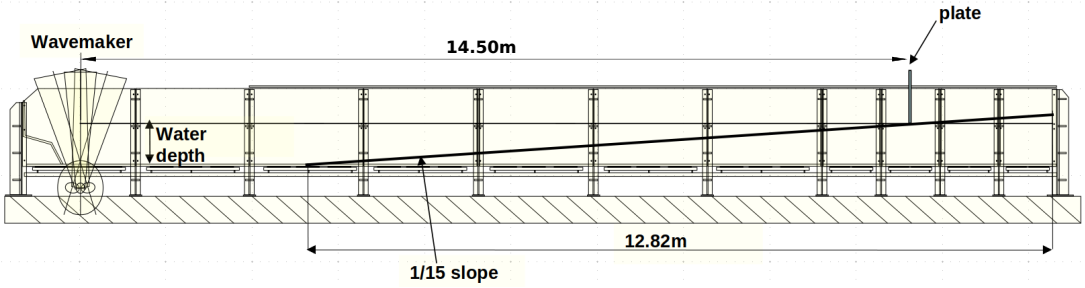

Figure 3.8: Experimental wave channel sketch X-Z

Furthermore, this separation allowed the air and water to flow through during the impacts. This fact had a noticeable effect during the impact process and will be further analysed.

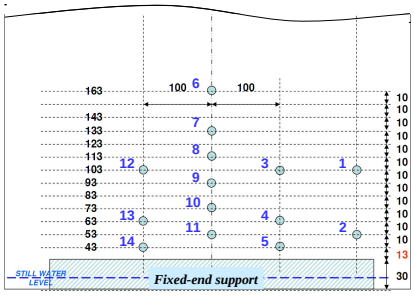

(a) Pressure sensors location on the impact plate Y-Z. Units in *cm*

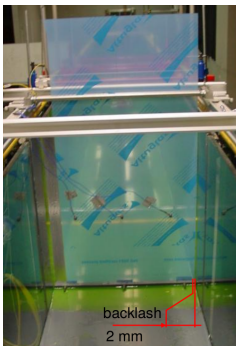

(b) Detail of the impact plate without pressure sensors indicating the backlash. The same backlash length is kept on the other side of the plate, here hardly visible due to the plate transparency.

Figure 3.9: Experimental wave channel sketch

Multiple breaking configurations were tested during the experiments, reproducing the four representative types of wave loads, such as, slightly breaking, low aerated or flip-through, high-aerated or air-pocket and broken, see Fig. 3.10. Here, two breaking types are evaluated, using the definitions given by G.N. Bullock [45]: the air-pocket or high-aerated configuration (see Fig. 3.10c) and the flip-through (see Fig. 3.10b). The selection of a solitary wave facilitates the analysis of a singular impact event, without any reflected or incoming wave train. The experimental wave parameters for the air-pocket case defined in the flat bottom part, were set such as $a = 0.0864$ m for the amplitude and a water depth of $h = 0.7185$ m, resulting in a wave steepness of $a/h = 0.1202$. Using 1% of the maximum wave height to determine an equivalent wave length λ, a value of $\lambda = 15$ m is obtained together with the celerity in shallow water $c = 2.8$ m/s and the equivalent period $T = 5.349$ s. This leads to a relative depth of $h/\lambda = 0.0479$ which is relatively well reproduced based on the previous Sec. 3.1.3. Secondly, for the flip-through case, the amplitude is $a = 0.0627$ m, the water depth is $h = 0.7185$ m and a steepness of $a/h = 0.0872$ is obtained. The calculated equivalent wave length is $\lambda = 17.64$ m and the relative depth $h/\lambda = 0.04$. These two plunging waves have in common an impulsive behaviour when interacting with a wall while their overturning process.

Fig.3.11 and Fig.3.12 represent the velocity field instants before the impact extracted from Particle Image Velocimetry (PIV) and the plate pressure distribution for the two

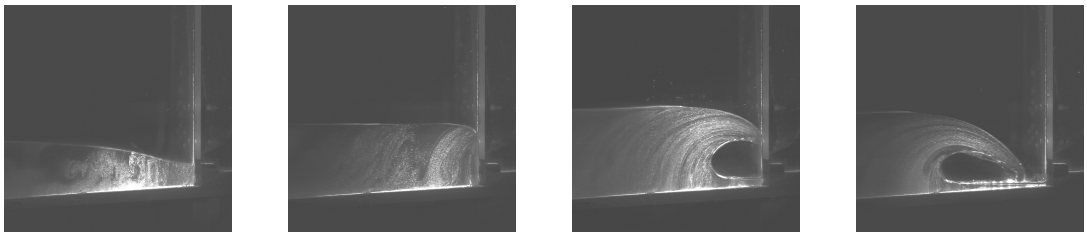

(a) Slightly breaking.

(b) Low aerated or flip-through.

(c) High-aerated or air-pocket.

(d) Broken.

Figure 3.10: Waves impingement classification

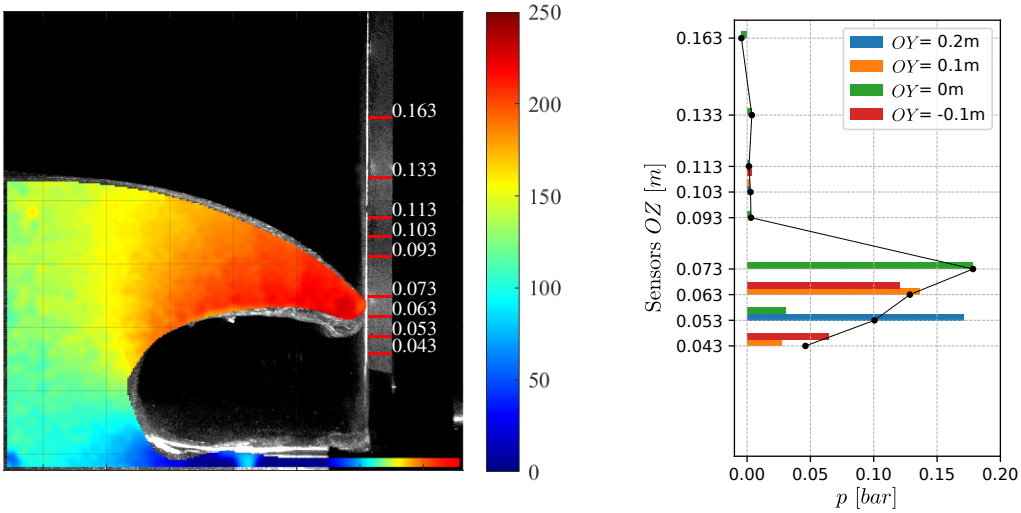

(a) Particle Image Velocimetry of an air-pocket impact. Colour range in cm/s

(b) Pressure distribution on the impact plate. The colors correspond to different pressure gauges that are at the same elevation but for different cross positions. The black line is an average of the pressure data.

Figure 3.11: Experimental high-areated or air-pocket impact

breaking at the highest peak pressure instant. In the PIV images (left picture), the red horizontal lines on the plate indicate the location of the pressure sensors. In the air-pocket case Fig.3.11, it is observable, on the velocity field of the left picture, how the highest velocities are located on the jet with values around 2 m/s pointing towards the plate. This case entraps high volumes of air between the liquid and the wall. The flip-through configuration presents velocities of approximately 1.6 m/s pointing towards the plate in a small localised area. In this situation, a small volume of air is entrapped.

Regarding the pressure distribution, each colour represent different width coordinates (Fig. 3.11b, 3.12b) on the plate and the black line is the average value at each height. In the air-pocket, the highest peak pressure is only recorded by one sensor at $Z = 0.073$ m in the central section. The pressure sensors inside the air cavity, $Z = 0.053$ m and $Z = 0.043$ m, have significant differences between sections caused by the air escape on the side of the wall. Besides this, a general 2D assumption seems acceptable regarding the pressure sensor in the impact point, $Z = 0.063$ m, which captured very similar magnitudes in

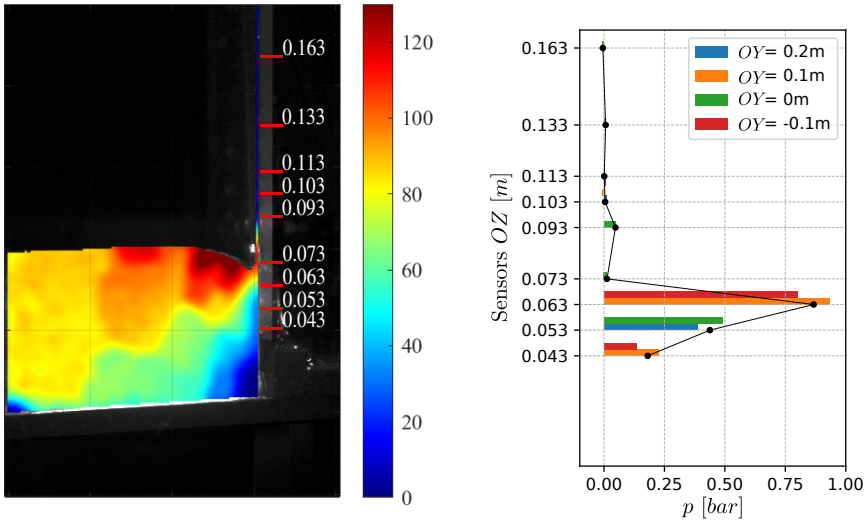

(a) Particle Image Velocimetry of a flip-through impact. Colour range in cm/s

(b) Pressure distribution on the impact plate. The colors correspond to different pressure gauges that are at the same elevations but for different cross positions. The black line is an average of the pressure data.

Figure 3.12: Experimental low-areated or flip-through impact

two different sections. The flip-through impact maintains similar pressure ranges between different transverse sections of the plate. This is normal because the time for the water to escape is much longer than for air. Much higher peak pressure values are recorded and seem to be more localised along the Z direction. This will be further developed and analysed in the following sections.

3.3 Numerical configuration

This section describes the numerical setup used to model the experimental wave breaking impacts presented in the last Sec. 3.2. The geometry is maintained as in the experiments. A static wave generator mimicking a piston type wave maker is employed following the Boussinesq theory. The selection of a flap or a piston type wave makers causes minor differences on the wave propagation and a slight calibration is needed to reproduce the experimental liquid interface instants before the impact. The right and the bottom boundary conditions are set as solid walls with a no-slip condition for velocity. The top side is modelled by an open boundary with a total pressure condition where air and water can freely flow out and only air can flow in. Finally, the lateral sides are set to indicate a two-dimensional problem.

The mesh has two major zones in the vertical direction: above and below the red line in Fig.3.13. The upper part has a geometric gradation having bigger cells close to the top boundary (upper right Fig. 3.14) and, the lower region mostly filled with liquid, the cell height is fixed in order to accurately capture the interface. Regarding the horizontal direction, a successive refinement by a factor of 0.5 defines 4 regions, see Fig.3.13, where the coarser is close to the inlet and the finest keeping a cell aspect ratio of 1 on the impact

area. Over the slope the cells are parallel to the plane (bottom left Fig. 3.14) except on the impact region where they will keep a 90° angle with the vertical plate. Here, triangular cells are thus needed to fit the mesh with the sloped plane (bottom right Fig. 3.14). These bottom boundary cells will reduce the resolution of the run-up wave kinematics but allow orthogonal cells in the overturning region and close to the impact boundary, which have shown to produce less erratic impact results in terms of pressure on the impact wall cell faces.

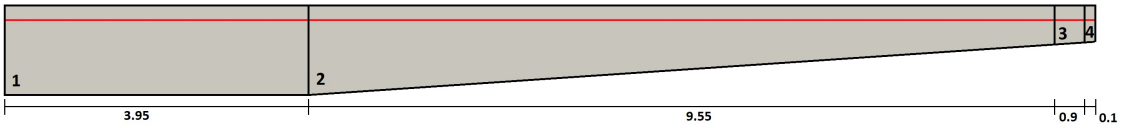

Figure 3.13: Mesh sketch

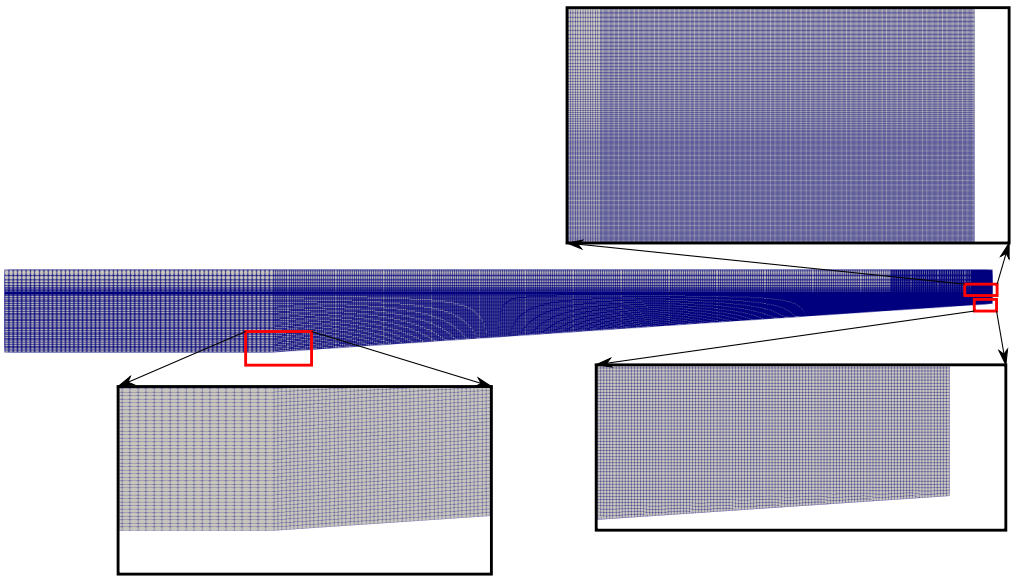

Figure 3.14: Mesh details. Notice the background mesh is only representative and the mesh employed have a higher discretisation.

The finest mesh employed in this 2D configuration had 4.6 million cells and a cell length at the impact region of $\Delta x = \Delta z = 0.5$ mm. A simulation of 9 s is performed, as in the laboratory experiments with a `maxCo` $= 0.5$. It takes 23 h with 28 cores of an Intel Broadwell (2.4 GHz) in CRIANN (Centre Régional Informatique et d'Applications Numériques de Normandie). This calculation time is disproportionately divided between approximately 5 h to compute the first 8 s as the wave propagates and 18h for the overturning and impact. The instants before the impact produce high-speed air flows that drop the time steps drastically down to values of $\Delta t \approx 10^{-5}$ s, especially when using a 2D configuration, increasing then the computational time, see Fig. 3.15.

For these simulations, a kinematic viscosity of 1×10^{-6} m^2/s was used for water and 1.48×10^{-5} m^2/s for air. The density was kept as 1.2 kg/m^3 for air and 1000 kg/m^3 for water. Although the problem faced here is an inertial driven flow, the surface tension was kept with a constant value of 0.07. Following the work of Sumer *et al.* 2010 [113], the Reynolds number for a solitary wave over a slopped beach (applicable in the up-rush

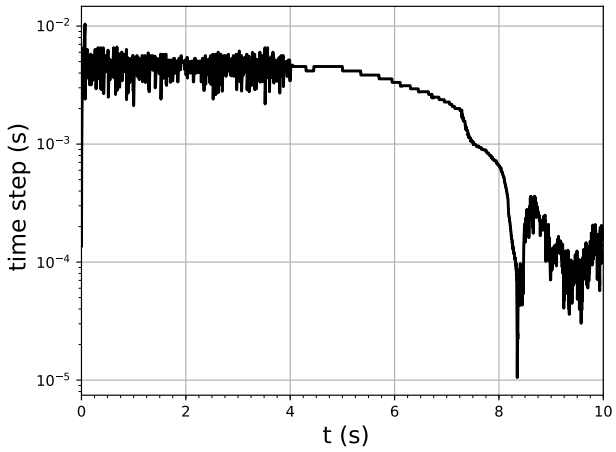

Figure 3.15: Time step evolution during a generation, propagation and an air-pocket impact of a solitary wave in a 2D compressible simulation

phase) can be defined as: $Re_u = A(U_{0m})/\nu$, where ν is the kinematic viscosity, A is half of the stroke of the water particle displacement in the free-stream region and U_{0m} is the maximum free-stream velocity. For the present study, the maximum wave amplitude is $a = 0.0864$ m and the water depth out from the slope $h = 0.7185$ m, thus the maximum Reynolds number at the slope during the run-up phase is $Re_u = 103000$ which is within the laminar flow ($Re_u < 2 \times 10^5$) defined by [113]. It is also presented in the work of [114], on the supplementary materials, how the SST $k - \omega$ does not have a great impact on the dynamics and kinematics before the impact compared to the laminar model. Thus, a laminar model has been adopted in this work for the sake of simplicity. The boundary layer is roughly approximated using the Blasius boundary layer solution [115]. For the two wave conditions employed in this work, it takes values around 2.3 mm on the horizontal bottom region and decreases throughout the swash zone. This boundary layer is out of the scope of the present work and even the finest mesh is not enough to resolve it properly. This is expected to contribute to the discrepancies against the experiments.

3.4 Solitary wave impact onto a vertical wall - 2D incompressible formulation

In this section, the incompressible assumption is tested using the two-phase solver `interFoam` for impulsive impact cases. The air-pocket or high-aerated wave impact is initially tested using a 2D configuration.

3.4.1 Air-pocket or high-areated impact

This section focuses on the wave breaking air-pocket impact under the incompressible assumption for both phases in a two dimensions configuration. Two major numerical challenges are faced in this kind of impact: on the one hand, the complex geometry of a narrow jet of liquid with high curvatures of the interface, and, on the other hand, the existence of high-pressure peaks within small-time intervals.

To begin with, a qualitative study of the impact process is presented in Fig. 3.16 with three snapshots of the dynamics and kinematics of the phenomenon. The reference image time is shifted so that the highest pressure peak is reached at $t = 0$ s. The first image shows

the fields before the impact at the pressure rise time. The second one is at the impact instant and the third during the splash phenomenon. The pressure fields are presented for both air and water using the same scale, although, the pressure range is different for each instant to be representative. On the contrary, the velocity fields have different scales for both phases and keep the same range for the three instants. The free surface is presented as a solid black line referenced by the contour of the liquid volume fraction field $\alpha = 0.5$.

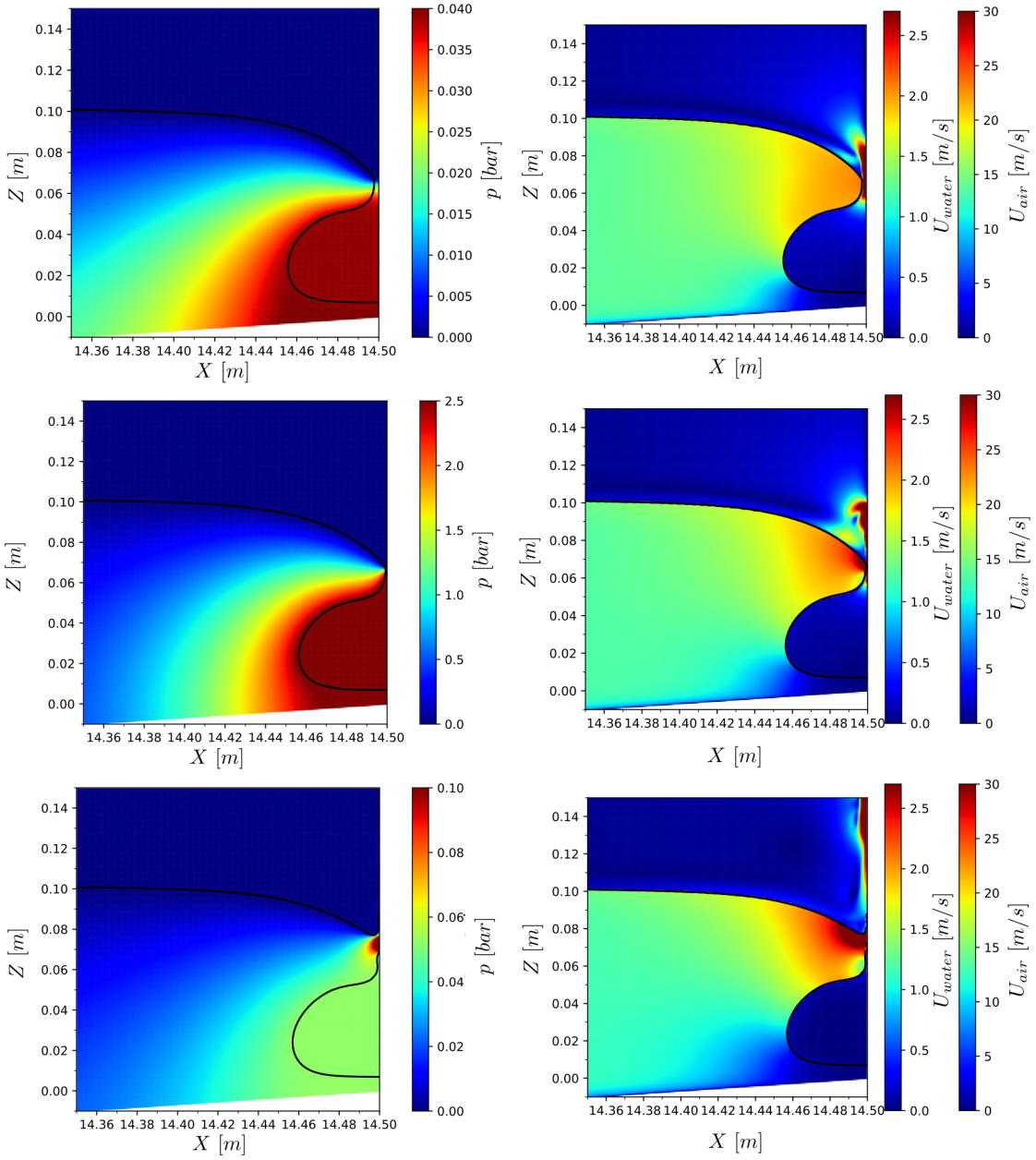

(a) Pressure evolution during the impact with a different pressure range at the each instants.

(b) Velocity magnitude for air and water.

Figure 3.16: Two phase air-pocket impact under the incompressibility assumption using $\Delta z = 0.5$ mm. Solid line corresponds to the interface. Top: before the impact $t = -0.00066$ s. Middle: impact instant $t = 0$ s. Bottom: splash after the impact $t = 0.002$ s.

First from Fig. 3.16, one can observe how the incoming wave momentum is being absorbed by the air entrapped inside the cavity before the collision occurs. Here, the confinement process exacerbates the pressure gradient in front of the water spike increasing the air velocity that flows out from the cavity. This fast air flow drags upwards a fraction of water, leading to a transformation of the water spike into a narrow vertical jet front. Comparing the water region before the impact with the PIV experimental images, presented in Fig. 3.11a, acceptable similarities in terms of velocity magnitudes are presented. At the impact moment, middle Fig. 3.16, the whole cavity has a constant pressure value due to the incompressible assumption and the most pronounced pressure gradient is shown. This fact is not observed in any representative experiments (see [45] or [46]) where the air cavity region exerts a lower pressure magnitude on the wall than the impinging jet area. The highest peak pressure is reached as well as a fast deceleration of the water jet. At this point, the air can no longer escape freely from the cavity and pushes upwards the water front to expand the cavity volume. This is observed in the bottom Fig. 3.16 where the highest pressure records are located on the splash jet directed upwards. As the cavity volume increases, the inner pressure falls.

Now a mesh sensitivity analysis is presented regarding the capability of the solver and the interface method to model such a phenomenon. Four meshes with a factor of 0.5 refinements are studied and presented in terms of free surface profile before the impact, pressure distribution on the wall at the impact moment and maximum pressure series on the wall. All the refinements have demonstrated in Sec. 3.1.3 to be sufficient for generating and propagating a solitary wave, where the coarser mesh presents a ratio of $a/\Delta z = 43$ and the finest $a/\Delta z = 173$.

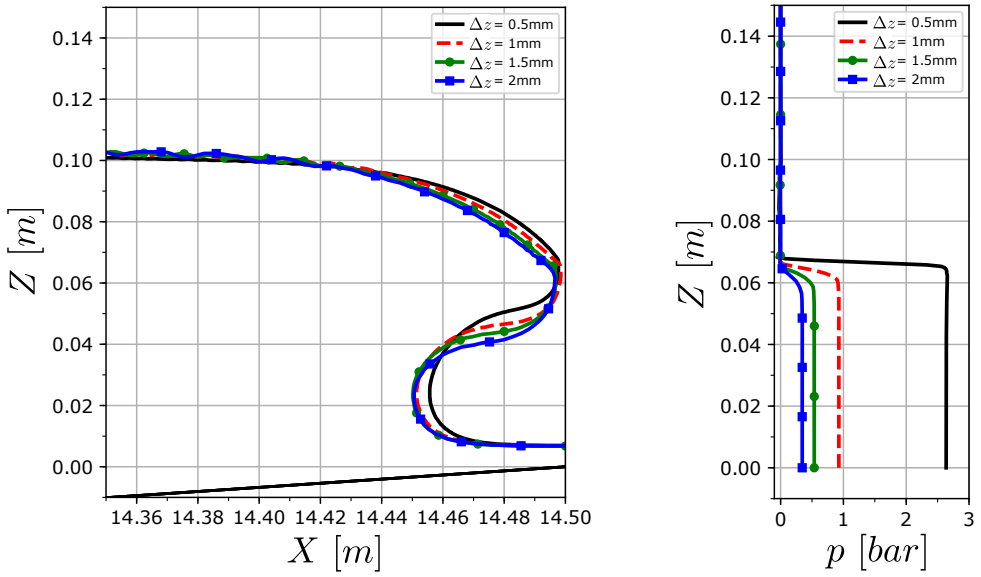

(a) Free surface

(b) Pressure distribution on the wall

Figure 3.17: Mesh convergence analysis. Δz refers to the impact region cell height

First, Fig.3.17a represents the free surface instants before the impact. The grid convergence is partially achieved regarding the free surface as it is part of the whole process of generation, propagation, shoaling and overturning. During this process, a poorly resolved boundary layer and the interface energy dissipation leads to slightly different wave shapes. The free surface is extracted at different instants for each mesh to be comparable, as the

celerity will also vary slightly.

Next, the wall pressure records are studied in Fig.3.17b and Fig.3.18 further detailed in Table 3.1. The pressure distribution on the wall at the impact moment confirms the fact that the whole cavity keep a constant pressure at the impact moment, as shown in middle Fig.3.16.

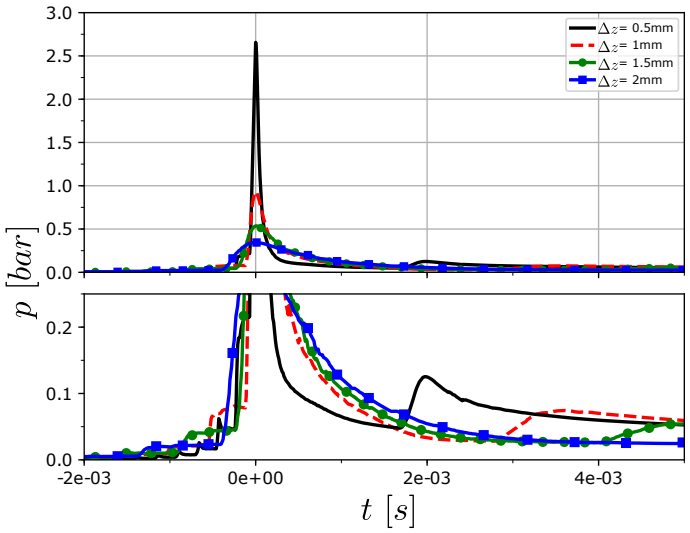

Figure 3.18: Mesh convergence analysis: maximum pressure serie on the wall. Δz refers to the impact region cell height

The selected series in Fig.3.18 belong to the cell face on the wall where the maximum peak pressure is reached within the impact area. The series are shifted in time so that the impact moment occurs at $t = 0$ s and each serie corresponds to different elevations of the wall depending on the mesh configuration impact point. These pressure series present abrupt rises of pressure of the order of $0.02 - 0.1$ bar less than 1 ms before the main peak pressure arrives. Then, the impact event is presented as the main peak pressure with high slopes at the rise time and lower during the fall. After the jet impact, a pressure valley is presented just before the collapse of the cavity which will lead to the splash phenomenon as the second pressure rebound. This second pressure rise is due to a strong jet of air trying to escape from the cavity through the front part of the overturning wave and pushing upwards with high velocity the liquid phase (see Fig.3.16). Depending on the violence of this jet, a smooth rebound $\Delta z = 2$ mm is observable which turns out to be steeper as the mesh is being refined to $\Delta z = 0.5$ mm. With respect to the maximum pressure value, once again the peak pressure keeps increasing when the cell size is being reduced. On the other hand, the rise time decreases while refining the mesh. These behaviours are similar to what was observed in Sec. 2.2.1.

$\Delta x = \Delta z$ $[mm]$	2	1.5	1	0.5
$pMax$ $[bar]$	0.344	0.537	0.93	2.656
Δt $[s]$	4×10^4	2.3×10^4	1.2×10^4	7×10^5
I $[N \cdot s/m^2]$	35.18	35.72	35.97	36.2

Table 3.1: Pressure and impulse impact study for different spatial discretisations

In this realistic wave impact, the definition of the impulse is calculated as an integral under the pressure serie (see the impulse definition Sec. 2.1). Now, the time before the

impact t_b is the instant where the pressure slope will remain approximately constant until the peak pressure. Consequently, this defines the rise time expressed in Table 3.1 as Δt. The time after the impact t_a is defined here as the same point for all different meshes as $t = 0.0014\,s$ where the function slope is approximately 45° with the horizontal. After these definitions, the obtained results are presented in Table 3.1 where a good convergence on the pressure impulse is achieved, similarly to what was obtained on the idealised wave configuration. With such results, it turns out that the incompressible assumption in a 2D configuration may lead to erroneous pressure peaks when studying such impulsive events.

3.5 Solitary wave impact onto a vertical wall - 2D compressible formulation

Following the impossibility to obtain converged peak pressure values under the incompressible assumption, a new approach using a compressible solver `compressibleInterFoam` is evaluated in this section. Two realistic breaking waves are modelled and analysed focusing on the compressibility role with a 2D configuration wave channel. A mesh sensitivity analysis is regarded for the air-pocket impact, followed by a comparison with the experimental data in terms of pressure records on the wall for both high and low aerated impacts.

3.5.1 Air-pocket or high-areated impact

This section focuses on the air-pocket impact under the compressibility assumption for both phases, following the ideal gas and the Tait's equation of state (see Sec. 1.2.4) in a two dimensions configuration.

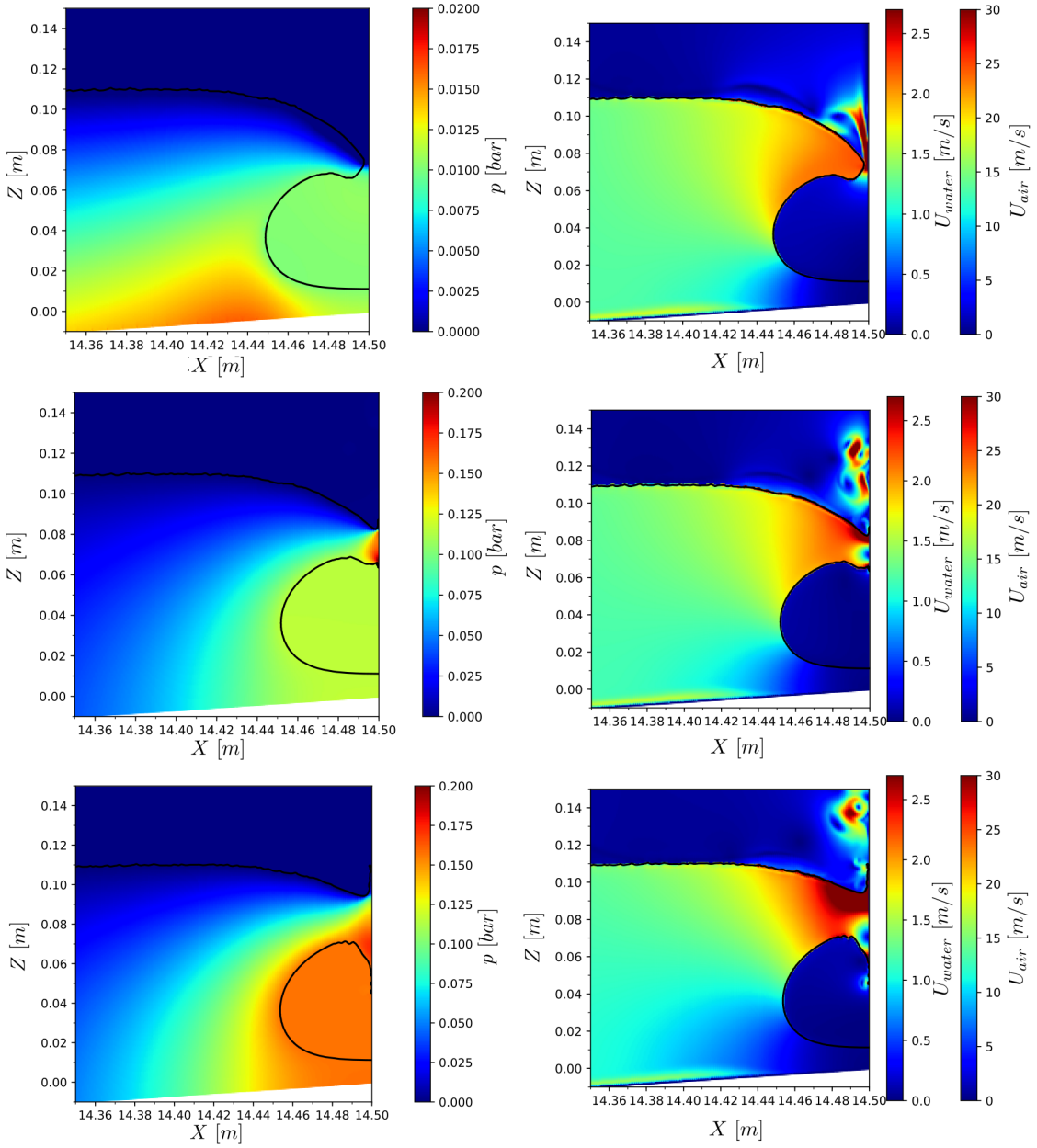

(a) Pressure evolution during the impact with a different pressure range at the each instants.

(b) Velocity magnitude for air and water.

Figure 3.19: Two phase air-pocket impact under the compressibility assumption using $\Delta z = 0.5$ mm. Solid line corresponds to the interface. Top: before the impact $t = -0.00243$ s. Middle: impact instant $t = 0$ s. Bottom: splash after the impact $t = 0.00257$ s.

To begin with, a qualitative study of the impact process is presented in Fig.3.19. The reference time is shifted so that the highest pressure is reached at $t = 0$ s. The upper Fig.3.19 represents an instant before the impact. Here the air cavity is being rapidly enclosed and the pressure starts increasing. The air is forced to leave the cavity through the space between the wall and the water spike front. The air outflow speed increases as the water spike approaches the wall and it will stop as soon as the water meets the wall. Once this happens, the deceleration of the water spike is balanced by a fast pressure rise to stop the moving liquid. There is only one stagnation point where the velocity is equal to zero, on each side of this point the liquid escapes up and down. In middle Fig.3.19 the highest peak pressure is located in the water impact area and the cavity, still pressurised, will reach lower values. This differs from what was presented under the incompressible assumption, see middle image in Fig.3.16, where both the air and the water region had the same pressure value at the impact moment. Finally, the splash phenomenon occurs when two water jets go upwards and downwards from the impact area avoiding the obstacle, bottom image Fig.3.19. This last phenomenon are characterised by dynamic pressures in the order of $p = \rho u^2$.

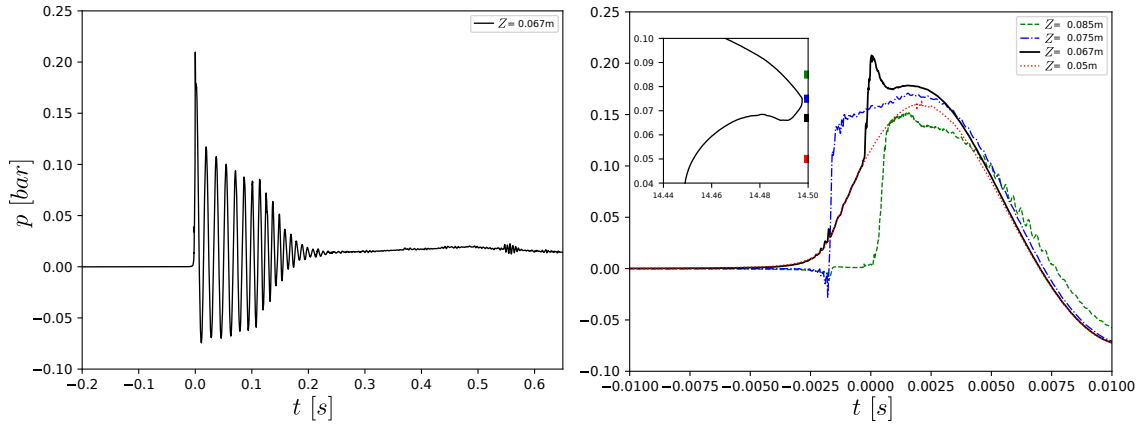

(a) Maximum pressure serie

(b) Different elevation pressure series

Figure 3.20: Pressure records during a 2D air-pocket or high aerated impact

Further understanding of this process can be extracted from the pressure fields recorded in every time step on the wall cell centres. Fig.3.20a presents a typical pressure record on the water impact area undergoing a 2D high aerated impact ($z = 0.067$ m). In this region, the fast deceleration and the higher density will lead to the highest pressure values in these kinds of events. Three main phenomenons are presented here; first the peak pressure related to the high density phase impact ($0 < t < 0.01$ s). Secondly, and until $t < 0.2$ s, a process of pressure oscillations due to an anisotropic contraction and expansion behaviour of the air cavity; this behaviour has already been reported experimentally in [39], [38] or [45]. This process ($t > 0.2$ s) could be related to a spring effect of the compressibility of the gas pocket, similarly to what was presented in Sec. 2.3. The shape and area of the cavity will have a great effect on the magnitude and damping of these oscillations. Moreover, this air cushioning effect evokes the necessity of a two-phase solver and has been studied before from a different perspective using Lagrangian methods, e.g. [81]. Finally, a tended rebound of quasi-hydrostatic pressure is presented during the run-up phase. This has not been completely computed as it is out of the impulsive scope of this work and involves a turbulent behaviour.

Now four numerical pressure sensors near the impact point are analysed in Fig.3.20b.

The black continuous line is a zoom of the impact instants ($-0.01 < t < 0.01$ s) already presented in Fig.3.20a. The red sensor located inside the air cavity is the first to be pressurised with a gradual growth as the air cavity is being enclosed. It will have a cushioning effect reducing the whole event violence. The black sensor simultaneously climbs on pressure until a sudden jump presents the highest peak pressure. This happens when the water spike meets the wall. The peak pressure is located on the water spike impact area. However, it will move relatively between the red and the blue sensors depending on the water spike shape and disposition. After the impact, the pressure drops and rebounds as the air cavity is being gradually pressurised due to the incoming wave. Before impact ($-0.0025 < t < -0.001$ s), the atmospheric pressure remains constant on the blue sensor $Z = 0.073$ m until a subatmospheric pressure happens just before the water meets the wall. This subatmospheric pressure has also been reported experimentally by [38] or [116] and is produced by the high-speed air flowing out before the entrapment. Next, the steepest pressure rise occurs when the liquid first meets the wall and keeps increasing levelling the air cavity pressurisation. To end with, a sensor (green dashed line) above the impact area is also affected by the air jet depressurisation. It will not increase in pressure until the splash phenomenon starts and then it will further be pressurised by the cavity compression.

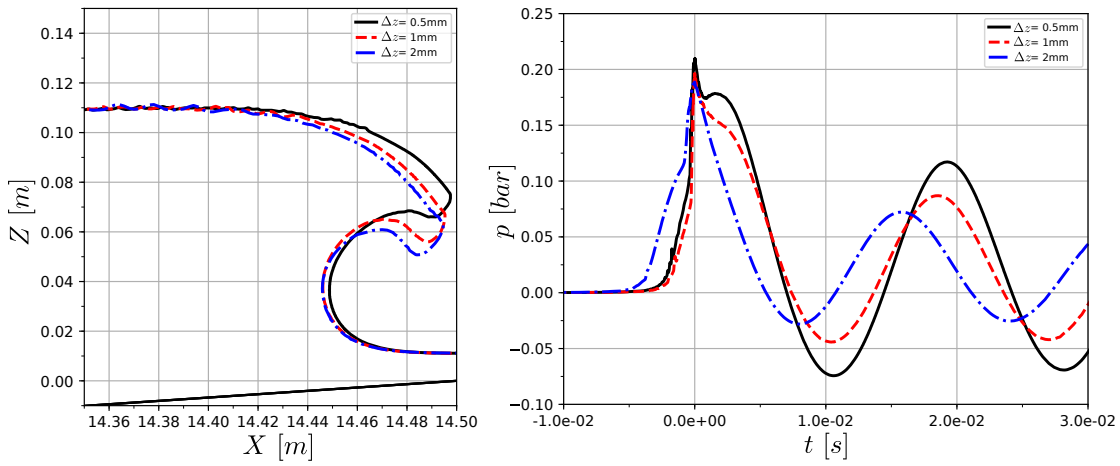

(a) Free surface

(b) Maximum pressure serie on the wall

Figure 3.21: Mesh convergence analysis. Δz refers to the characteristic cell length in the impact region denominated as 4 in Fig. 3.13.

Now a mesh sensitivity analysis is carried out, in terms of free surface and pressure fields, with a spatial refinement factor of 0.5. These meshes are referenced by the characteristic cell length $\Delta x = \Delta z$ in the impact area (region 4 of Fig. 3.13). Fig.3.21a compares the free surface profile before the impact. A partial convergence is achieved due to the interface diffusion and a poorly boundary layer resolution during the wave: propagation, shoaling and overturning. Therefore, the pressure record with the highest peak pressure, being highly sensitive to the water spike, is located at different elevations and instants. Fig.3.21b presents this highest pressure signal recorded on the wall at $Z = 0.052\,m$ for the coarser mesh (blue dashed-dotted) and $Z = 0.067$ m for the finest (black line). This last configuration corresponds to the one presented on Fig.3.20. The signals were shifted so that the highest pressure is reached at $t = 0$ s. The most relevant feature is the stability of the peak pressure around 0.2 bar while refining the cell size, hence slightly modifying the water spike geometry. Besides this fact, the pressure rise before the impact has some

differences between the finest and the coarser mesh. This may originate from the faster arrival of the peak pressure. To further develop this, as it was mentioned in Fig.3.20b, the peak pressure may not occur at the very first liquid-solid contact but will depend on the incident angle and front shape of the water spike. The pressure rise due to compression of the air cavity, with a lower slope than the fluid impact, has two major differences between discretisations: on the one hand, a lower maximum value of the first compression related to smaller volume of air being entrapped by the coarser mesh $\Delta z = 2$ mm; and on the other hand, a sooner appearance of this compression linked to the fact that the presented pressure record is closer to the air cavity with the coarser mesh.

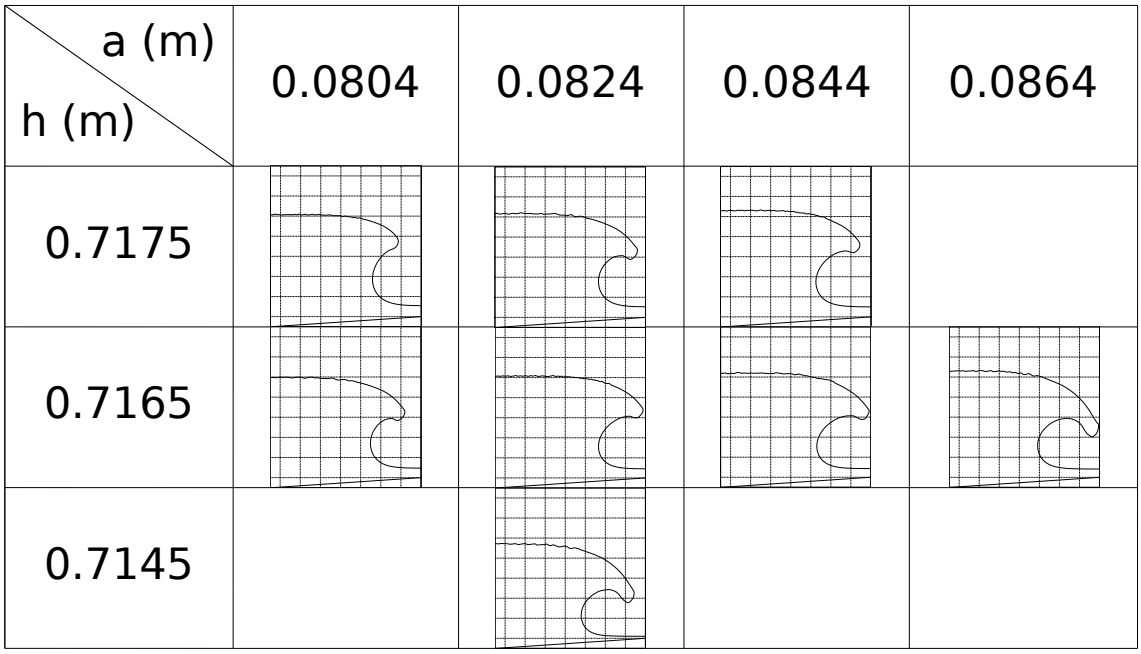

Figure 3.22: Parametrization study regarding the water depth and wave amplitude

The convergence of the results towards a stable solution while improving the mesh resolution gives confidence to now compare the numeric results with the experimental data. The finest mesh $\Delta z = 0.5$ mm is employed in the forthcoming comparisons. To achieve the better experimental-numerical comparison, it is necessary to reproduce the kinematics and fluid geometry moments before the impact. The chosen experimental wave parameters for this case were a soliton amplitude of 0.0864 m and a water depth of 0.7185 m. However, as mentioned before, the wave maker during the experiments was a flap and here a piston type is employed. This will arise slight differences during the propagation and, thus, a parametrization study regarding the water depth and amplitude was carried out to obtain the most comparable profile before impact, see Fig. 3.22. It is observable how, by increasing the water depth and maintaining the wave amplitude, the breaking points moves away from the impact plate. Or, by maintaining the same water depth and increasing the wave amplitude this will occur similarly. The numerical amplitude employed in this case is $0.0844\,m$ and a water depth of 0.7165 m, which produces the interface profile shown in Fig.3.23a.

Differences can be seen in terms of surface elevation in the order of mm and lower depth regarding the quasi static-fluid under the air cavity. The air cavity has a smaller area when compared with the experiments and the numerical water spike is narrower. Furthermore, very low amplitude oscillations are observable at the top part of the wave due to some

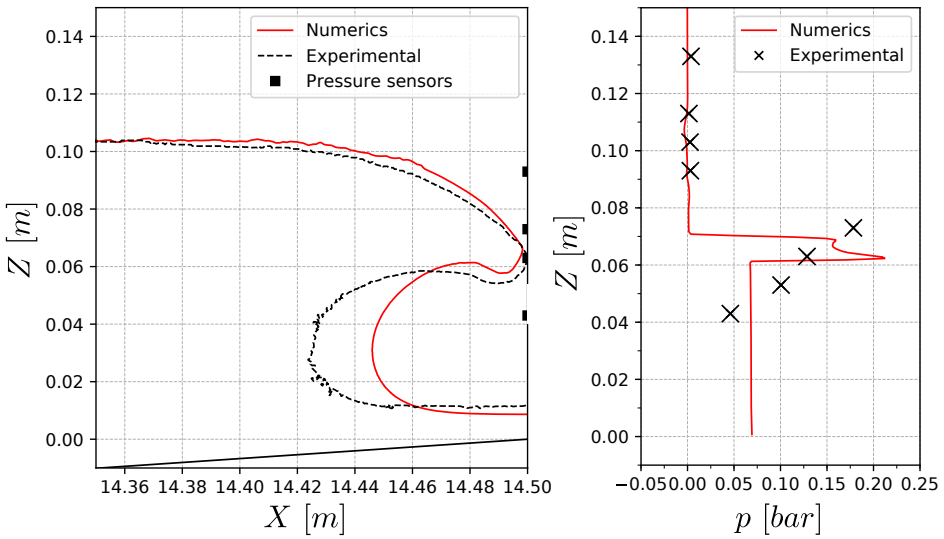

(a) Free surface

(b) Pressure distribution on the wall at $t = 0$ s

Figure 3.23: Free surface and pressure distribution comparison at the impact moment.

parasitic currents on the low density phase near the interface. This phenomenon has been already and largely reported in the literature, linked to the surface tension term on an initial stage (see [67, 69, 117]) and extended to inertial flows due to an imbalance on the pressure and the density gradient terms near the interface (see [68,75]). Here these wiggles remain small enough not to affect the inertial driven flow during the next few seconds. Although these discrepancies with the experiments, a fairly good agreement is achieved and allows a fair comparison in terms of loads on the wall.

Fig.3.23b compares pressure distributions at the instant when the maximum pressure peak is reached numerically and the averaged maximum pressure distribution from the experiments, as it was presented in Fig.3.11. The low relative amount of pressure sensors during the experiments and the variability between the different transverse sections enables only an approximate comparison. But both numerically and experimentally, the peak pressure is reached in the vicinity of the water impact region. However, the numerical distribution reaches the highest peak pressure slightly beneath the initial contact point. Regarding the experiments the maximal pressure is reached above the initial impact point. Inside the air cavity, at $Z = 0.053$ m, the average pressure records extracted from the different sensors (at different transverse location) have very different values $\Delta p = 0.14$ bar and the presented averaged value may not be completely representative. On the contrary, the sensor at $Z = 0.043$ m has a more reliable value in the experiments and presents an overestimation of the numerical results. This fact is expected from the 2D configuration which does not allow the air from the cavity to flow out using the backlash in the transverse OY direction. Above the impact area, the pressure values remain as atmospheric pressure both numerically and experimentally speaking.

Fig.3.24 depicts a closer comparison to four temporal pressure series with the experiments. As mentioned above, the temporal series are shifted so that the highest peak pressure is reached at $t = 0$ s experimentally and numerically. Slight time lag is observed due to the different geometries between the numerical and the experimental results. The behaviour inside the air cavity ($Z = 0.043$ m) experiences a rise of pressure at the first instant. Experimental and numerical records are initiated following a similar trend, even

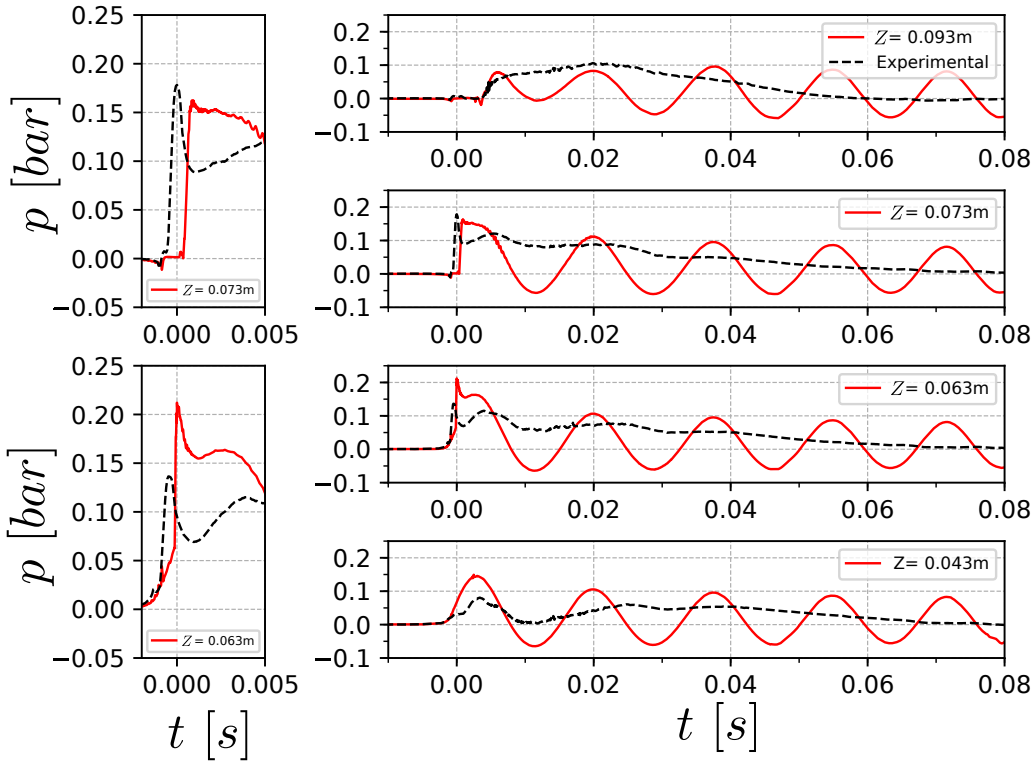

Figure 3.24: Pressure series for 4 different elevations on the plate in a compressible air-pocket impact

though their evolution rapidly separate from each other. Sinusoidal like oscillations are produced numerically by compression and expansion of the air entrapped with an approximate initial frequency of 80 Hz. The simulation reaches a higher value of 0.14 bar during this first compression of the cavity and a subatmospheric minimum of 0.058 bar in the first expansion. This pressure oscillation phenomenon is not appreciable on the experiments after the first rebound. Here the compression of the cavity, with a lower pressure range of 0.08 bar, pushes the air to flow in the transverse direction reducing the pressurisation to normal atmospheric values. This is followed by a pressure plateau of 0.06 bar produced by a water jet going downward from the impact point. The expansion and contraction of the air cavity are completely damped after 0.3 s. This phenomenon will affect all the pressure signals within the influenced area during this interval.

A focus will now be made on the region where the water spike meets the wall: between $Z = 0.063$ m and $Z = 0.073$ m. A detail of the impact interval is shown on the left part of Fig.3.24. At $Z = 0.063$ m, the highest numerical peak pressure of 0.21 bar is reached. The presented rise in pressure has two main origins: an initial rise produced by the air-cavity compression and a second, with higher values, by the water impact. Approximately 1 ms after the peak, the pressure drops and is followed by a second rebound when the air cavity if fully compressed (see bottom left graph of Fig.3.24). Similarly, the experimental record presents a lower maximum pressure peak at 0.14 bar then followed by the air-cavity compression lead pressure rise. Next it follows a similar trend as the simulation, with a pressure fall and a second rebound simultaneously with the air cavity maximum compression. The peak pressure then seems to be a superposition of water spike momentum and the cavity pressurisation effects. Finally, the numerical results will not capture the experimental behaviour, where the possibility for the air to flow out will

prevent the subatmospheric oscillations. At $Z = 0.073$ m, the highest experimental peak pressure of 0.17 bar is reached (see top left graph of Fig.3.24). Here the high slope on the pressure rise is originated initially only by the water impact. Numerically the peak pressure is underestimated due to a lower water impact region.

The pressure sensor above the water impact ($Z = 0.093$ m) represents the splash phenomenon and the run-up. Here both numeric and experiment experience at the same time a pressure rise when the splash phenomenon occurs. Small subatmospheric pressure drops are captured experimentally and numerically at different instants before this pressure rise. The air-cavity compression and expansion will also affect this higher part of the wall arising a clear physical phenomenon differentiation between the experiments and the simulation.

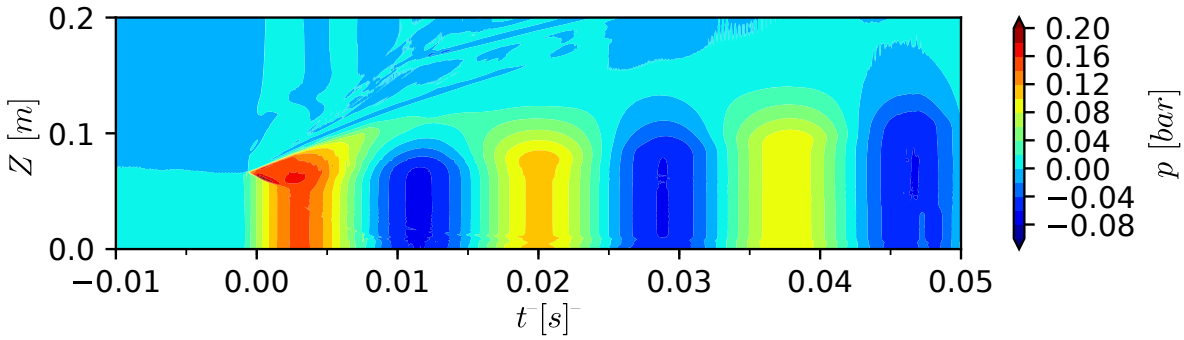

Figure 3.25: Spatio-temporal representation of the wall pressure in the compressible air-pocket impact.

Finally, a coloured map of the evolution of pressure field on the wall is presented in Fig.3.25. The cavity compression before the water jet meets the wall is presented in lighter blue below $Z < 0.065$ m. Less than 1 ms before the maximum peak pressure, the water meets the wall and a sudden pressure rise is observed at the impact area, coloured like the orange arrowhead. After that, the peak pressure in dark red is located beneath this point having a downward direction as the water jet influence starts expanding. At $t = 3$ ms the cavity reaches the maximal compression and starts the expansion process. From this map, the air-cavity compression-expansion oscillating phenomenon can clearly be observed.

3.5.2 Flip-through or low-areated impact

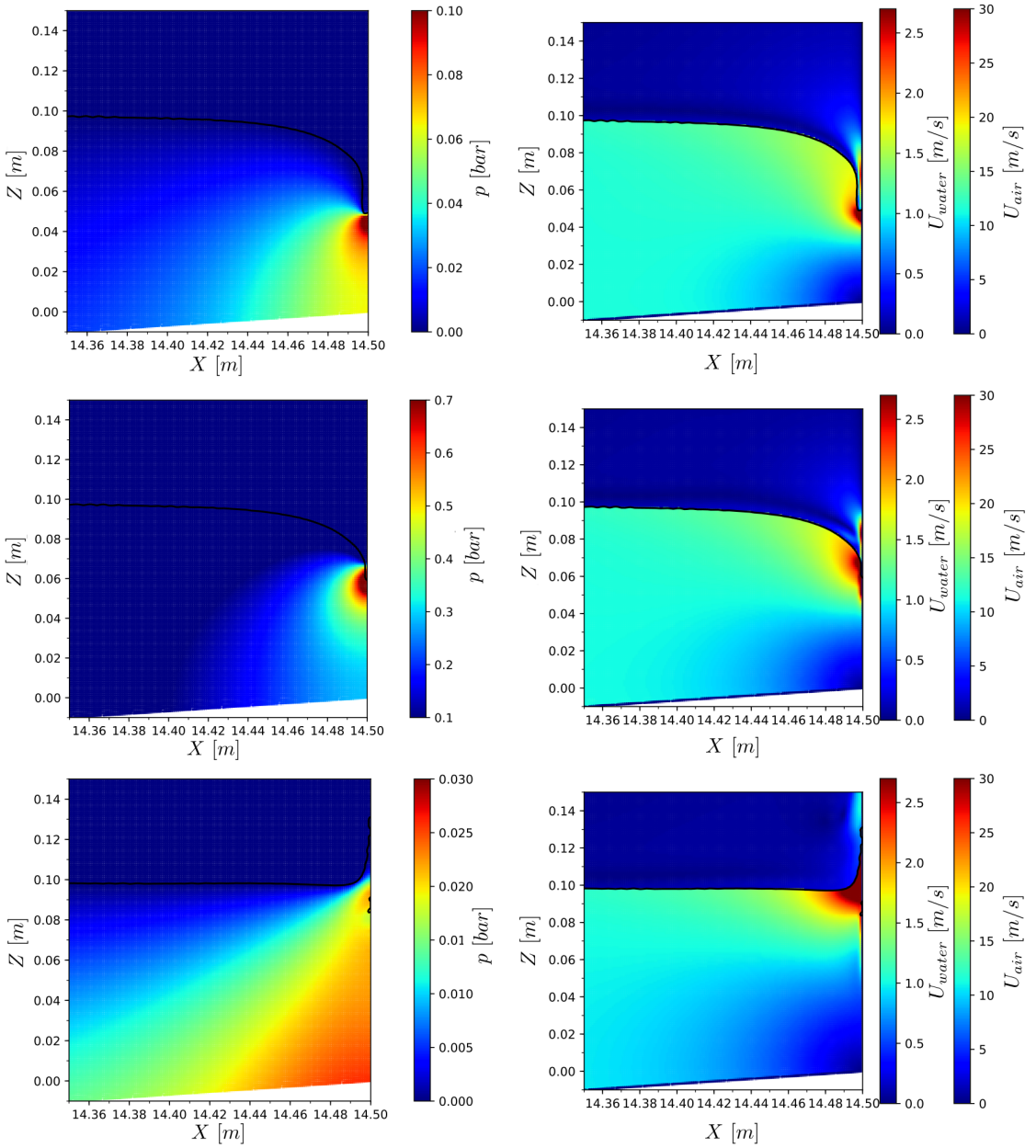

(a) Pressure evolution during the impact with a different pressure range at the each instants.

(b) Velocity magnitude for air and water.

Figure 3.26: Two phase flip-through impact under the compressibility assumption using $\Delta z = 0.5$ mm. Solid line corresponds to the interface. Top: before the impact $t = -0.001$ s. Middle: impact instant $t = 0$ s. Bottom: splash after the impact $t = 0.008$ s.

Now the flip-through or low-areated impact is evaluated. This kind of wave breaking impact only occurs in limited configurations, where the amount of air encapsulated between the liquid and the wall is small. It produces higher peak pressures than the air-pocket as well as more violent upwards water jets. Following the same procedure as in the air-pocket impact, a first qualitative analysis is carried out regarding three snapshots during the impact interval (see Fig. 3.26). The selected instants are: before the impact, the instant where the highest pressure peak is reached and the initialisation of the splash. The complete impact phenomenon occurs over a relative short time interval of 9 ms. From the upper image in Fig.3.26 for instants before the impact happens, only the lower part of the wave is in contact with the wall. It is already exerting a momentum pushing the fluid upwards to avoid the obstacle, similarly as what has been referred as the slightly breaking case in [45]. Above this point, a relatively large water front is nearly parallel to the wall. The air is flowing out fast from the small cavity. In this computation, the upward velocity will not be fast enough to liberate all the air before the incoming wave front meets the wall resulting in a very small fraction of air entrapment (see middle Fig.3.26). At this moment the superposition of the fast deceleration of the wave front and the upward jet avoiding the obstacle lead to a highly localised pressure. Similarly as in the air-pocket situation, a compression and expansion process happens now with much higher frequencies due to the smaller size of air cavity. Finally, all the momentum is transferred upwards creating a violent vertical water jet.

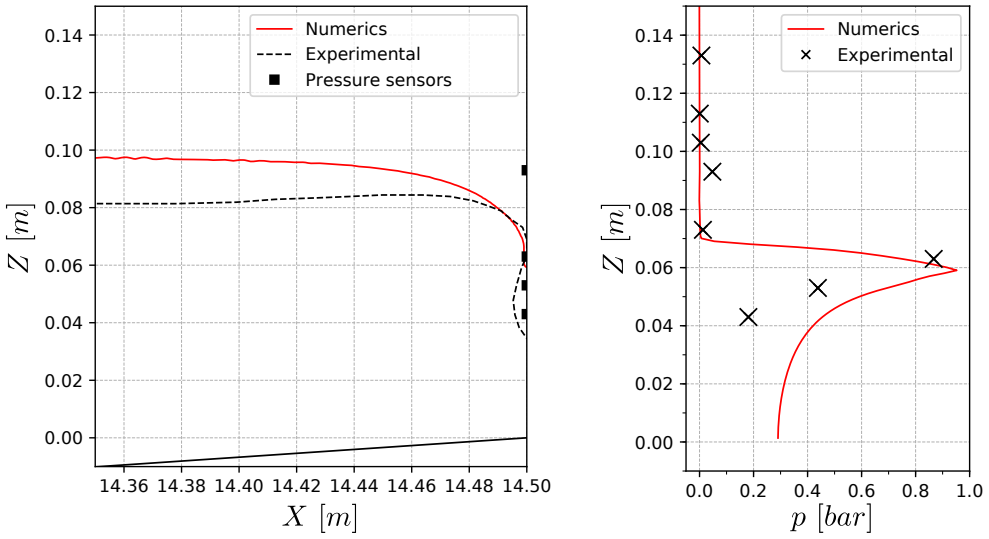

(a) Free surface

(b) Pressure distribution on the wall at $t = 0\,s$

Figure 3.27: Free surface comparison at the impact moment. Numeric values of $\alpha = 0.5$.

This wave breaking impact type is regarded as the limit between the slightly breaking phenomenon and the air-pocket impact, it is then highly sensitive to the wave parameters. Figure 3.27 depicts numerical-experimental comparisons, first in terms of free-surface profile before impact and second in terms of pressure distribution at different locations on the plate. The experimental parameters employed were: a wave amplitude of 0.0627 m and a water depth of 0.7185 m for the water depth before the sloped beach. Here, the numerical solitary wave generation inputs are a wave amplitude of 0.076 m and a water depth of 0.7185 m to achieve the profile presented in Fig.3.27a. A similar impact point elevation is achieved in both cases. However, two major differences are presented in terms

of higher air entrapment during the experiments and a lower experimental wave height, both of which could be attributed to the different wave maker types. In Fig.3.27b, the pressure distribution is presented at the maximum pressure instant. The pressurised area starts both in experiments and numerics at $Z = 0.07$ m with a steep gradient towards the maximal pressure. The experimental pressure sensor at 0.063 m recorded the peak pressure in two transverse sections (see Fig. 3.12b of Sect. 3.2). This situation is also reproduced on the simulation where a similar magnitude of this peak is reproduced and at a slightly lower elevation of $Z = 0.06$ m. Next, the pressure gradient has higher values in the experiments regarding the sensors inside the air cavity. This is attributed to the cushioning effect of a higher fraction of air.

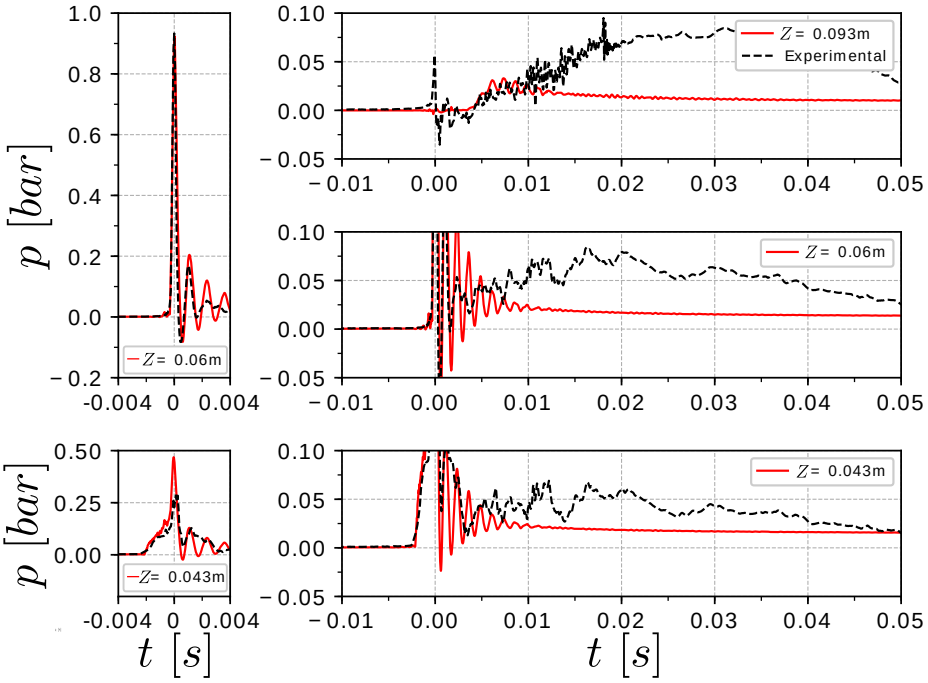

Figure 3.28: Pressure series for 3 different elevations on the plate in a compressible flip-through impact

Three relevant pressure series, referred to as black squares in Fig.3.27a, are studied in Fig.3.28. Let us start from the highest location $Z = 0.093$ m above the impact point. Experimentally, an initial noisy behaviour is attributed to the high speed air flowing out from the cavity producing momentaneous subatmospheric values. These are also captured on the simulation, though, in lower magnitudes of -0.005 bar compared to the experimental minimum of -0.03 bar. After approximately 4 ms, there is an experimental pressure rise which is well captured by the simulation on an initial stage. Numerically, at $t = 0.01$ s the simulation reaches a maximum of 0.03 bar and starts a plateau of 0.01 bar that lasts for 0.3 s. This pressure rise has two main origins: an initial rise produced by the water jet velocities of $1-2$ m/s and a second, by the hydrostatic pressure as the water ascends the wall. After the initial pressure rise, the experiments rebound to higher values of 0.08 bar. The main reason for this discrepancy is due to a thermal shock produced by the difference of temperature between the sensor and the water during wetting process.

Next, the impact point is evaluated at $Z = 0.063$ m during the experiments and at

$Z = 0.06$ m on the simulation. The top left part of Fig.3.28 presents a detail of the impact interval. At the location where the water front strikes the wall, the pressure rockets to 0.9 bar in less than 0.3 ms. This is accurately captured by the numerical simulation. Although, after the impact a sudden pressure drop to a minimum of -0.08 bar is followed by an oscillatory behaviour linked to the compression and expansion of the cavity. Here, the obtained frequency with $f \simeq 1000$ Hz is much higher than with the air pocket configuration due to lower volume of the cavity. These oscillations are accurately captured numerically until the second expansion where the experiments present a faster damping, probably due to 3D effects. After the impact, the simulation presents a stable dynamic pressure as it happens in higher elevations on the plate. On the contrary, in the experiments, a higher value of pressure is recorded most probably coming from the aforementioned thermal shock on the pressure sensor.

The region below the impact point($Z = 0.043$ m) is already wet and receiving pressure gradually by the incoming liquid before the impact occurs. Approximately 2 ms before the water front strikes the wall, the pressure starts rising gradually. This happens as the water changes the velocity direction from being perpendicular to parallel to the wall together with a deceleration. The sensor is located in the water region during the simulation while, presumably, it is inside the air cavity in the experiments. Regarding the pictures extracted from the experiments, an unclear interface is defined in this stage as the cavity is a mixture of air bubbles and water. This explains a lower peak pressure of 0.28 bar in this area attenuated by the air on the experiments while a peak of 0.46 bar is numerically captured with pure liquid. The compression and expansion of the air entrapped are absorbed around the impact point. Here the first expansion reaches numerically a subatmospheric pressure of -0.015 bar while in the experiments falls to a positive value of 0.06 bar. Again the damping is underestimated under the 2D configuration as well as the splash phenomenon which is reaching lower maximal value while getting closer to the channel bottom. However, a fairly good agreement between the experimental and numerical pressure record is presented on these graphs of Fig. 3.28 which gives confidence in the numerical assumptions and the computations run.

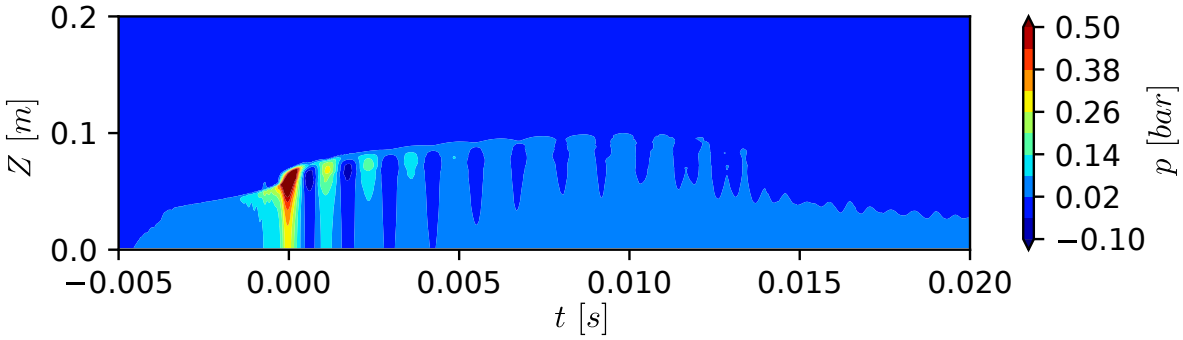

Figure 3.29: Spatio-temporal representation of the wall pressure in the compressible flip-through impact.

Finally, a spatio-temporal representation of the pressure field over the plate is presented on Fig.3.29. Before the impact ($t \leq 0$ s), the lower parts of the plate are being slightly and gradually pressurised as the wave arrives. At the impact moment, a very intense peak pressure is located around the impingement point. And generally speaking, the whole area beneath this point will reach values of ≈ 0.3 bar, that are higher than in the air-pocket configuration. In contrast, these high loads will only last a short period of time. And

then, high frequency compression-expansion oscillations start.

This section has investigated two wave breaking types using a compressible two phase solver in a 2D configuration. First, a global convergence study has demonstrated the possibility to obtain a reliable solution using fine discretisations conversely to what was presented using an incompressible solver. The numeric result obtained during an air-pocket breaking wave situation has been compared with the experiments and presented a good agreement regarding the initial pressure impact and wave shape instants before the impact. On the other hand, the air entrapment compression and expansion behaviour following the impact has shown to be highly dependant on the possibility to escape and, here, the 2D configuration has shown differences regarding the pressure temporal series. Finally, the flip-through breaking situation has been fully validated against the experiments, capturing the pressure impact magnitude and the air oscillations after this pressure peak.

3.6 3D compressible solitary wave impact onto a vertical wall

In this section a three-dimension geometry is employed to model the air-pocket impact. The motivation of this approach is to measure the influence of the lateral air outflow from the cavity. The experimental setup allowed this phenomenon by keeping a backlash between the impact plate and the lateral walls (see Fig. 3.9b or [46]). This is expected to have a direct influence on the pressure oscillations inside the air cavity presented in Sec. 3.5.1. This simulation aims to reproduce the short interval of time when the impact occurs while keeping the refined spatial and temporal discretisations. For this purpose, the general idea is to reproduce only the impact region for the impact duration, and not the whole propagation stage which would have been time consuming in 3D. In other words, the assumption is made that, during the impact process, most of the channel length is not affected by this phenomenon and vice versa.

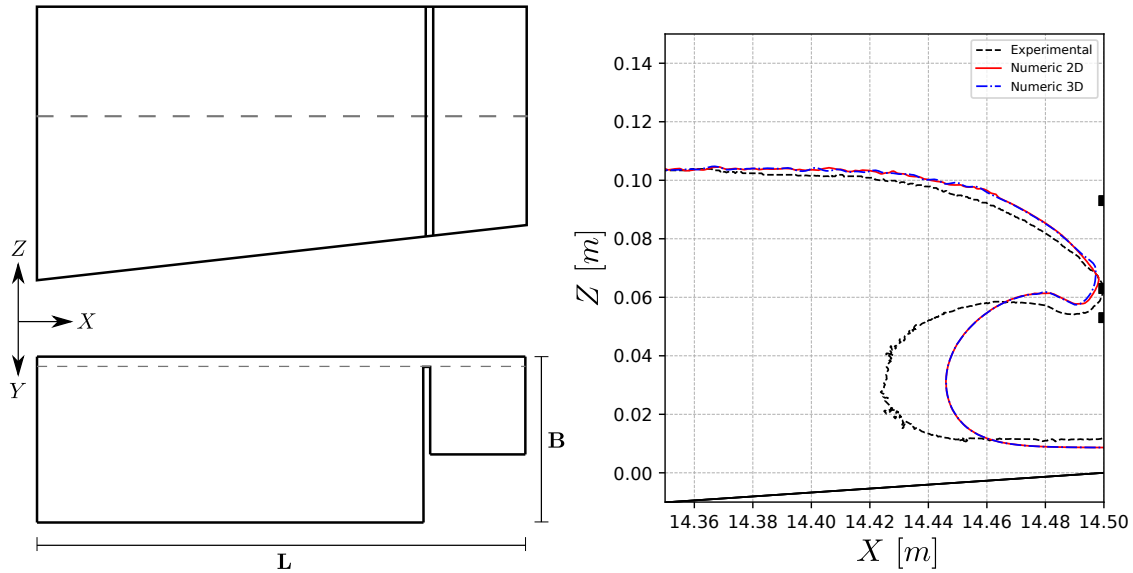

(a) 3D geometry sketch

(b) Free surface before the impact

Figure 3.30: 3D air-pocket impact simulation overview

The presented simulation is an extrusion along the Y direction of the final meters of

the 2D wave channel during the overturning process. To do so, an `OpenFOAM` existing tool called `mapFields` has been used. The cell centre fields from the source mesh are interpolated by proximity to the target mesh cell centre at the indicated time. This time is chosen so that the less time steps have to be computed on the 3D mesh before the impact occurs together with that the incoming wave should not already be affecting the wall in terms of pressure. The employed 3D geometry is presented in Fig.3.30a. The last 30 cm of the 2D channel are extruded along the Y direction. Behind the impact plate, 10 cm are added in the X direction, which are connected to the main channel through a 2 mm width backlash as in the experiments. Regarding the mesh, two differentiated regions in the vertical direction are defined. The lower, beneath the dashed grey line (Fig.3.30a), will keep an aspect ratio of 1 between X and Z (cell length being $\Delta x = \Delta z = 1$ mm). Above this, which will remain out of the water and the interface region until the run-up, a geometrical gradation is employed in the vertical direction. in the Y direction, four equidistant cells of $\Delta y = 0.5$ mm are employed to model the backlash width. A geometrical gradation of the plate region in the Y direction is employed where the central cells are double size, then $\Delta y = 1$ mm, compared to the near-wall cells. Back of the plate, the gradation in the Y direction starts from $\Delta y = 0.5$ mm to 1 mm. With these assumptions, and using a channel width of $B = 0.15$ m, the mesh had 4.9 million cells. The simulation of the 0.2 s impact process using a maximum Courant number of 0.5 approximately takes 41 h with 28 cores of an Intel Broadwell (2.4 GHz) at the CRIANN. Here, the computation is highly constrained by the Courant condition around the backlash when the fast outflow of air from the cavity drastically drops the time-step short before the impact and hence increases the computational time.

The employed boundary conditions are set as solid walls with a no-slip condition for the lateral wall close to the backlash and the bottom. The impact plate and the end of the channel boundary are also defined as solid walls with a no-slip condition. However, aiming to reduce the computational costs of the simulation by only modelling half of the wave channel in the Y direction, a symmetric boundary condition is set to the central plane. The computed part of the channel width is in fact $B_{exp} = 0.32$ m but this will not have a major impact on the obtained results. The top plane is defined as an open boundary with a total pressure condition. Finally, the most critical boundary condition is the inlet plane where a similar inflow velocity as in the 2D configuration section is imposed. Here, a constant value of velocity on the horizontal direction is set on each wet cell. More precisely, a constant velocity of $U = 1.1$ m/s is imposed at the inlet based on an extraction from the 2D configuration section situated 14.2 m away from the wave maker. All the other variables such as the pressure, the liquid volume fraction are extracted from the air-pocket configuration presented in Sec.3.5.1 at $t = 8.33$ s.

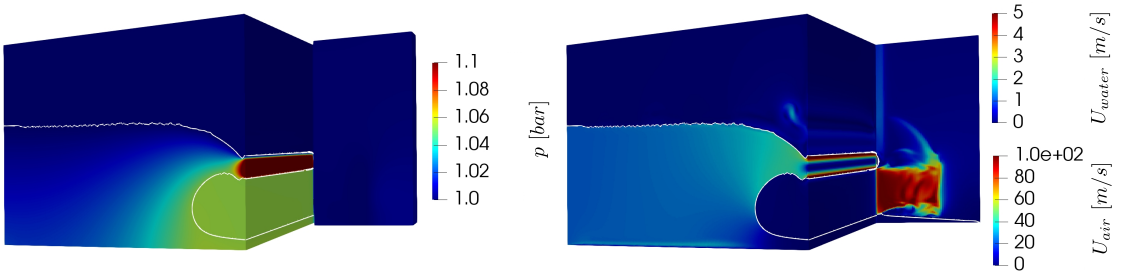

(a) Pressure fields (bar)

(b) Water and air magnitude velocity fields (m/s)

Figure 3.31: 3D velocity and pressure fields after the impact

Fig. 3.31 presents the 3D velocity and pressure fields. Regarding the velocity fields, the water spike decelerates fast when meeting the wall and splits into two high speed jets with velocities up to 5 m/s. The air phase reaches high-speed velocities as it escapes from the entrapped cavity through the aforementioned back-lash, as presented on the image far plane. The pressure fields on the water region have a similar representation as in the 2D compressible configuration. However, the air cavity is depressurised gradually as the air escapes. Here, the pressure gradient is very strong and spatially located close to the back-lash at these initial moments. After running 25 ms, the free surface extracted from a central transverse section is represented and compared to Fig.3.30b. The 2D and the 3D simulations are almost superposed with slightly lower curvatures of the water spike on the 3D computation due to the coarser spatial discretisation on the X and Y direction. The experimental free surface is also represented and the major differences lie in the larger air cavity and a slightly wider water spike experimentally.

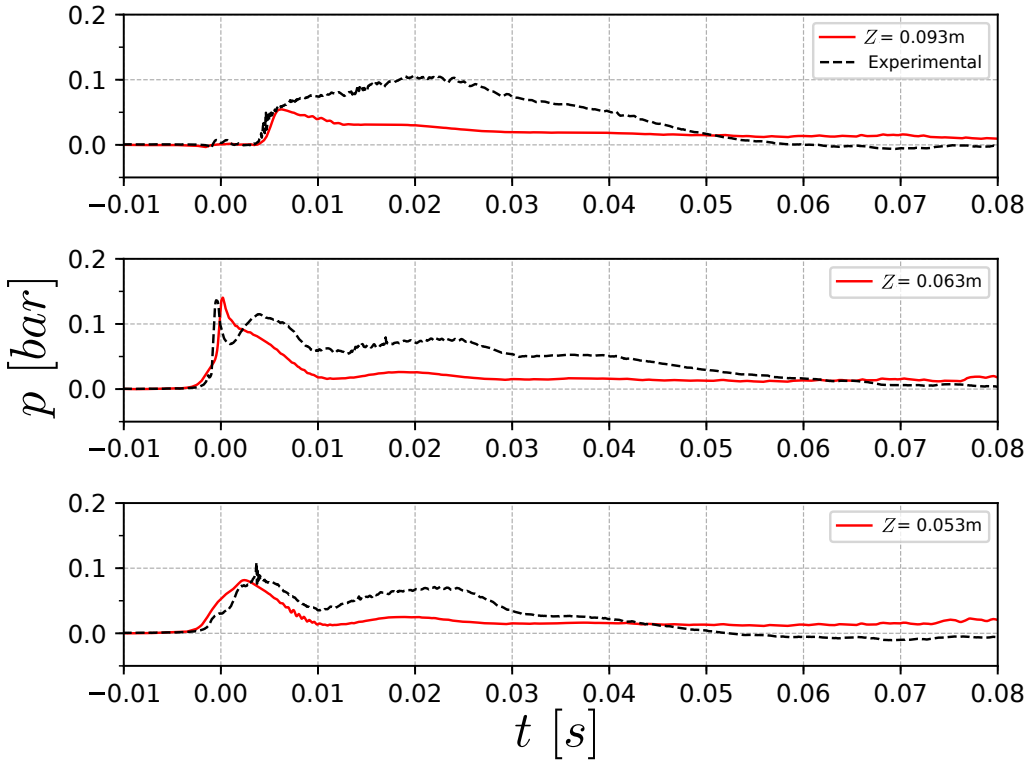

Figure 3.32: Pressure series for 3 different elevations on the plate in a compressible air-pocket impact 3D configuration

Now three representative pressure series, represented by the black squares on Fig.3.30b, are analysed in Fig.3.32. A pressure sensor located above the impact point, $Z = 0.093$ m, will capture principally the splash phenomenon with dynamic pressure range values. Here the pressure rise occurs at similar instants for both experiments and numerics, approximately 5 ms after the peak pressure. The pressure rise have similar slopes reaching 0.06 bar numerically and higher values of ≈ 0.1 bar experimentally, which will correspond to velocities between $2.5 - 3$ m/s. After, the loss of pressure is much faster numerically stabilising around 0.018 bar during the run-up phase.

In the impact region, at $Z = 0.063$ m, two different phenomena explain the recorded pressure series, either experimentally or numerically. The first explanation is related to the cavity compression and overlaps with the temporal serie inside the air cavity region

($Z = 0.053$ m). The second one with higher temporal derivative is related to the impulsive event, the impact of the water spike. A peak pressure of 0.14 bar is numerically obtained and accurately compared to the experiments, although slightly shifted in time. This delay is related to the fact that the maximum pressure peak experimentally of 0.18 bar is reached in a gauge located at $Z = 0.073$ m slightly after the peak pressure at $Z = 0.063$ m. Numerically the impact region has a slightly lower elevation and the maximum pressure value is reached at $Z = 0.063$ m, as it happened in the 2D configuration (see Fig.3.24).

After the impact a second rebound is presented experimentally with values up to 0.12 bar simultaneously with the maximal compression of the air cavity. This second rebound is achieved numerically with lower values of approximately ≈ 0.1 bar. However, the time span between the peak and the rebound is much shorter numerically as the cavity compression is happening earlier. After this rebound, the air flows out from the cavity through the backlash as it gets compressed and a pressure drop occurs without reaching subatmospheric values. Next, a slightly pressure rebound occurs ($0.01 < t < 0.03$ s) as the water splash blocks partially the backlash decelerating the air outflow and, thus, compressing the air cavity again. Here the numeric pressure of 0.03 bar largely underestimate the experimental 0.09 bar, which may be due to a lower blockage of the backlash. Finally, inside the air cavity at $Z = 0.053$ m, a first pressure rebound is well captured numerically in terms of magnitude at 0.08 bar together with a 2 ms time shift. An experimental peak pressure occurs followed by fast oscillation when the cavity reaches it maximal compression ($t \approx 0.005$ s), which should be further studied. After, the pressure falls experimentally and numerically. Although, as it has just been mentioned, the second pressure rebound is being underestimated numerically due to the thermal shock effect on the experimental pressure sensor.

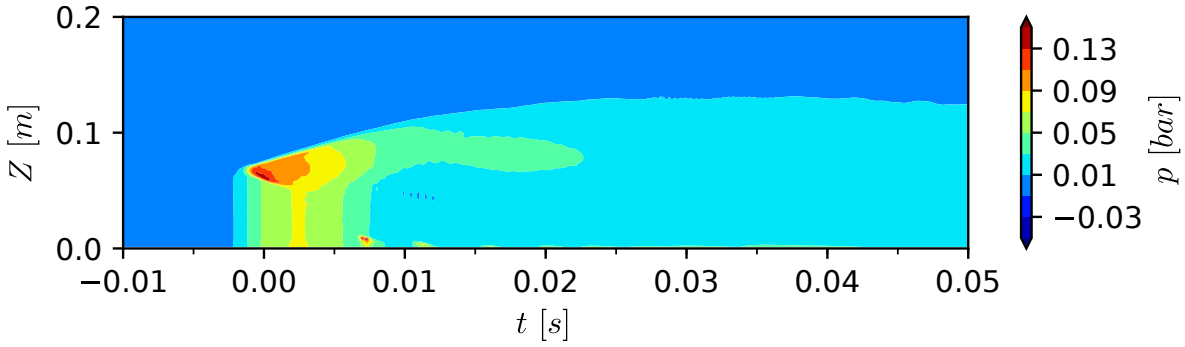

Figure 3.33: Spatio-temporal representation of the wall pressure in the 3D air-pocket impact configuration.

Fig.3.33 present the spatio-temporal representation of the pressure history on the impact plate. Initially a similar behaviour occurs as in the 2D configuration (see Fig. 3.25), while the air cavity is being compressed before the impingement. Just after the water spikes meets the wall, a localised pressure rises up to 0.14 bar is generated slightly below the impact point. As the splash phenomenon develops, it pressurises the wet area. At the same time, the cavity is being compressed until a maximum value is reached pushing the air to outflow through the backlash. The pressure oscillations observed on the 2D configuration are not observable anymore, which was expected in this 3D configuration.

The section has demonstrated the possibility to model an air-pocket wave breaking impact using a 3D configuration and a compressible solver. An expensive high-resolution simulation has been used and aroused the necessity of high computation resources for

reproducing this kind of phenomenons. The pressures series present a fairly good agreement with the experiments quantitatively and qualitatively, by capturing all the relevant phenomenons. This study concluded the possibility to study numerically the physics behind a plunging wave with high air entrapment with the necessity of using a two phase compressible solver.

Chapter 4

Oscillating water column facing a nearshore irregular sea state

This chapter puts together all the experience gained from the previous chapters and adds further complexity. Here an oscillating water column device is evaluated facing a nearshore fully developed irregular sea state. After a short introduction of the irregular waves theory, the performance of the relaxation zone method is evaluated attempting to generate and propagate an irregular sea state over an horizontal plane using a JONSWAP calibration. Next, an oscillating water column device and a sloped beach are introduced reproducing the experimental configuration used in [118]. The ability to model the OWC chamber behavior is studied and compared with the experiments. Finally, three different irregular sea state conditions are investigated with special interest on the front wall pressure exerted by waves. Two of the aforementioned random sea states only produce non-impulsive events and a final one is expected to violent breaking waves impacts on the structure.

4.1 Irregular waves generation and propagation

This section is dedicated to the description of the procedure employed in the present work to reproduce a numerical irregular sea state. The waves are generated using a *relaxation zone method*, a technique that is detailed in Sec. 1.3.2. The irregular wave theory using the summation of several monochromatic waves is derived from the same set of equations which were presented in previous Sec. 3.1.1, namely the kinematic and dynamic boundary condition that read:

$$\frac{\partial \eta}{\partial t} + \left(\frac{\partial \Phi}{\partial x}\right)_{z=\eta} \frac{\partial \eta}{\partial x} - \left(\frac{\partial \Phi}{\partial z}\right)_{z=\eta} = 0 \ , \tag{4.1}$$

and

$$\frac{\partial \Phi}{\partial t} + \frac{1}{2}\left[\left(\frac{\partial \Phi}{\partial x}\right)^2 + \left(\frac{\partial \Phi}{\partial z}\right)^2\right]_{z=\eta} + g\eta = 0 \ . \tag{4.2}$$

However, the case studied here is based on the deep-water wave theory. It uses the assumption of small amplitude waves *i.e.* $a << \lambda$, where a is the wave amplitude and λ is the wavelength. Under this condition, the term $\partial\eta/\partial x$ from eq. (4.1) is much smaller than 1 and may be neglected. Moreover, continuing with the small amplitudes assumption, the terms $(\partial\Phi/\partial x)^2$ and $(\partial\Phi/\partial z)^2$ from eq. (4.2) can also be neglected. This consideration can be demonstrated by using a dimensional analysis, however, this is no developed in the present work.

Finally, the two previous equations now read:

$$\frac{\partial \eta}{\partial t} - \left(\frac{\partial \Phi}{\partial z}\right)_{z=\eta} = 0 \ , \tag{4.3}$$

and

$$\frac{\partial \Phi}{\partial t} + g\eta = 0 \ . \tag{4.4}$$

The bottom boundary is assumed to be horizontal and the fluid to be incompressible. From these equations, a solution for a propagating wave with a single frequency or a monochromatic wave can be derived, which is commonly referred to as Airy, linear or first-order Stokes wave theory.

The irregular waves are obtained by a linear superposition of these single Airy or first-order Stokes waves and the solution for the free surface elevation, for N being the number of wave components, reads:

$$\eta = \sum_i^N a_i cos(\omega_i t - \mathbf{k}_i \cdot \mathbf{x} + \varphi_i) \ , \tag{4.5}$$

where a_i is the amplitude of the i^{th} wave component, ω_i the cyclic frequency, $\mathbf{k}_i$ the wave-number vector and φ_i the a phase. The wave-numbers and the wave frequencies are connected by the dispersion relation,

$$\omega_i^2 = g \ k_i \ tanh(k_i h) \ . \tag{4.6}$$

Finally, the horizontal and vertical velocities are also calculated using a linear superposition of first-order Stokes such as:

$$u = \sum_i^N \frac{2\pi}{T_i} a_i \frac{cosh(k_i(z+h))}{sinh(kh)} cos(\omega_i t - \mathbf{k}_i \cdot \mathbf{x} + \varphi_i) \tag{4.7}$$

and

$$v = \sum_{i}^{N} \frac{2\pi}{T_i} a_i \frac{sinh(k_i(z+h))}{sinh(kh)} sin(\omega_i t - \mathbf{k}_i \cdot \mathbf{x} + \varphi_i) \ . \tag{4.8}$$

The free surface elevation (eq. (4.5)), the dispersion relation (eq. (4.6)) and both horizontal and vertical velocities (eq. (4.7) and (4.8)) are the core of the irregular wave theory based on monochromatic waves. The obtained results from these free surface and velocity formulas are then introduced as target solutions within the *relaxation zone method* for generating the waves conditions (See Sec. 4.1.3).

4.1.1 JONSWAP wave spectrum

Real sea state conditions are characterized by random waves, whose spectral representation can generally be represented by Pierson-Moskowitz or JONSWAP spectra. These spectral representations of irregular sea states can be applied for fully or partly developed seas. The present work uses the JONSWAP spectrum to calibrate the irregular sea state, which is suitable for a fully developed sea states generated by winds blowing for a long time over a large area of sufficient fetch length. The fetch length is defined by the distance over which the wind blows with constant velocity. Such hypothesis are generally validated for sites where wave energy devices, and especially OWC, are placed. This JONSWAP spectrum was proposed after analysing data collected during the Joint North Sea Wave Observation Project (JONSWAP) [119] and adds an extra peak enhancement factor to the Pierson-Moskowitz spectrum. The spectrum takes the following form:

$$S(f) = \frac{\alpha H_s^2 f_p^5}{f^5} exp\Big[-\frac{5}{4}\Big(\frac{f_p}{f}\Big)^4\Big] \gamma^{exp\Big(-\frac{(f-f_p)^2}{2\sigma^2 f_p^2}\Big)} \ , \tag{4.9}$$

where H_s is the significant wave height and f is a wave frequency. The coefficient α is known as the Phillips constant, empirically related to the fetch length and wind speed 10 m above the free surface. Here, α is calculated as follows:

$$\alpha = \frac{0.0624}{0.23 + 0.0336\gamma - \frac{0.185}{1.9+\gamma}} \ . \tag{4.10}$$

γ is the peak enhancement factor, which takes a value of 3.3. f_p is the peak frequency and σ is a relative measure of the peak width. Here, σ takes the recommended value:

$$\sigma = \begin{cases} 0.7 & \text{for } f \leq f_p \\ 0.09 & \text{for } f > f_p. \end{cases}$$

By selecting $\{H_s, T_p\}$ the spectrum is defined relating each frequency f with a spectral density associated $S(f)$ and, thus, a wave amplitude. The resultant spectrum is then discretised into independent waves obtaining a list of N components of amplitudes a_i and frequencies f_i which are introduced into eq. (4.5), (4.7) and (4.8). The wave-numbers $\mathbf{k}_i$ are then calculated using eq. (4.6) and the wave phases φ_i are selected randomly. The present work only imposes a limited range of spectral frequencies ($f_p/2 < f_i < 3f_p$), which is representative of the real sea state.

4.1.2 Spectral density estimation

A way to characterise a random sea state is usually by recording the free surface elevation at given locations. However, this is not representative by itself due to the statistical properties

of the signal. Then, a representation over the frequency domain is often envisaged and calculated using techniques based on the fast Fourier transform algorithm. The present work uses a slightly more sophisticated approach by taking advantage of the Welch's method [120].

This method has already been tested and demonstrated to be suitable for an efficient reconstruction of the sea state parameters starting from a random wave time history by Rossi *et al.* [121] for instance. The method consists of parsing the data record into smaller segments with partial overlap. The periodogram [122], which is the square of the Fourier transform, is calculated for each segment and the final spectrum is obtained by averaging over them. Typically, the signal is split into $512 \cdot n$ segments, where n is an even number, and the segment overlap is set to 50%.

4.1.3 Generation and propagation of an irregular sea state

In this section, the capabilities of the relaxation zone method for generating and absorbing irregular waves will be tested and validated. For this purpose, a simple rectangular numerical wave tank (NWT) in 2D (see Fig. 4.1) is used to generate, propagate and absorb irregular waves. The numerical wave tank geometrical characteristics are summarized in Tab. 4.1. So far boundary conditions are concerned, the top boundary is defined as an open boundary with a total pressure where air and water can freely flow out and only air can flow in. The bottom boundary is defined as a solid wall with a no-slip condition; the inlet and outlet boundaries have the prescribed velocity and free surface elevation conditions given by the relaxation zone method. All over the domain, a structured grid is used with a cell aspect ratio of $\Delta x/\Delta z = 2$, where Δz refers to the cell height. Additionally, around the free surface, a refined region is defined where the cell sizes are divided by two. Keeping the same mesh for the different configurations, this leads to different ratios of the number of cells per significant wave height $H_s/\Delta z$ or wavelength $\lambda_p/\Delta z$. These ratios are presented in table 4.2. The physical cell dimensions on the free surface region are kept as $\Delta x = 10$ cm and $\Delta z = 5$ cm. The time discretisation is adjustable and limited by a maximum Courant number condition of `maxCo`$= 0.8$ ($maxCo = mag(U) \cdot \Delta t/\Delta x$, where $mag(U)$ is the velocity magnitude and Δt is the time step) in the vicinity and away from the interface. Before a discussion of the results from the simulations, it is important to highlight the coarse spatial and temporal discretisation of this simulation to evaluate the limit of both accuracy and time consumption for large stochastic simulations. These simulations consider the presence of any relevant turbulence phenomenon to be negligible and a laminar model is selected.

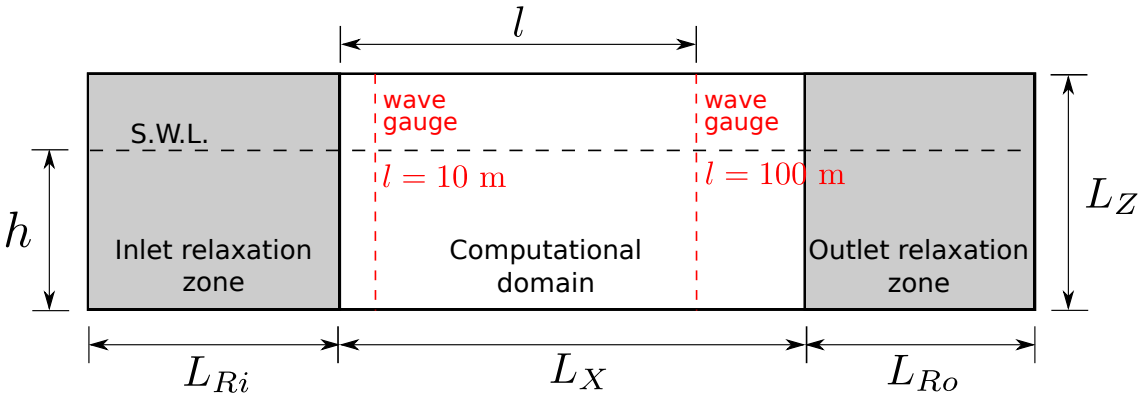

Figure 4.1: Geometrical definition of the numerical wave tank.

Table 4.1: Numeric wave tank dimensions

L_{Ri} (m)	50
L_{Ro} (m)	20
L_X (m)	130
L_Z (m)	6

In the presented simulations, and more generally all over the present study, random waves are generated using $N = 100$ wave components and a random phase seed φ. Increasing the number of wave components has shown to proportionally increase the computational time consumption without any clear improvement of the solution. The total physical time duration is defined as $500\,T_p$ to capture the statistical properties of the considered irregular sea state. For this validation section, three waves conditions will be tested. The major difference between these three sea states is the wave steepness, defined as $s = H_s/\lambda_p$ and presented in Table 4.2. Two numerical wave gauges are located $l = 10$ m and $l = 100$ m away from the end of the relaxation zone inlet region and record the free surface elevation every 0.05 s. From these temporal series, a spectrum is calculated and compared with the input spectrum as depicted in Fig. 4.2. From these figures, the three configurations are fairly well reproduced compared with the imposed spectrum 10 m away from the inlet relaxation zone. The configuration with the highest steepness $s = 0.03$ has the worst solution when observing the peak frequency and higher frequencies related energy. This last phenomenon is also observable, with a lower appreciation, on the second steepness configuration $s = 0.02$. On the other hand, the wave gauge located $l = 100$ m away from the relaxation zone is a clear indicator of the propagation stage. For the lowest steepness, $s = 0.01$, the sea state energy distribution and magnitude are surprisingly well conserved. Conversely, the higher steepness configurations present a more dissipative behaviour, which can be attributed to the coarse temporal and spatial resolution, see Tab. 4.2. Moreover, hardly any reflection effects are appreciable on any of the computed spectrum.

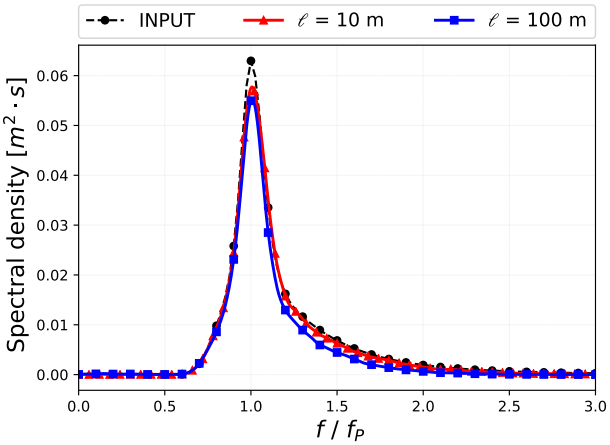

(a) $H_s = 0.26$ m $T_p = 4.5$ s $s = 0.01$

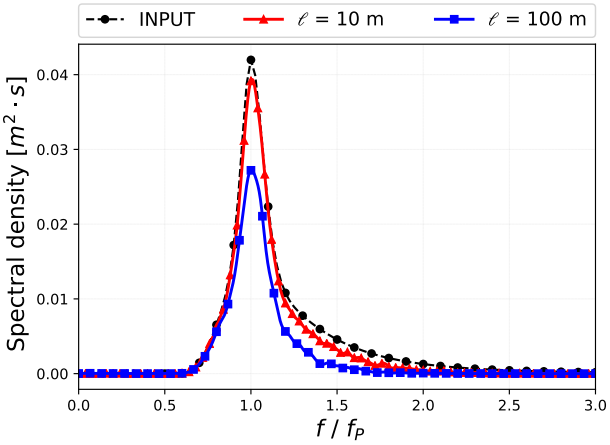

(b) $H_s = 0.26$ m $T_p = 3$ s $s = 0.02$

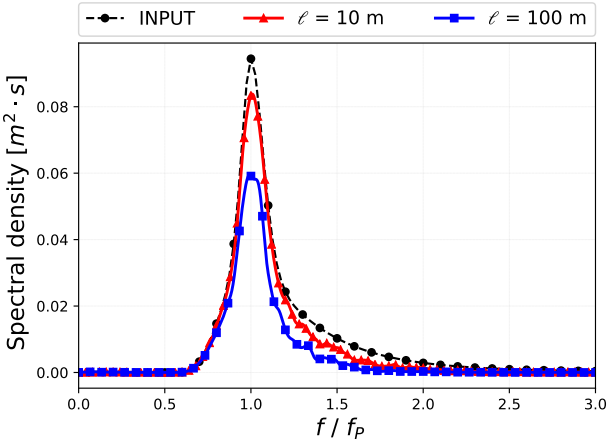

(c) $H_s = 0.39$ m $T_p = 3$ s $s = 0.03$

Figure 4.2: Spectral analysis of different simulated irregular sea states compared with the input spectrum following a JONSWAP calibration. The spectrum is obtained from a free surface elevation temporal series at two locations $l = 10$ m and $l = 100$ m away from the generation boundary, see Fig. 4.1

Table 4.2: Simulation results

H_s	T_p	H_s/λ_p	$H_s/\Delta z$	$\lambda_p/\Delta z$	H_{m0}		H_{max}	
					l=10 m	l=100 m	l=10 m	l=100 m
0.26	4.5	0.01	5	233	0.259	0.238	0.442	0.442
0.26	3	0.02	5	130	0.248	0.199	0.429	0.368
0.39	3	0.03	8	130	0.366	0.301	0.578	0.567

The results are quantified in Tab. 4.2 by making use of the wave height related to the spectrum zeroth momentum $H_{m0} = 4\sqrt{m0}$ together with the maximum wave height directly extracted from the free surface temporal signal. The significant wave height H_s is a user-defined value in this table and it can be extracted directly from the free surface temporal serie. On the other hand, the zeroth momentum wave height H_{m0} is a statistical parameter calculated from the wave spectrum. Regarding the results of the first configuration ($s = 0.01$), the previous analysis is further confirmed with errors for the significant wave height under a 1% for the generation sensor ($l = 10$ m) and around 8% for the propagation sensor ($l = 100$ m). Moreover, the rule of thumb typically employed to calculate the maximum wave height (*i.e.* $H_{max} \approx 1.8H_s$) seems to be pretty accurate. The second configuration ($s = 0.02$) presents a significant wave height error of 4.5% in the vicinity of the wave generator and a non-negligible 23% for the sensor 100 m away. Again, the maximum wave height is in line with the zeroth momentum wave height. Finally, the last configurations ($s = 0.03$) have the highest errors with 6% and 22.8% for the two sensors, whereas the maximum wave height seems to be underestimated when compared to the rule of thumb formula.

This section has covered three different irregular sea state configurations evaluating the generation and propagation accuracy using a certain discretisation. Affordable computational times for very long simulations was one of the objectives of the present section and this is the main reason why fairly low discretisations are employed. One may conclude a good performance of the generation method under these conditions. A fairly good accuracy for propagation over reasonable length has been observed, but high dissipation of the wave heights for longer distances ($\approx$ 100 m). However, a lower accuracy of the propagation stage is not surprising due to the remarkable length of the numerical wave flume combined with the present discretisation. Finally, in the forthcoming sections the propagation lengths are in the order of ($\approx$ 20 m) and the previous study gives confidence for pursuing with the methodology employed here.

4.2 Experimental setup and numerical configuration

4.2.1 Definition of the experimental configuration

The forthcoming numerical results will be compared with the experimental data-sets obtained from Allsop *et al.* [118] dealing with *Large scale tests on a generalised oscillating water column wave energy converter*. This experimental study was led by Dr. Tom Bruce in the Grosse Wellenkanal (GWK) under the Hydralab IV project. Several authors already analyzed the obtained experimental results. On the one hand, Viviano *et al.* 2016, 2019 [123, 124] characterized reflection coefficients, exerted pressures on the exterior and interior of the OWC curtain wall, and compressibility effects inside the OWC chamber. On the other hand, and more recently, Pawitan *et al.* 2019, 2020 [18, 125] further explored the wave loads and pressures on the structure front wall and proposed an extension to

the Goda [28]'s formulation. Dimakopoulos *et al.* 2015 [126] numerically reproduced the chamber behaviour under regular waves and this piece of work has been of great help for the current study. Nevertheless, an incompressible solver was employed at that time which presented some limitations under certain circumstances. However, Dimakopoulos *et al.*'s results will be used as a matter of comparison and further validation.

(a) (b)

Figure 4.3: Photos from the experimental setup during the installation and the OWC undergoing a wave interaction

These experiments were designed at a nominal Froude scale of approximately 1:9 relative to a prototype. The flume was 307 m long, 7.0 m deep and 5.0 m wide and the OWC structure (Fig. 4.4) was 97.5 m away from the piston paddle wave-maker. The structure was composed of 3 chambers as one can see from Fig. 4.4(a) with a 1 in 6 slope rising from the flume floor to the structure foot.

Multiple wave gauges (WG01-WG04) were located halfway between the wave-maker and the structure and also in front of the structure (WG05-WG08). The central caisson had five free-surface elevation gauges (WG09-WG13) inside the chamber, which can clearly be identified from the schematic representation of Fig. 4.4. The acquisition frequency for all wave gauges was set to 100 Hz. The central caisson was equipped with multiple pressure transducers (General Electric Druck PDCR 1830) measuring air and water-induced pressures on the front face, internal back wall and roof of the caisson. These pressure transducers are also clearly identifiable from Fig. 4.4. The pressure transducers sampling rate was set to 1 kHz for all test cases. Finally, a differential pressure transducer also measured the effects of an adjustable orifice. This adjustable orifice was installed to control the air flows in and out of the caissons chambers, via the $0.5\,m$ diameter tubes or chimneys (see Fig. 4.4 and the three of them in Fig. 4.4(a)), altogether mimicking a power take-off (PTO) device. Various openings of the adjustable orifice were tested during the experiments, these a referenced by using an open orifice diameter against the chimney diameter (d_0/D), where $d_0/D = 0$ means a completely closed orifice and $d_0/D = 1$ a fully opened situation. This ratio is expected to have a a great effect on the chamber behaviour, e.g. using small ratios the air inside the chamber presents compressibility effects. The experiments were run through a series of regular ($Reg\#$) and random ($Irr\#$) wave conditions. And some of the relevant ones for the present study are detailed in Tab. 4.3.

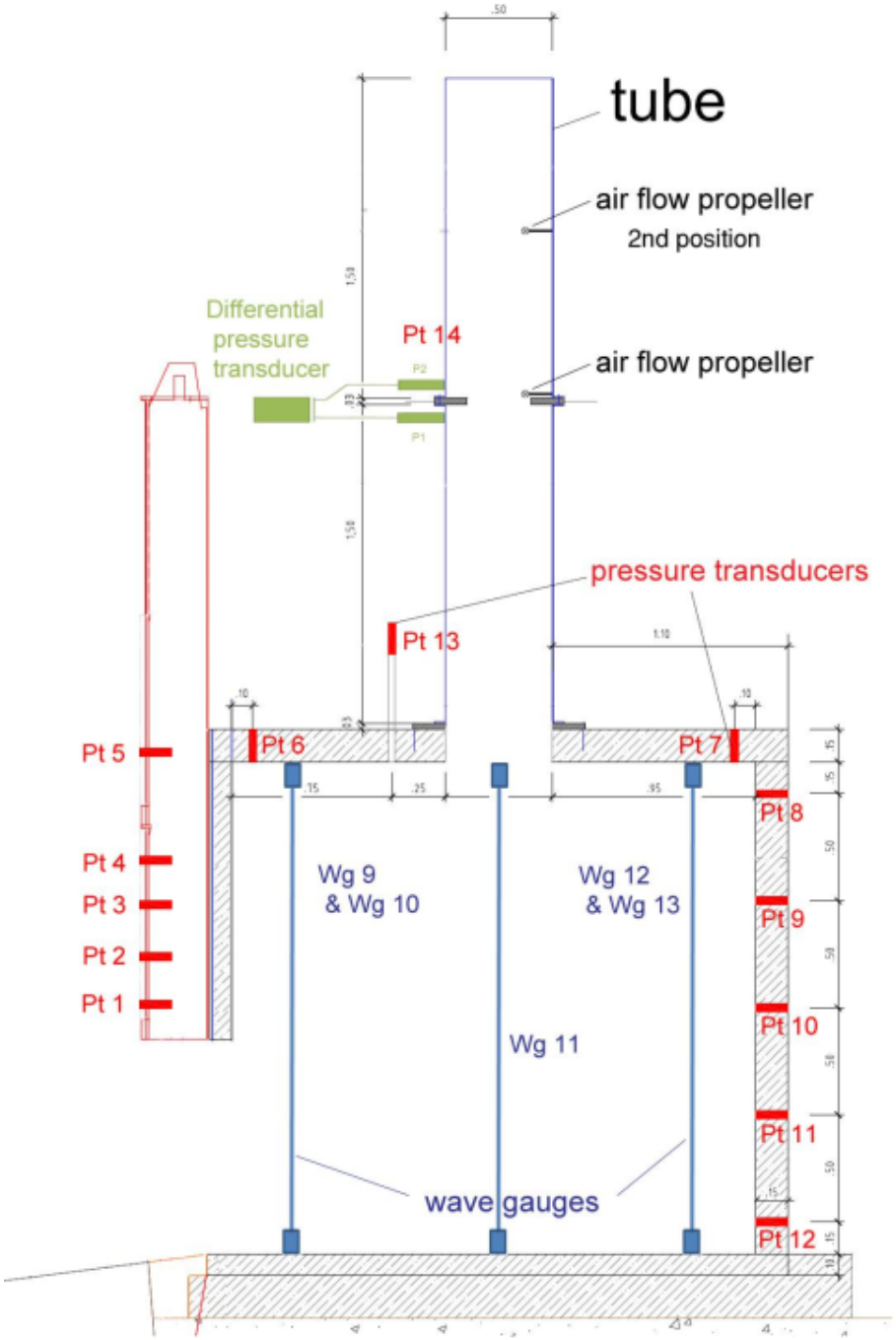

Figure 4.4: Cross section of OWC model, showing (qualitatively) the locations of pressure transducers (red) and wave gauges (blue)

4.2.2 Data analysis

As aforementioned, all pressure transducers had a high acquisition frequency of 1 kHz. This was necessary to accurately describe possible impulsive loads related to breaking waves. However, this induced a non-negligible noisy signal and occurrences of some non-physical oscillations. This issue was already addressed in Viviano *et al.* [123] for the impulsive pressure series. But the lack of information has motivated the present authors

Table 4.3: Summary of wave conditions

Regular waves

Ref	H [m]	T [s]	h [m]	H/λ [-]	d_0/D [-]
*Reg*6.05	0.4	4	3.5	0.02	0.6
*Reg*6.10	0.4	4	3.5	0.02	0.1

Irregular waves

Ref	H_s	T_p	h	H_s/λ_p	d_0/D
*Irr*01.10	0.26	3	3.5	0.02	0.6
*Irr*13.01	0.26	4.5	3.5	0.01	0.4
*Irr*11.07	1.0	6.0	3.5	0.03	0.4

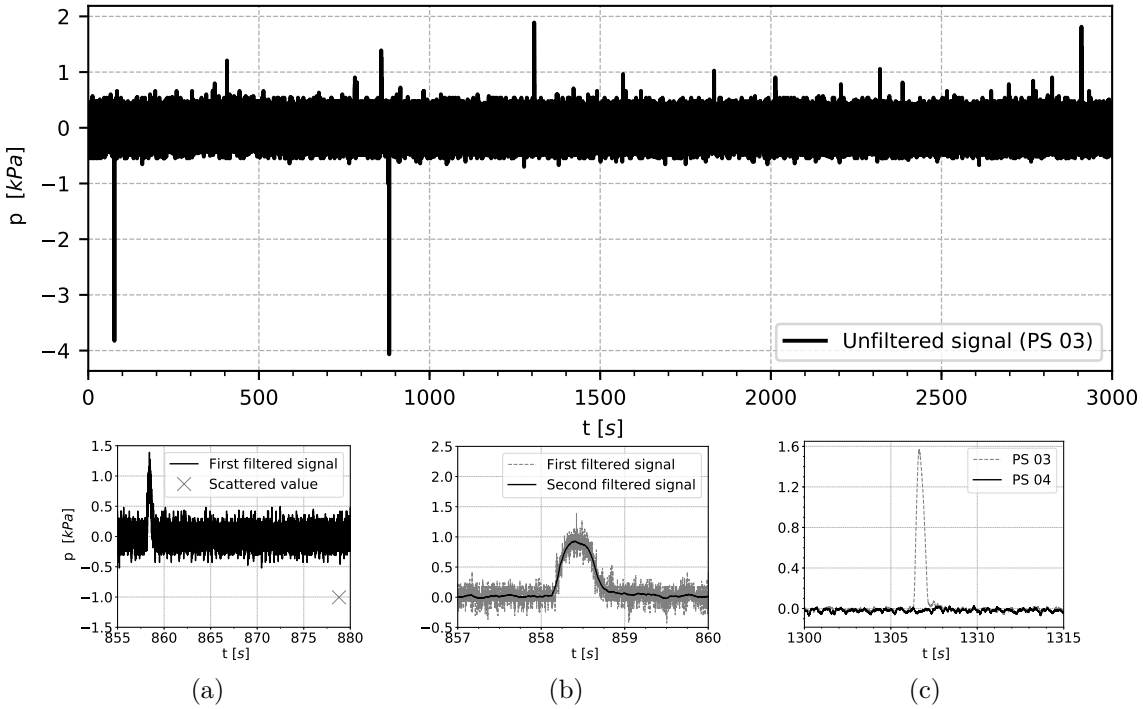

Figure 4.5: Pressure signal recorded by transducer (P3), located on the front wall. Test conditions Irr01.10 are: $H_S = 0.26$ m, $T_P = 3$ s and $d_0/D = 0.6$.

to develop a new filter for a better assessment and understanding of these experimental pressure signals.

Regarding the configurations without any impulsive event, the temporal scale of all the relevant phenomenons is at least 0.1 s, which is two orders of magnitude larger than the acquisition time step of 1 ms. Under this assumption, three main aspects are addressed for filtering the original signal, as depicted in Fig. 4.5.

1. First, some scattered values can easily be identified as the one depicted at the bottom

right of Fig. 4.5a for $t \approx 879$ s. These scattered values are removed from the series using a filter (eq. 4.11) based on a local variance:

$$(p(t_i) - p(t_{i\pm1}))^2 > 25 \cdot \left[\frac{1}{100} \sum_{n=i-50}^{i+50} (p(t_n) - \overline{p}(t_{i-50} < t < t_{i+50}))^2 \right] , \qquad (4.11)$$

where $\overline{p}$ refers to the mean value within the interval. Each pressure value $p(t_i)$ difference with the previous and the following value (t_{i-1}, t_{t+1}), where t_i is the current time-step, is compared against the average variance of the 50th previous and following values. If one of the local differences is higher than 25 times the local variance, the value is removed from the signal.

2. Secondly, a smoothing filter is used by averaging each value $p(t_i)$ over the (t_{i-50}, t_{t+50}) consecutive values, see Fig. 4.5b.

3. Finally, a qualitative analysis is carried out for the two highest pressure sensors (PS 04 - 05) by observing if any wave reached that elevation. To do this, the instants related to the highest waves are identified by looking at the pressure series (p_{max}) from (PS 01 - 02 - 03). Then, the pressure series from (PS 04 - 05) are observed at those instants and if there is any relevant pressure rebounds occurring (see Fig. 4.5c), it is assumed that the wave did not reach that elevation. If any of the two highest waves observed is captured by the two highest pressure sensors (PS 04 - 05), it can be concluded that the pressure signal related to wave loads is zero at that location.

4.2.3 Mesh and time discretisation

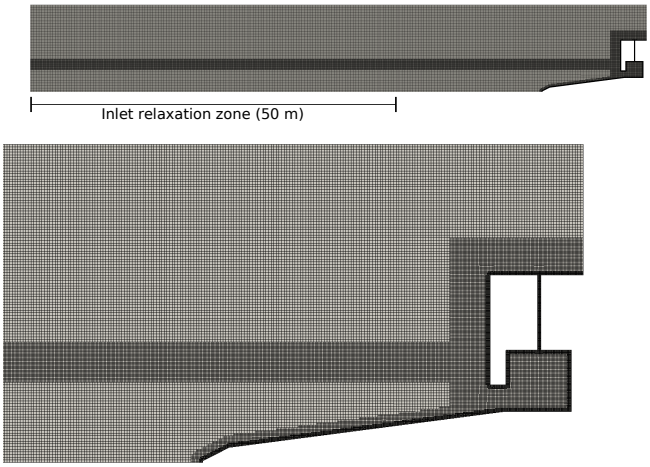

Figure 4.6: Full mesh snapshot and a detail of the mesh in the vicinity of the OWC.

The employed numerical wave flume used to validate the experiments previously detailed in Sec. 4.2.1 is 84 m long and 12 m high using a 2D configuration. The relaxation zone, motivated by the results of Sec. 4.1.3, is 50 m long (see top of Fig. 4.6) having the possibility to allocate more than one wavelength in the present conditions. Boundary conditions are set to a solid wall with a no-slip condition for the flume bottom, sloping beach and structure. While the top boundary is left as an open boundary imposing a total pressure condition, where air and water can freely flow out and only air can flow in. The computational domain is discretised into a structured grid (see Fig. 4.6). To optimise

computational times, a variable grid is defined (see bottom of Fig. 4.6), with a higher resolution around the free surface and close to the structure and beach boundaries. Δx is defined as the horizontal cell size and Δz the vertical one. The grid cell size is selected to maintain an aspect ratio $\Delta x/\Delta z = 1$ throughout the entire computational domain with a characteristic value of $\Delta x = 0.1m$. In the refinement areas and at the free surface, Δx is reduced (divided by 2) to obtain a value of $\Delta x = 0.05m$, keeping a low wave height/grid size ratio of $H/\Delta z = 8$ for the regular wave cases. This allows to reduce the computational time costs while keeping a fairly reasonable accuracy. Nevertheless, the analysis carried out in Sec. 4.1.3 showed this range of grid size to be enough for a variety of irregular wave configurations. Finally, the cells size surrounding the beach and the structure are even further refined to a value of $\Delta x = 0.025m$.

An adaptive time-stepping is employed for the time discretisation using a maximum Courant number `maxCo` $= 0.4$. Although this is higher than the literature recommendations to obtain stable wave profiles, it is selected for balancing accuracy and computational costs. All the simulation that will be presented in the next sections are summarised in Tab. 4.4.

Table 4.4: Summary of simulations

Regular waves

Ref	H/Δz	$\lambda/\Delta x$	`maxCo`	Solver	Turbulence model	Physical time
	[-]	[-]	[-]	[-]	[-]	[s]
*Reg*6.05						
	8	400	0.4	incompressible	laminar	100
	8	400	0.4	compressible	laminar	100
*Reg*6.10						
	8	400	0.4	incompressible	laminar	100
	8	400	0.4	compressible	laminar	100

Irregular waves

Ref	$H_s/\Delta z$	$\lambda_p/\Delta x$	`maxCo`	Solver	Turbulence model	Physical time
*Irr*01.10						
coarse	5	262	0.4	incompressible	*mod* $k-\omega$ SST	3000
refined	7	349	0.4	incompressible	*mod* $k-\omega$ SST	3000
*Irr*13.01						
	5	466	0.4	incompressible	*mod* $k-\omega$ SST	4500
	5	466	0.4	compressible	$k-\omega$ SST	4500
*Irr*11.07	20	657	0.4	compressible	$k-\omega$ SST	2000

4.2.4 Power take-off damping with porous material

In the present work, similarly as in previous studies [126], a porous layer is introduced numerically to model the adjustable orifice behaviour. Firstly, when converting the 3D experimental domain into a 2D model, the opening of the slot is redefined to keep the same orifice area. To do this, the initially circular tube is assumed to be a rectangle and its width can be calculated using the following formula:

$$w = \frac{A_0}{B} \ , \tag{4.12}$$

where w is the slot width, A_0 is the orifice area and $B = 1.45m$ is the OWC chamber transverse width. Hence, the slot width is defined here such as $w = 0.14m$. According to [127], the PTO pressure damping can be consistently represented using a porous membrane, which establishes a linear-quadratic relation concerning the flow rate, according to:

$$P = k_1 q + k_2 q^2 \ , \tag{4.13}$$

where k_1, k_2 are damping coefficients and q the flow rate. Experimentally, this flow resistance is achieved by using an adjustable orifice. It is well known that impulse turbines, commonly used for converting pneumatic power to shaft power, have a non-linear behavior [128]. Thus, in the present work only the quadratic term is kept and, for an orifice plate, the resistance coefficient can be calculated using:

$$k_2 = \frac{\left[1 - C_C\left(\frac{d_0}{D}^2\right)\right]^2}{C_C^2\left(\frac{d_0}{D}^4\right)} \ , \tag{4.14}$$

where C_C is an empirical contraction coefficient as detailed in [129]. Numerically, this resistance is modelled utilizing a porous membrane obeying the Darcy-Forchheimer law, according to:

$$\frac{\nabla P}{\rho g} = a\mathbf{u} + b|u|\mathbf{u} \ , \tag{4.15}$$

where a, b are the Darcy and Forchheimer coefficients, respectively. This equation is introduced in the momentum equation as a source term acting only on the porous region.

4.3 OWC chamber under regular waves

This section aims to properly characterise the behaviour of both fluids inside the OWC chamber. For this purpose, experimental configurations using two regular wave conditions are chosen for a sake of simplicity. Also, Dimakopoulos *et al.* [126]'s paper used this precise configuration for their numerical computations, enabling interesting comparisons. The main differences between the two considered conditions are the orifice opening within the airflow tube (see Tab. 4.3). For this analysis, and following the methodology proposed by Dimakopoulos *et al.* [126], free surface evolution inside the chamber is presented in Fig. 4.7 by averaging over three wave gauges, WG10-WG11-WG12 of Fig. 4.4. During the experiments, the averaging procedure was performed over 5 wave gauges to account for 3D effects. The numerical scheme and parameters are those presented in Table. 4.4. Fig. 4.7a presents the free surface elevation recorded by each of the numerical wave gauges and Fig. 4.7b presents the averaged solution over 25 wave periods. Although the different

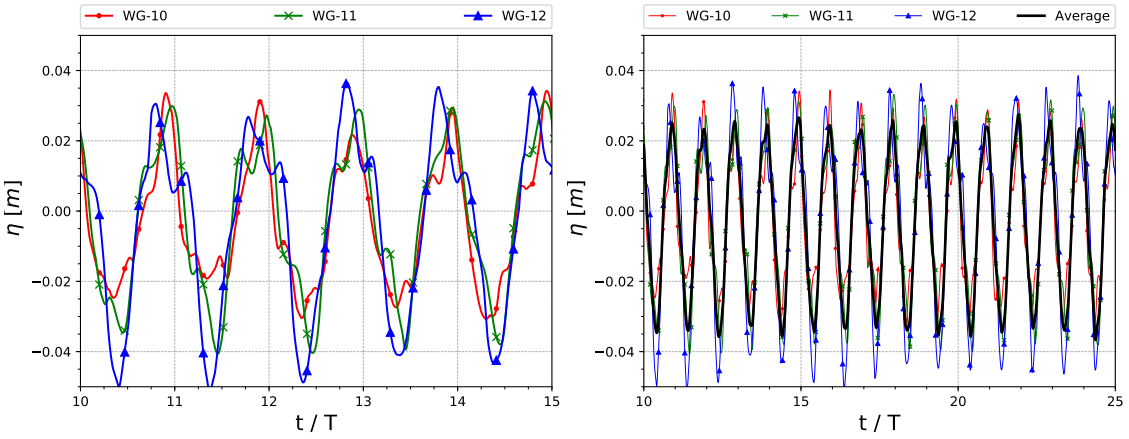

(a) (b)

Figure 4.7: Numerical in-chamber free surface elevation averaged over the three wave gauges WG10-WG11-WG12 of Fig. 4.4 issuing from a compressible computation. Test conditions Reg06.10: $H = 0.4$ m, $T = 4$ s and $d_0/D = 0.1$.

motion of the free surface on each of the wave gauges, a fairly well conservation of the free surface motion is observed when averaging over them.

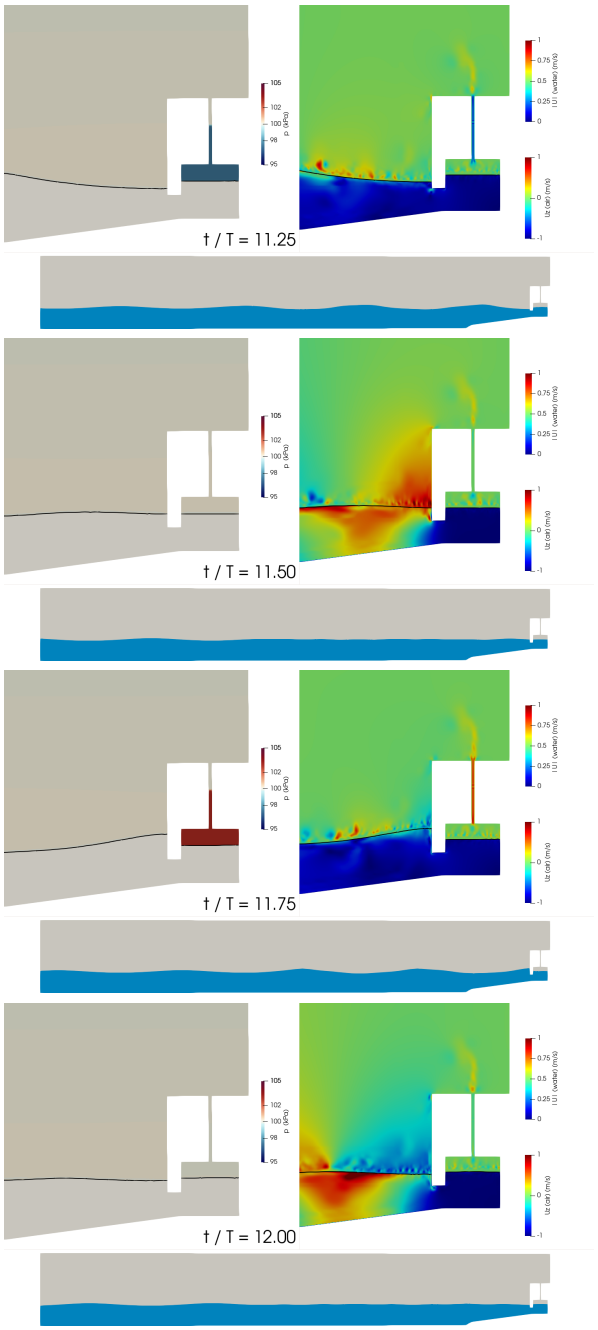

Figure 4.8: Snapshots of an four relevant instants of an OWC undergoing an air-chamber compression and expansion process. Each instant presents (top left) absolute pressure for air p (kPa), (top right) velocity magnitude for water $Mag(U)$ (m/s) and vertical velocity for air Uz (m/s) and (bottom) water representation $\alpha > 0.5$.

Four selected snapshots are presented in Fig. 4.8 during an oscillating process caused by regular incoming waves (test case Reg6.10 of Tab. 4.3). Results are obtained using the compressible solver and orifice opening is defined as $d_0/D = 0.1$. In the first image ($t/T = 11.25$), the free-surface elevation is near still water level while it is going down and an incoming wave approaches the trough. Air pressure inside the chamber has the minimum sub-atmospheric values and air is rapidly flowing inside the chamber. Presence of spurious velocities in the light phase (air) are observable in the vicinity of the interface.

The imbalance in the momentum equation, which causes a vertical acceleration of the air phase, was highlighted in previous sections to be the cause of such phenomena. It was also the matter of study by different authors [67, 68]. Next, for $t/T = 11.50$, air is still flowing into the chamber while the incoming wave approaches the structure. Free-surface elevation approximates its minimum and in-chamber pressure is close to atmospheric value. Free-surfaces inside and outside the chamber have the same elevation. At $t/T = 11.75$, air inside the chamber is fully compressed and flows out rapidly through the tube. The wave reaches the highest run-up on the front exterior wall and the free surface inside the chamber is again close to the still water level. In the last snapshot ($t/T = 12$), air is still flowing out from the chamber while the exterior wave is reflected away from the structure. Free-surface elevation approximates its maximum and the pressure is close to the atmospheric values. A vortical structure is observable close to the bottom corner of the curtain wall.

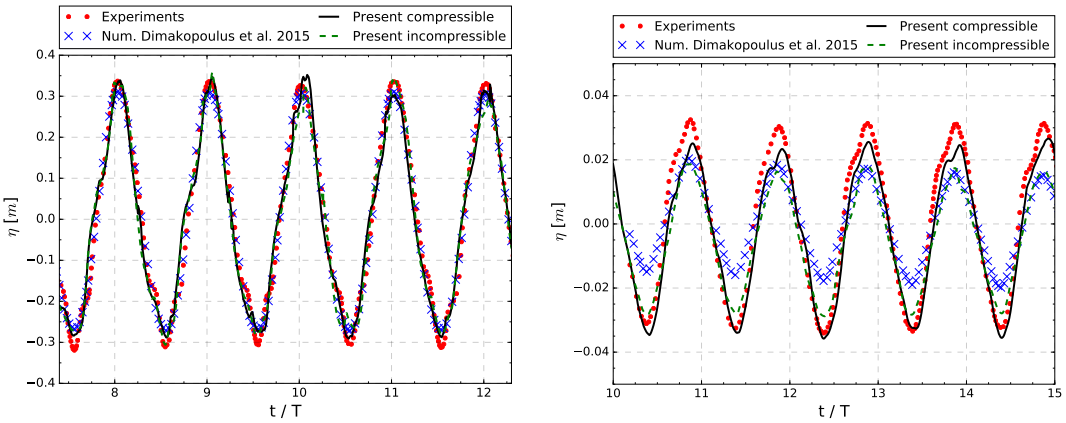

(a) $d_0/D = 0.6$ (b) $d_0/D = 0.1$

Figure 4.9: In-chamber free-surface elevation averaged over three wave gauges.

Based on these observations, it is now time for analysing more into detail these two regular wave configuration using in-chamber free-surface elevation records. In the first configuration (test case Reg6.05 of Tab. 4.3), using an orifice opening ratio of $d_0/D = 0.6$, very few air compressibility effects are expected. Under these conditions, Fig. 4.9a presents different free-surface evolution. The present numerical results are compared with the experiments and the numerical ones of [126] using an incompressible approach. Results are just shifted in time so that the maximum elevation happens at the same instant for all the data-sets. A good agreement between the present work, the experiments and the previous numerical results is observable. Moreover, and as expected, differences between results issuing from compressible or incompressible solver are negligible due to the low resistance of the adjustable orifice. On the other hand, by reducing the orifice opening ratio to $d_0/D = 0.1$, air compressibility effects are now remarkable from Fig. 4.9b. For this $d_0/D = 0.1$ configuration, experimental and both incompressible numerical show to have a poor agreement. The present compressible solution proved to have a much better behaviour and tends to the experimental curve. However, some discrepancies are still noticeable. These differences are mainly due to a low mesh resolution around the tube and the chamber compared to the previous numerical results of M. Batlle *et al.* 2020 [130]. The present work aims to reduce, as much as possible, the spatial and time discretisation for consistency with the incoming sections where highly computationally demanding simulation will be run. Differences with the experiments may also be explained

by 3D effects to some extent.

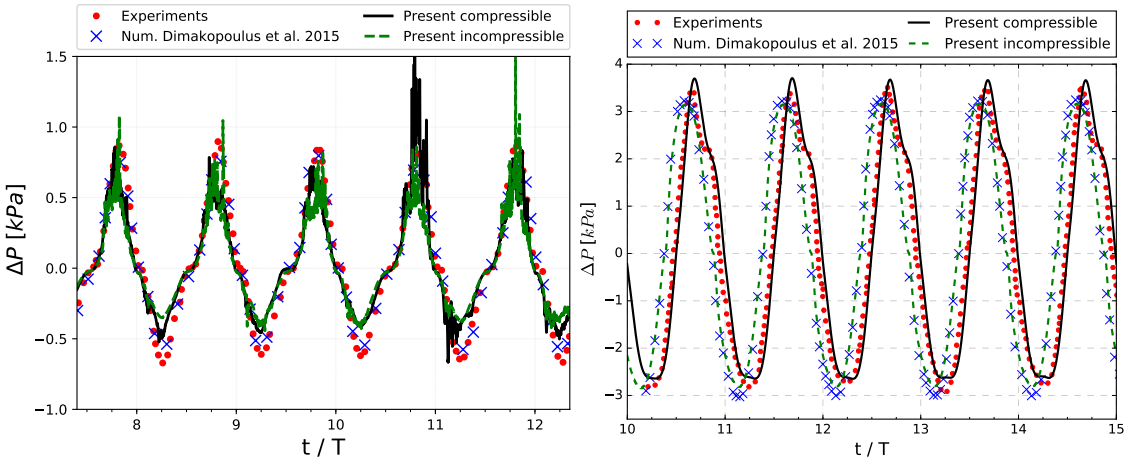

(a) $d_0/D = 0.6$ (b) $d_0/D = 0.1$

Figure 4.10: Pressure difference across the adjustable orifice.

Figure 4.10 presents temporal series of pressure differences across the power take-off (PTO), being a relevant parameter for measuring the power that can be extracted from the system. Similarly as for the surface-elevation signals, these results are shifted in time with the exact same time lag extracted earlier. A positive pressure difference indicates a greater pressure inside the chamber that outside. For the lower resistance orifice, Reg06.05 configuration with $d_0/D = 0.6$, a fairly good agreement is obtained between both numerical approaches and the experiments, capturing the quadratic nonlinearity of the experimental signal near the zero-crossing. As mentioned before, the differences between the compressible and the incompressible solvers are very little for this configuration. The pressure fluctuations are caused by some instantaneous non-realistic high velocities which may appear on singular cells due to the coarse mesh and the high-speed air flowing inside or outside the cavity. This could be solved by computing the pressure difference between several cells above and below the porous medium. Regarding the results of the orifice opening $d_0/D = 0.1$ (Fig. 4.10b), the role of air compressibievel itity is now distinctive. Experimental and compressible numerical results are shifted in time compared with the incompressible results, both issuing from Dimakopoulos *et al.* [126] or with the present approach. This effect is caused by the compressibility acting like a mechanical spring in phase with the chamber free-surface elevation motion rather than velocity. Moreover, quadratic non-linearity is also captured slightly after the air inside the chamber is fully compressed, which can be observable e.g. at $t/T \approx 10.75$ or $t/T \approx 11.75$ on Fig. 4.10b. The above-mentioned analysis gives the authors confidence to continue into more complex scenarios using random waves and a logical range of applicability of the incompressible ($d_0/D \geq 0.6$) and compressible ($d_0/D \leq 0.1$) approaches. Moreover, even if the mesh resolution employed here was rather coarse, it can be concluded to be sufficient enough to properly model in-chamber phenomena.

4.4 Irregular waves pressures on the OWC front wall

This section is dedicated to the numerical evaluation of wave induced loads exerted by different irregular sea-states on the OWC exterior carapace. The pressure fields on the

curtain wall are the result of complex wave interaction processes that enclose multiple relevant phenomena, such as:

- Generation and absorption of an irregular sea-state
- Wave transformation over the sloped plane
- Wave-structure interaction
- Pneumatic chamber behaviour

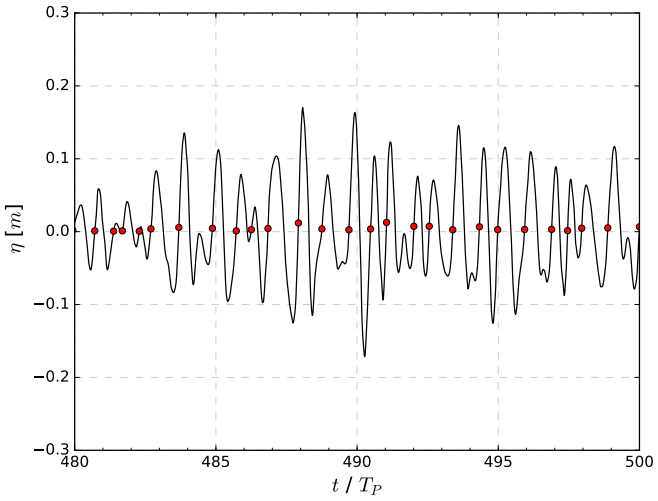

Figure 4.11: Representation of the free surface elevation with the wave division (red points) one meter away from the structure (WG-08)

In a random sea environment, the assessment of a single wave event is not trivial. However, in order to have a first level of analysis, each individual wave will be detected and identified as depicted in Fig. 4.11. This identification is based on an extraction from the free surface temporal series 1m in front of the structure (wave gauge WG-08). Every time the free surface up-crosses the still water level, it marks the beginning of a new wave, see Fig. 4.11. Therefore, the wave train is divided into several individual waves, each wave has a related time interval. With this information, an interval of the pressure signal is attributed to a singular wave event. Finally, the maximum value within this pressure interval is chosen as the wave pressure value.

In order to perform a survivability analysis, the most interesting events are those related to the most energetic waves during the whole wave train. However, experience has demonstrated that the natural selection of the single maximal pressure P_{max} is too simplistic and not representative of the whole stochastic process. To avoid this uncertainty, the average of the pressure maxima obtained from over two hundred fifty of the waves pressure $P_{1/250}$ is commonly used. As a matter of example and for consistency with the experiments, the duration of the simulations is $1000\,T_P$. It means that numerical and experimental results are obtained from 1000 wave individual events and the $P_{1/250}$ is calculated using the four highest pressure values recorded.

In order to increase even more confidence in the presented results, the present study adds further perspective to the statistical nature of the selected irregular sea states by computing five times the same configuration of significant wave height, peak period and water depth (H_S, T_P, h). In fact, for each of the 5 identical computations, only the

wave phase seed components are changed on a random basis. The pressure values in this section are made dimensionless by dividing them with the hydro-static component of the significant wave height ($\rho g H_S$).

4.4.1 Non-impulsive conditions

In this section two irregular sea-states, Irr01.10 and Irr13.01 as presented in Table 4.3, are reproduced and compared with the experiments. The studied configurations are referred to as non-impulsive and no wave breaking is expected. Presumably, the most energetic wave pressures on the structure will not exceed values of $2.5\rho g H_S$. Differences between both cases are the wave steepness and the orifice opening. The first subsection 4.4.1.1 also introduces a global convergence analysis by modifying the mesh and keeping the Courant number limitation. Then, the second subsection 4.4.1.2 compares the incompressible and compressible solvers. It is important to notice the fact that the experimental pressure signals for the non-impulsive conditions are modified using the filters explained in Sec. 4.2.2.

4.4.1.1 Irr01.10 : Global convergence

The configuration evaluated in the present section has a significant wave height $H_S = 0.26m$, a peak period $T_P = 3s$ and a water depth of $h = 3.5m$. Then, the physical time simulated is $1000\,T_P = 3000s$. A global convergence study is carried out in this section while comparing the numerical results using an incompressible solver with experiments. In fact, two spatial discretisation are used, the initial *coarse* mesh already presented and a so-called *refined* one. For this *refined* mesh, the initial spatial discretisation, presented in Sec. 4.2.3, is further refined by a factor of 3/4 with a new characteristic cell length $\Delta x = 0.075m$. Refined areas are modified accordingly. The temporal discretisation is also refined by keeping the same $maxCo = 0.4$ as in the original setup.

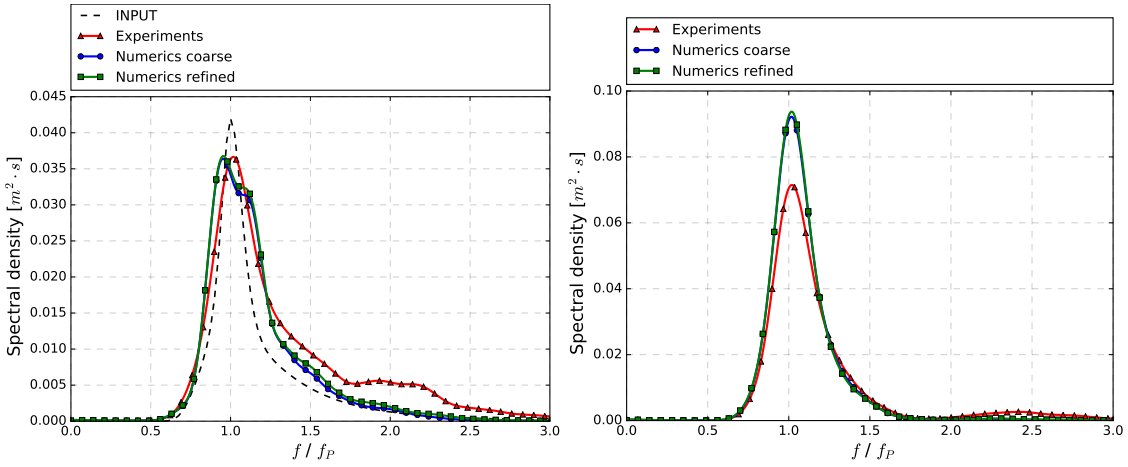

(a) $WG-04$ (b) $WG-08$

Figure 4.12: Spectrum over the horizontal slope (WG-04) and one meter in front of the OWC front wall (WG-08). Test conditions (Irr01.10): $H_S = 0.26m$, $T_P = 3s$ and $d_0/D = 0.6$.

First, Fig. 4.12 depicts free surface elevation spectra, one computed far from the structure over the horizontal bottom (WG-04, Fig. 4.12a) and the other one meter in front of the OWC front wall (WG-08, Fig. 4.12b). Fig. 4.12a compares the numerical results ob-

tained by using the two discretisations with the experimental one and the input spectrum for the relaxation zone.

On the one hand, the input spectrum is well captured by the numerics with a lower sharpening and distribution of energy towards the higher frequencies. However, these higher frequency waves are underestimated compared with the experiments. Finally, numerical results show a good convergence comparing the two obtained spectra, which are almost superposed.

On the other hand, computing the spectrum in the vicinity of the structure (see Fig. 4.12b), discrepancies between the peak frequency energies from the experiments and the numerics increase.

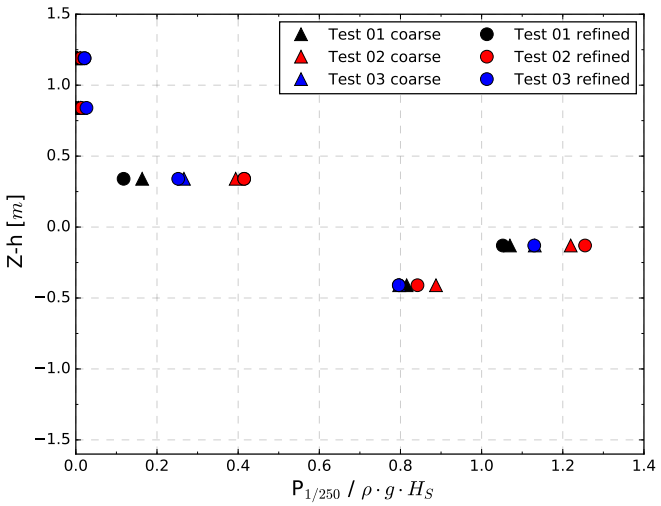

Figure 4.13: Convergence of wave pressure results ($P_{1/250}$) on the structure front wall for 3 exact similar configurations using 3 different wave phase random seeds. Test conditions (Irr01.10): $H_S = 0.26m$, $T_P = 3s$ and $d_0/D = 0.6$.

Next Fig. 4.13 presents dimensionless pressure values at five different elevations of the OWC front wall. The location with $Z - h = 0$ corresponds to the still water level, having two immersed pressure sensors (PS 01-02) and three above the water (PS 03-04-05). First, the obtained results using two discretisations are compared. Only three tests with different phase seeds, the same ones for both discretisations, are employed for this analysis due to the high computational costs when using the refined mesh. A very good convergence is observable between the coarse and the refined mesh, meaning that the coarse mesh is enough when looking for reliable solutions. Therefore, it is employed for the upcoming computations and analysis.

Finally, and as mentioned above, 2 additional computations were run with new seeds for the coarse mesh. This gives an overall of five similar tests with different phase seeds using the incompressible solver. The obtained results are compared in Fig. 4.14 with the experiments and the prediction using Goda's formulation [28] for caisson breakwaters. The numerical results are represented using the average value as a black square, the range corresponding to the minimum and maximum encountered over the 5 tested configurations. Comparing the results with the predictions using the pressure formulas, a relatively similar order of magnitude is encountered. The formulas proposed by Goda (1977) overpredict the values remaining on the security side, suggesting them as a good practice for design purposes. Observing the results from the experimental campaign, one can say the computed results have a good agreement from a quantitative point of view.

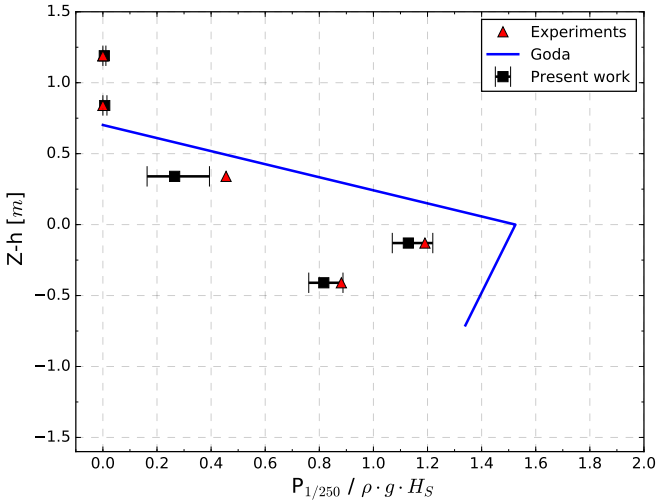

Figure 4.14: Maximal adimensional wave pressure ($P_{1/250}$) ranges over 5 random seeds on the structure front wall compared with the experimental values. Test conditions (Irr01.10): $H_S = 0.26m$, $T_P = 3s$ and $d_0/D = 0.4$.

The computed results depict the stochastic nature of the random sea with a non-negligible pressure range rather than a singular value. Furthermore, from a wider perspective, by taking into account all the statistics and analysis procedures to obtain such extreme and singular values, the authors are fairly optimistic about the computations.

4.4.1.2 Irr13.01 : Compressible and incompressible comparison

The configuration evaluated in the present section differs from the previous one by having lower wave steepnesses and a smaller opening of the orifice. The diameters ratio is $d_0/D = 0.4$ and the effects of air compressibility are expected to have a greater effect. In this section, the numerical results using incompressible and compressible solvers are compared with the experiments. During this work, the modified $k - \omega$ SST turbulence closure model is not yet implemented for the compressible solver, however, it is used in the incompressible simulations. This may cause higher damping of the wave heights when using the compressible solver.

From the wave gauge located over the horizontal plane (WG-04), Fig. 4.15a, the wave reflection caused by the structure reduces the spectrum peak and spreads energy onto smaller wave periods. The numerical differ from the experiments by keeping a sharper spectrum and slightly underestimating the energy-related to smaller and higher wave periods. On the other hand, the spectrum computed in the vicinity of the structure (Fig. 4.15b) shows a remarkably good agreement with the experiments. Nevertheless, the compressible solver slightly underestimates the energy compared with the incompressible solution and this is more visible when computing the pressure values. Both, away and close to the OWC, the compressible and the incompressible solver present very similar solutions.

Fig. 4.16 presents results of wave induced pressure exerted on the structure curtain wall using both incompressible and compressible solvers. As in the previous case, results are represented by their averaged values combined with a range of minimum and maximum values obtained over 5 identical computations. In this context, predictions using the Goda's formulation again over-predict the experimental values by an offset of $0.4\rho g H_S$. Both the incompressible and compressible solutions have a fairly good agreement with the

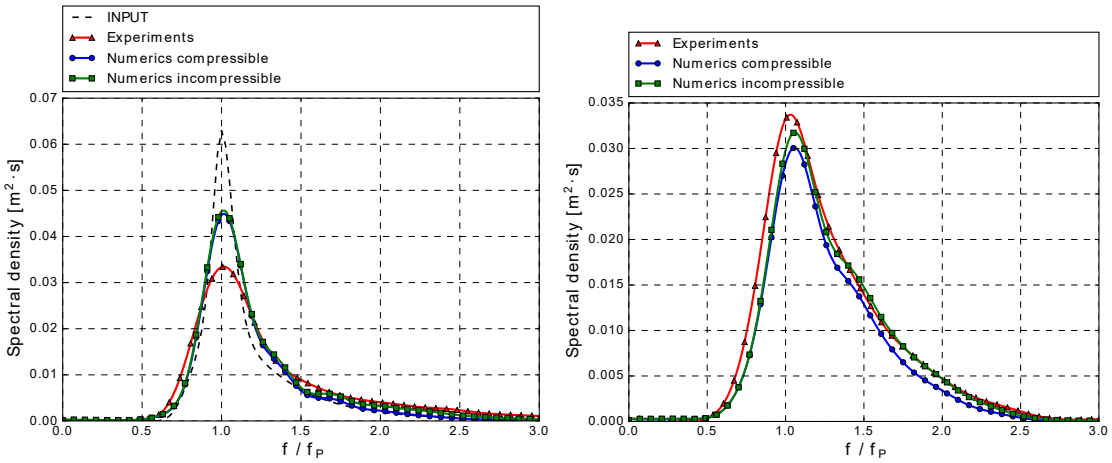

(a) $WG-04$ (b) $WG-08$

Figure 4.15: Spectrum over the horizontal slope (WG-04) and one meter in front of the OWC front wall (WG-08). Test conditions (Irr13.01): $H_S = 0.26m$, $T_P = 4.5s$ and $d_0/D = 0.4$.

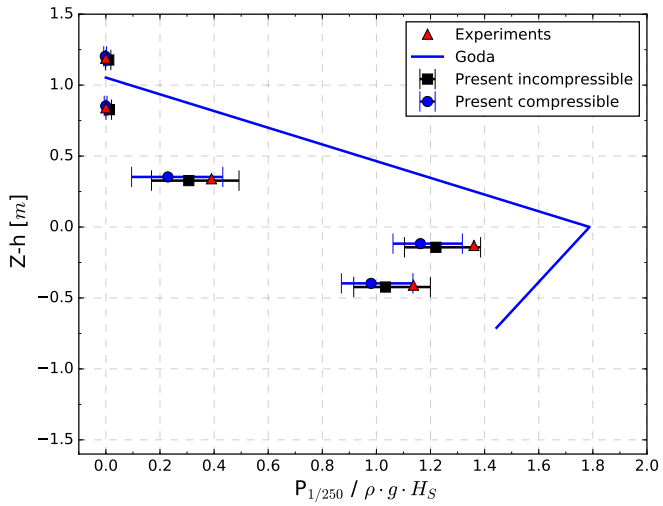

Figure 4.16: Comparison of compressible and incompressible maximal dimensionless wave pressure results ($P_{1/250}$) on the structure front wall evaluated over 5 computation with different phase random seeds. Test conditions (Irr13.01): $H_S = 0.26m$, $T_P = 4.5s$ and $d_0/D = 0.4$.

experiments. Again, it is also observable the statistical nature of the maximal pressure values related to, apparently, the same sea-state with ranges of pressure rather than a single value. Finally, the compressible and incompressible results have a similar trend, although, the compressible solver presents a higher diffusion, which was expected, and slightly reduces the pressure ranges. By to conclude, both incompressible and compressible solvers have demonstrated stability and accuracy when solving these two non-impulsive configurations and handling very large stochastic processes. Also, the interface compression method MULES has been once again validated for reproducing irregular waves interaction with a singular structure as the OWC.

4.4.2 Impulsive conditions

This section presents the results obtained using a new irregular sea state configuration (Irr11.07). During the experimental campaign, this configuration produced multiple wave breaking with highly energetic loads classified as impulsive. To study these conditions, previous analysis using the variable $P_{1/250}$ is less representative due to the high variability of the pressure maxima related to the most energetic impacts. Then, analysis is here limited to some selected singular events and their pressure signals. In fact, the presented computations were computationally very expensive due to high velocities, which significantly dropped the time steps. It was also necessary to increase the size of the free surface refinement region in order to maintain the interface within its limits owing to a much higher H_s value. Consequently, the physical time for this simulations was limited to $1000\,T_P/3 = 2000\,s$ keeping the same numbers of five different phase seeds tests as in previous sections.

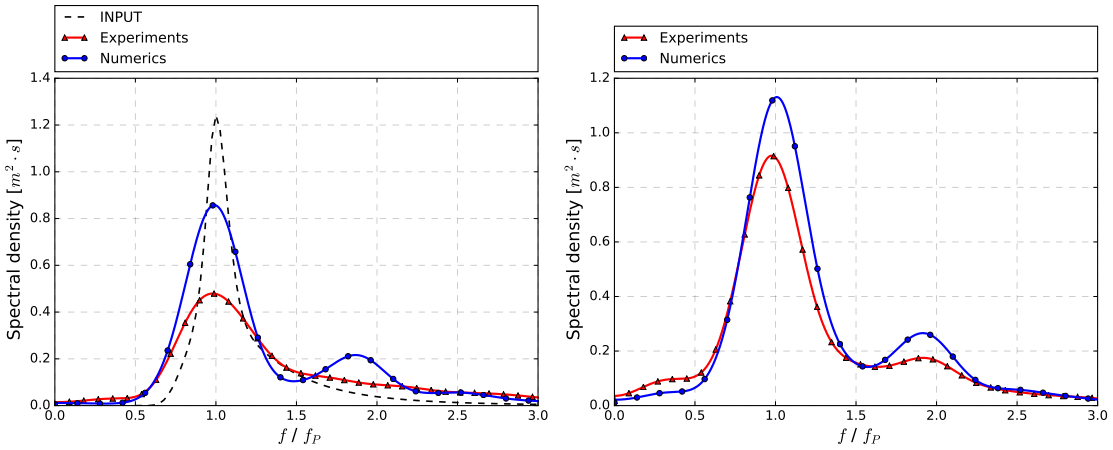

(a) $WG-04$ (b) $WG-08$

Figure 4.17: Spectrum over the horizontal slope (WG-04) and one meter in front of the OWC front wall (WG-08). Test conditions (Irr11.07): $H_S = 1m$, $T_P = 6s$ and $d_0/D = 0.4$.

Fig. 4.17 presents the spectrum over the horizontal slope (WG-04) and 1m in front of the structure (WG-08). It is important to notice here the lower physical time of the present simulations which may affect the sea state long term development. Hence, the spectrum computed over the horizontal slope (WG-04) presents visible discrepancies with the experiments. From Fig. 4.17a, a generalized overestimation of energy is noticeable from the numerical results compared with the experiments. The experimental higher frequencies $f > f_P$ are equally distributed compared to the numerical ones. Although these are present in the simulations, they are grouped around some characteristic values mainly around $f/f_P \approx 1.9$ and to some lower extent at $f/f_P \approx 2.5$. Also, some infragravitatory waves ($T > 30s$) can be identified from the experimental spectrum. These are underestimated in the numerics over the horizontal plane (WG-04, Fig. 4.17a). Regarding the spectrum in the vicinity of the structure (WG-08, Fig. 4.17b) a fairly good agreement is obtained here between the numerics and the experiments. Similar analyses as the ones observed for (WG-04) can be made with a general numerical overestimation of the energy related to the peak period and higher frequency waves. Here, the numeric presence of energy for long period waves has increased, however, the experimental values keep being underestimated. A preliminary observation can be extracted from this analysis, which points towards a lower presence of breaking effects due to a smaller representation of long-period waves. Finally,

the second peak located at $f/f_P \approx 1.9$ already identified for (WG-04, Fig. 4.17a) in the numerics is still present for (WG-08, Fig. 4.17b) but with its experimental counterpart. This gives some confidence in the fact that this is not a numerical artifact and more generally that the presented computations accurately represent the physical encountered phenomena.

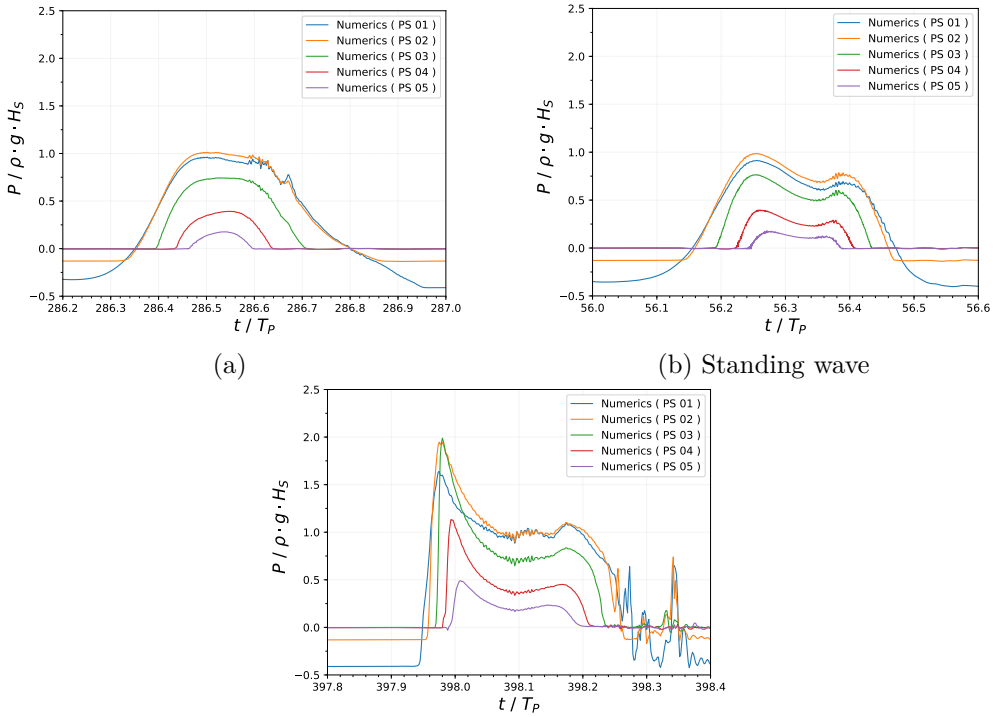

(a)

(b) Standing wave

(c) Slightly breaking wave

Figure 4.18: Numerical pressure signals recorded by wall pressure sensors (PS 01-05) on the exterior front wall for three distinct characteristic events. Test conditions (Irr11.07): $H_S = 1m$, $T_P = 6s$ and $d_0/D = 0.4$.

When looking at the wall pressure temporal series, three different characteristic types of events are mainly detected. These are presented in Figure 4.18. The first type of event (Fig. 4.18a) is the regular non-impulsive event, where pressure values are mostly related to the hydro-static pressure of the run-up and run-down process. The second type (Fig. 4.18a) can be classified as a pulsating load caused by a standing wave, identified using the PROVERS's [42] distinction. Although it seems very similar to the first type, here, two rebounds are visible and attributed to kinematic and hydro-static pressure ranges. The initial rebound is slightly more prominent compared to the second one as the wave momentum is being absorbed gradually with a rise time in the order of $t_r \approx 0.1T_p$. The last situation (Fig. 4.18c) can be classified as a slightly breaking wave. The numerical pressure sensors, which recorded the highest values, are in the vicinity of the still water level (PS 02-03) and, the upcoming analysis, will focus on these pressure series.

Experiments presented a fourth situation (Fig. 4.19), where the pressure peaks exceeded 10 times the significant wave height hydro-static pressure and an extreme event where it exceeded 20 times this value (Fig. 4.19b). These impacts are typical of plunging waves with rise time values around $t_r \approx 0.001T_P$. Unfortunately, not a single similar event could be numerically captured, where the maximal pressure values were always below 3 times the significant wave height pressure head. This further confirms the observation ex-

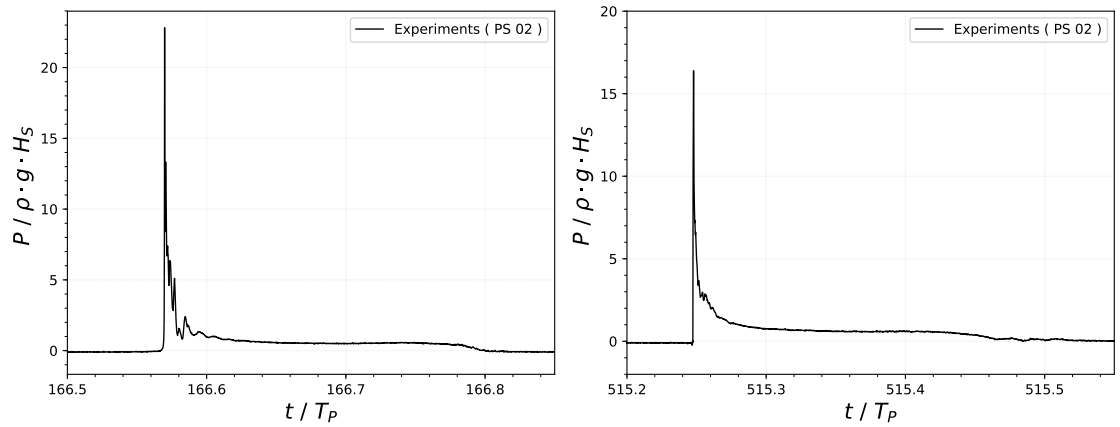

(a) (b)

Figure 4.19: Experimental pressure signal recorded by wall pressure transducer (PS 02) on the exterior front wall for two impulsive events. Test conditions (Irr11.07): $H_S = 1m$, $T_P = 6s$ and $d_0/D = 0.4$.

tracted from the computed spectrum meaning that not any real plunging breaker occurred during the simulations. The reason for this non-appearance of plunging breakers is still unknown although some ideas are plausible such as: the 3D configuration of the experiments leading to different behaviour of the chamber oscillations, the low discretisation adopted for a feasible computational costs objective, slight differences in the irregular sea state displacing the breaking point or a coarse definition of the interface by using MULES, instead of a geometric interface capturing method such as `isoAdvector`. Or a possible combination of all these phenomena can have an impact.

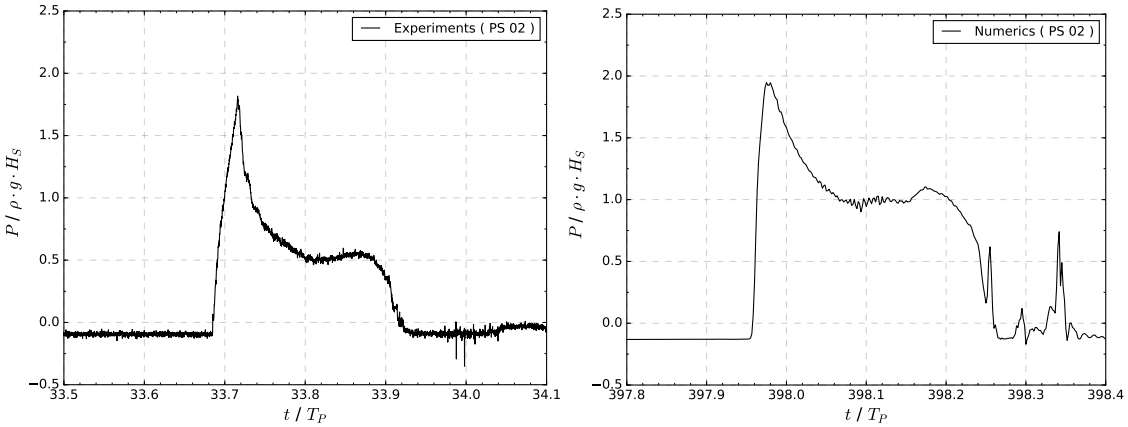

(a) Experiments (b) Numerics

Figure 4.20: Comparison of experimental and numerical pressure signal recorded by wall pressure transducer (PS 02) on the exterior front wall for a violent wave impact. Test conditions (Irr11.07): $H_S = 1m$, $T_P = 6s$ and $d_0/D = 0.4$.

Nevertheless, some lower order of magnitude violent wave-structure impacts are also observed on numerical pressure sensors as depicted in Figure 4.20. As presented above in Fig. 4.18c, these are classified as slightly breaking wave. Pressure signals related to this type of phenomenon reach values up to $2\rho g H_s$ and have an approximate rise time of $t_r \approx 0.01 T_P$, which is one order of magnitude higher than those from the extreme

impact loads. They present the classic double-peaked or 'church roof' shape related to the initial impact, deflection and reflection of the wave. Although these remain out of the impact events classification, the sudden pressure rise indicates an important role in the fluid deceleration in this wave interaction with the structure.

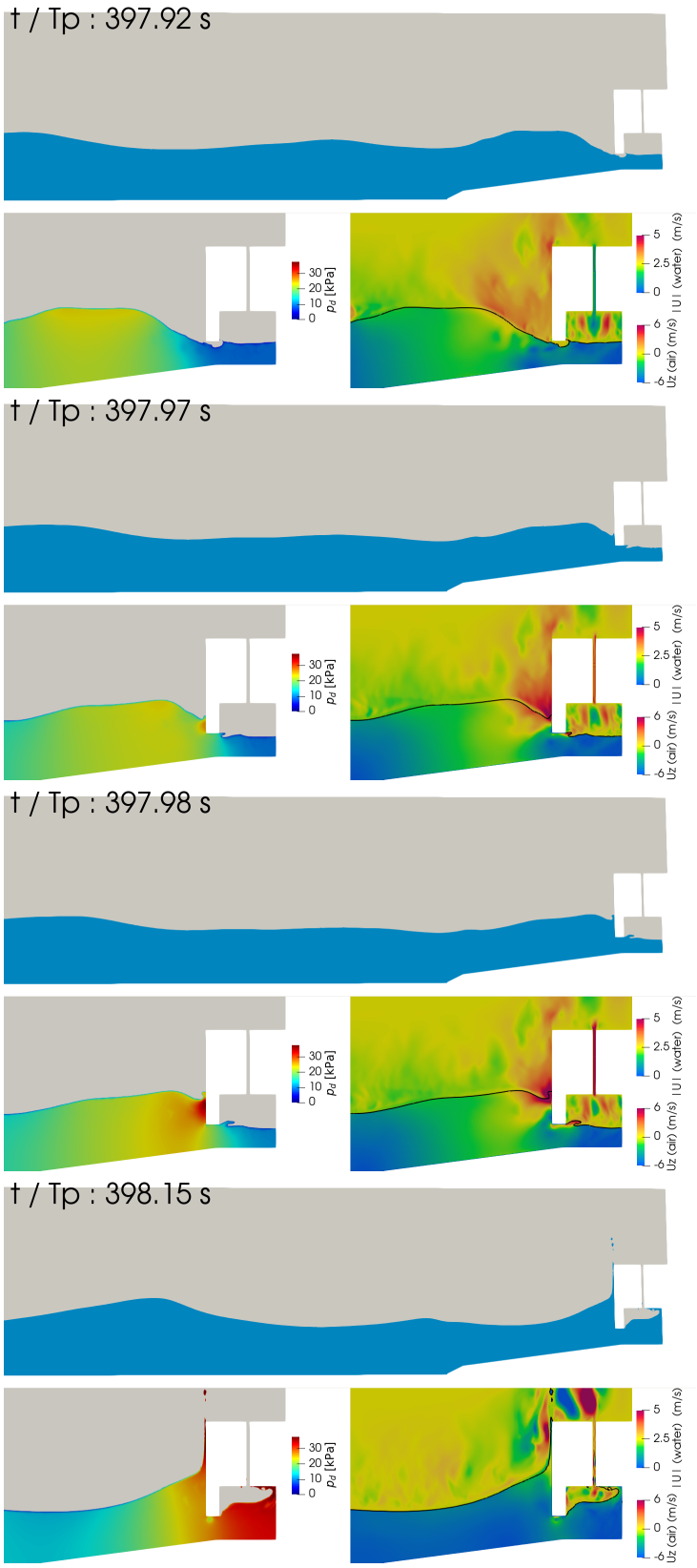

Figure 4.21: Snapshots of (top) water representation $\alpha > 0.5$, (bottom left) modified pressure for air p_d (kPa), (bottom right) velocity magnitude for water $|U|$ (m/s) and vertical velocity for air Uz (m/s), for four relevant instants during a wave impact, pressure signal Fig. 4.20

For a better understanding of the event related to the pressure signal from the last Figure 4.20, four relevant instants are presented in Fig. 4.21. In the first image ($t/T = 397.92$), a reflected and an incoming waves are superposed in front of the structure. The free surface inside the OWC chamber is falling sucking in air from the exterior. The bottom lip of the OWC curtain wall is not submerged. This is an unexpected situation and, in principle, should be avoided. Next ($t/T = 397.97$), the front wall bottom lip is exposed to a fluid impact originating two water tips, one traveling upwards the front wall and, a second one, towards the chamber rear wall. The velocities of these tips are non-negligible with values up to 5m/s. Regarding the modified pressure fields p_d, the incoming wave starts loading the bottom part of the front wall further accelerating the rising water tongue. At ($t/T = 397.98$), the pressure signal presented in Fig. 4.20 reaches its maximum and the incoming wave fully charges the vertical wall. The front wall is fully charged from the exterior side and remains only surrounded by the air from the interior side, causing an important bending moment. The chamber is now pushing the air outwards. In the last snapshot ($t/T = 398.15$), it is observable the deflection and reflection stage of the wave where the fluid is fully projected upwards forming some water independent small structures which are captured by the simulation. Under the front wall bottom lip, the already mentioned vortical structure again appears. Inside the chamber, the liquid undergoes a sloshing type situation leading to some impacts with the interior walls and fully compressing the air. These were also observed during the experimental campaign, see [18], and may cause unexpected damages if not addressed properly.

4.4.2.1 Identification of a possible broken wave impact case

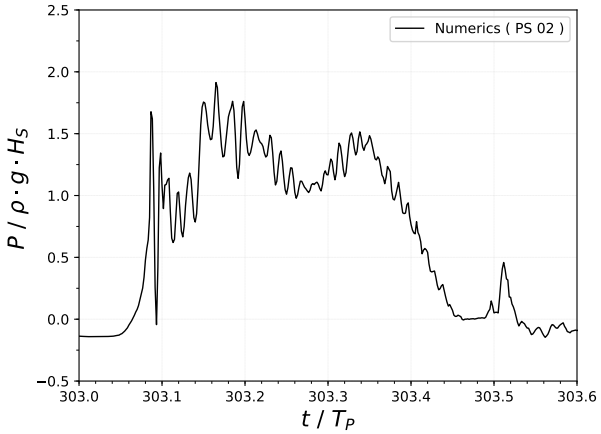

Figure 4.22: Numerical pressure signal recorded by a wall pressure sensor (PS 02) on the exterior front wall during a broken wave impact. Test conditions (Irr11.07): $H_S = 1m$, $T_P = 6s$ and $d_0/D = 0.4$.

Finally, a unique event occurred during the simulations which could be classified as a broken wave. The pressure signal for this situation is presented in Fig. 4.22. Studying the experimental pressure signal, no evidence of a similar event can be identified. This non-appearance of such a pressure signal in the experiments does not necessarily mean that no broken wave impact occurred. And a second perspective, e.g. imagery, would be necessary to corroborate this assertion. To analyse the pressure signal shown in Fig. 4.22, snapshots from the computation are presented in Fig. 4.23 and 4.24. From Fig. 4.23, observing the instant when the first pressure rise occurs ($t/T_p \approx 303.10$), it is clear that the wave has not collapsed yet onto the wall. The cause of this initial pressure peak (Fig. 4.22) is unclear.

However, it may be caused by a detached liquid structure that travels at abnormally high speed towards the wall as it is appreciable in this first figure. Secondly, a more coherent double-peaked signal is observed due to the deceleration, remount, deflection and reflection of the wave. Nevertheless, an oscillatory behaviour is observed during this process which is attributed to the compressibility of air-pockets, which are encapsulated between the wave impingement and the structure. This condition would be less likely to occur in reality, due to the possibility of air escaping through the transverse 3D direction.

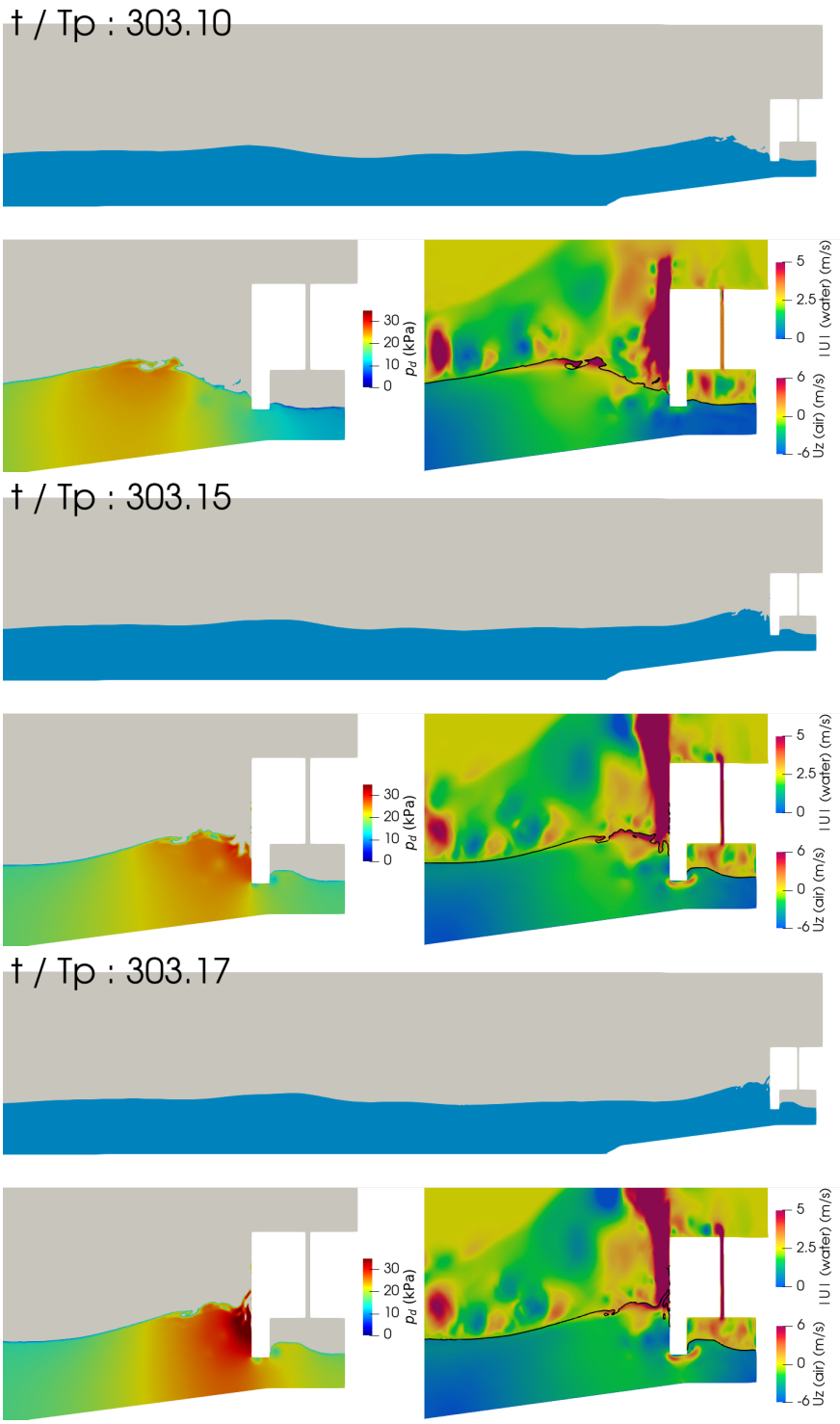

Figure 4.23: Snapshots of (top) water representation $\alpha > 0.5$, (bottom left) modified pressure for air p_d (kPa), (bottom right) velocity magnitude for water $|U|$ (m/s) and vertical velocity for air Uz (m/s), for four relevant instants during a broken wave impact, pressure signal Fig. 4.22

Again, in the last images of Fig. 4.23, broken wave interaction with the vertical wall is observable. Moreover, the vortical structures are here more present below the curtain bottom lip. Finally, Fig. 4.24 presents the whole breaking process of this wave in front

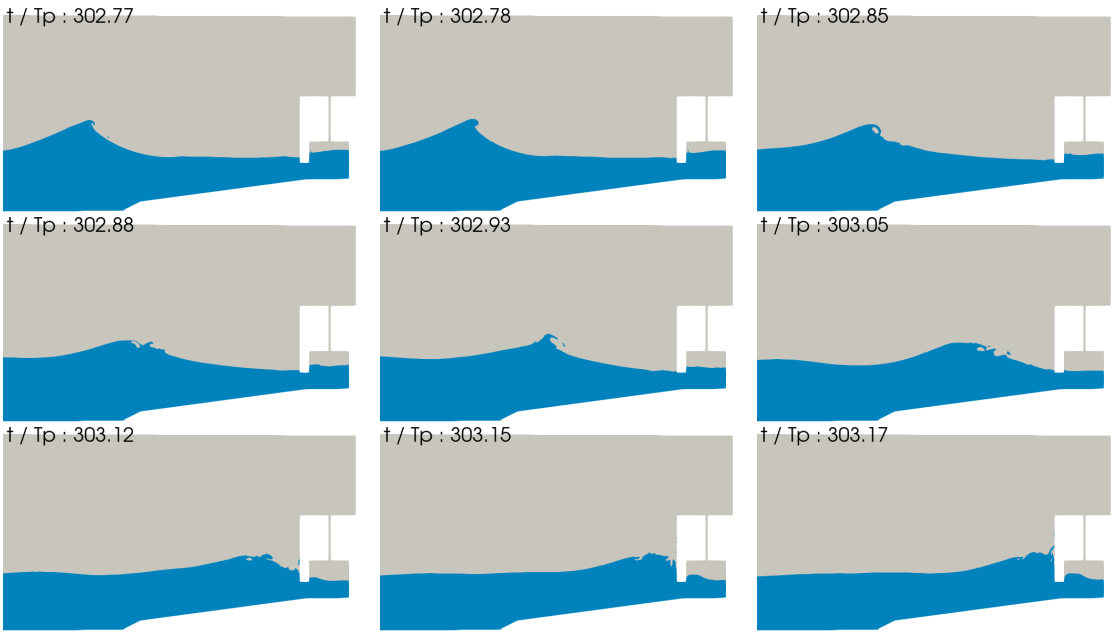

Figure 4.24: Snapshots of water representation $\alpha > 0.5$ during the breaking process from the pressure signal presented in Fig. 4.22 and the final process presented in Fig. 4.23

of the structure. This situation presents several detachments of liquid which are poorly represented due to a coarse spatial and temporal discretisation.

Chapter 5

Conclusion and perspectives

This research concerns the validation and analysis through a Computational Fluid Dynamics methodology for simulating coastal hydrodynamics using two-phase flows with time domain and finite volume discretisations. In this work, free surface waves generation, propagation and overturning have been studied and validated. Contributions have been made towards a numerical evaluation of wave loads exerted during a fluid impingement on a structure. This last chapter concludes the thesis and is divided into two Sections. The first section summarises the conclusions acquired from this work and the second one proposes suggestions for future work.

5.1 Conclusion

The results of this study have been assessed and discussed in the previous chapters. In the following, the most relevant conclusions are summarised.

Nonetheless, let us first outline the principal objectives. The final goal of the present work is to numerically evaluate the loads related to extreme waves impinging on an oscillating water column structure. For this, a gradual validation process starting from a simplistic to more complex configurations is chosen to extract robust and reliable conclusions. These configurations are distributed over three chapters and each chapter corresponds to a designed objective. They can be summarised as: an investigation of the mechanisms during an idealised fluid impact, an analysis of a controlled wave breaking impact using a solitary wave configuration and, finally, the reproduction of a realistic extreme sea-state acting on an OWC.

Investigation of the mechanisms during an idealised fluid impact

Thanks to the two-phase solver for incompressible fluids, `interFoam`, which is part of the `OpenFOAM` CFD library, we demonstrated in Sec. 2.2.1 the stability of the pressure impulse results under a fluid structure impulsive situation. A global convergence analysis has demonstrated the pressure impulse convergence towards an analytic solution proposed by M. Cooker *et al.* in 1990 [37]. On the other hand, a divergence of the pressure fields has been reported when decreasing the temporal and spatial discretisation under the incompressible assumption.

Using two-phase compressible solver, `compressibleInterFoam`, we demonstrated in Sec. 2.2.2 the ability to obtain accurate pressure solutions during an impulsive fluid-structure impact according to acoustic pressure theory. The present numerical implementation have proven convergence and stability on the pressure results. This section has arisen the necessity of using a CFL condition related to the fluid speed of sound to characterise a traveling pressure wave.

In Sec. 2.3 we have proven the possibility to model water compressing and expanding a gas phase (air) by using a 1D liquid piston configuration. Neglecting the compression terms in the liquid volume fraction equation has demonstrated to reduce the numeric diffusion in a compression and expansion air process. Next, in Sec. 2.4, we presented a tentative study of an aerated fluid impact. This part of the work can be classified as a perspective yet interesting and argumented approach. By using this configuration, we demonstrated the high influence of air during a fluid impact by lowering the fluid loads. Moreover, different time scales were observed during the impulsive loading process for air and water.

Analysis of a controlled wave breaking impact using a solitary wave

We validated the static boundary method in Sec. 3.1.3 for reproducing a Boussinesq solitary wave. Spatial discretisation has shown to be an important parameter for improving the generation and propagation of the solitary wave. On the other hand, temporal discretisation has demonstrated to be especially relevant for maintaining the wave amplitude during the propagation stage.

In Sec. 3.4 we demonstrated the pressure impulse convergence of the incompressible solver using a 2D solitary breaking wave ending in an air pocket or high-aerated impact. Again, this section confirmed that the pressure records are not a good measure to evaluate the convergence when using an incompressible solver. Moreover, Sec. 3.4, demonstrated

that in an aerated impulsive event using a 2D configuration and assuming the air as an incompressible fluid, the obtained pressure records result in erroneous loads. This is a consequence of the air phase not being capable of absorbing any impact energy and, thus, acting momentaneously as a solid rigid. These results are far from the reality observed in the literature, e.g., M. Hattori *et al.* in 1994 [38] and the experiments Kimmoun *et al.* 2009 [46], these last experiments being used as a validation cases in the present work.

From the author point of view, the incompressible assumption should be avoided when accurate pressure measurements are expected. To be more precise, our work aroused the necessity of a two-phase compressible model when one of these two conditions comes: the air is playing a role and/or the fluid-structure impact has an impulsive behaviour. This is the case for air-pocket and flip-through impacts.

In Sec. 3.5 we validated the compressible solver based on the free surface shape against the experimental results of O. Kimmoun, for reproducing a solitary wave overturning process using a 2D configuration. Moreover, it has demonstrated converged peak pressure results during an air-pocket or high-aerated impact. The pressure values at the impact moment are observed to agree with the experiments in a 2D air-pocket breaking wave situation.

On the other hand, the compressible solver has proven its ability to reproduce air compressibility effects by observing oscillations on the pressure signal related to the compression/expansion process of the air cavity. However, these have shown not to agree with the experiments due to the impossibility of the air to escape under the numerical 2D configuration which is not the case in the experiments.

We successfully simulated a flip-through or low-aerated impact using a two-phase compressible solver in a 2D configuration. Owing to the physics of waves impact, the pressure records showed a high degree of spatial and temporal scattering and the highest pressure recorded was by far on the low-aerated impact. This is in agreement with the literature (see G.N. Bullock [45] or M. Hattori [38]) and the experiments by O. Kimmoun. The obtained pressure peak magnitude is in agreement with the experimental pressure records. Pressure oscillations related to the compression and expansion of the air cavity have been numerically reported and are observed to agree with the experiments. Consequently, the flip-through or low-aerated impact can be simulated using a 2D configuration.

An air-pocket solitary wave impact using a compressible solver has been simulated using a 3D configuration, allowing the air to escape through a backlash during the compression phase. When the air was able to escape, the pressure oscillations were not appreciable after the impact. A good agreement with the experimental pressure records has been reported under these circumstances quantitatively and qualitatively.

We observed, for both the 2D and the 3D configurations of breaking wave impacts, a numerical underestimation of the quasi-hydrostatic pressure just after the impact.

For real-life configuration, a full 3D well-resolved compressible model would inevitably give the best results but this study also showed the associated computational costs. For the real design phase of coastal structure, a 3D well resolved model will probably not be feasible and 2D compressible approach may reveal sufficient in most cases.

In Sec. 3, we have demonstrated the suitability of the toolbox `OpenFOAM` for assessing fluid impulsive loads on a rigid solid wall. The great variability of maximum loads have been identified and the air entrapment has demonstrated to be a key parameter, as it has been reported before, both experimentally and numerically.

Reproduction of a realistic extreme sea-state acting on an OWC

In Chapter 4, we studied and compared with experimental data a real large scale oscillating water column facing nearshore sea state. Initially, the relaxation zone method has been evaluated for generating different irregular sea states using the JONSWAP spectrum based on various wave steepness $s = H_s/\lambda_p$. The results presented a good agreement compared with the input spectrum near the wave generation boundary (10 m away). The propagation of the sea state over 100 m was better conserved for the smaller steepness irregular configurations. Nevertheless, we have proven the possibility to generate a fairly accurate irregular free surface elevation time series following the linear theory using the relaxation zone method.

In Sec. 4.3, an oscillating water column affected by regular waves has been studied. Additionally, a Power Take-Off system mounted on the structure has been modelled using a porous medium approach. Two different configurations have been tested by changing the porous medium airflow resistance and a remarkable good agreement has been observed compared with the experiments. The highest resistances have shown that taking the air as incompressible leads to erroneous results and a compressible solver is again needed. Regarding the pressure gradient on the porous medium, the compressible solver has been able to accurately capture the compressibility effects observed experimentally.

In Sec. 4.4 we compared the numerical and experimental results of three different irregular sea states acting on an oscillating water column. The free surface elevation spectrum computed far from the structure and in front of the structure presented a fairly good agreement for the two irregular configurations classified as non-impulsive. We carried out a global sensitivity analysis for one irregular sea state configuration and converged results have been observed for the spectrum, and the extreme pressures ($p_{1/250}$) exerted on the OWC front wall on this non-impulsive configuration. Moreover, using another non-impulsive irregular sea-state configuration the compressible and the incompressible solvers have been compared and similar results are obtained, although, the compressible solver presented higher energy dissipation with lower extreme pressure ranges. The extreme pressure ($p_{1/250}$) exerted on the OWC front wall, highlighted the stochastic nature of the irregular sea-state presenting a range of solutions for apparently similar conditions. The extreme pressure experimental values have been successfully validated for two non-impulsive irregular sea state configurations.

Sec. 4.4.2 compared the numeric and experimental free surface and extreme pressures results during an irregular state with breaking waves. The computed spectrum have shown resemblances, however, the numeric results underestimated the long period wave energies. The most energetic wave impacts during the experiments were not observed in the simulations and may be caused by different reasons such as: the slight differences on the sea state parameters, the 3D effects during the experiments, the necessity of finer temporal and spatial resolution or a different methodology for modelling the free surface. A broken wave situation has been also observed numerically presenting air compressiblity effects due to entrapped air pockets. Finally, lower energetic impacts have been recorded numerically and are directly compared quantitatively and qualitatively to some experimental specific events. Extracting a final positive or negative conclusion from this impulsive loads section would need further investigation; however, promising results are observed and a general optimistic perspective can be extracted.

All the aforementioned results from Chapter 4 confirmed the necessity of high computational efforts to accurately reproduce the most interesting extreme conditions involving highly energetic breaking waves.

In this thesis we demonstrated the capabilities of the numerical toolbox `OpenFOAM` and, more specifically, the two-phase compressible solver dealing with fluid-structure impulsive events caused by water waves. We have proven the possibility to model both, large and small-scale phenomena, such as irregular waves, waves propagation and transformation, high deformation of the free surface during wave breaking and pressure related to violent wave impacts. On the other hand, the high costs of using high-fidelity models such as CFD in certain situations is reaffirmed by the present work. Finally, new perspectives of old problems, such as pressures related to breaking waves, have been explored and concluded the ability to mimic complex phenomenons that are hardly appreciable experimentally such as pressure waves, air inclusion or local pressure distribution.

5.2 Suggestions for future work

The present work has investigated the possibility to use a CFD code to evaluate the most violent wave impact loads on an oscillating water column. This effort can be of great use for the coastal engineering community and brings further confidence when using numerical approaches. Nevertheless, further work is still needed to advance into generic and accessible formulations, which capture the nature of breaking impacts and can be used during a coastal protection structure design process.

The presence of spurious velocities around the free surface has been repeatedly reported in the present work and the perspective to address this issue can also be interesting within the OpenFOAM community. From the authors knowledge, this has already been investigated by the naval engineering community [68] using the Ghost Fluid Method. However, this part of the code is not accessible and still has not been fully validated for the present situations

A great effort has been made in the present work to assess a situation close to reality. However, the lack of wave loads data recorded in a real breakwater has limited the scalability of these results. The possibility to carry such a campaign remains out of the numerical perspective from the author. Nevertheless, the difficulty of recording such localised and transient pressure records for the most violent impacts has been identified in this work.

On the one hand, the reproduction of some configurations presented in this work using a 3D geometry would give a further perspective and the possibility to limit the effects related to this assumption. Consequently, an important topic would be to accelerate and improve the performance of this kind of simulation. For this purpose, coupling techniques between potential and CFD codes would be a great candidate for evaluating the interaction of irregular sea states with coastal protection structure. Nevertheless, the time-scale related to breaking waves ($\approx \mu s$) is small compared to the generation of irregular waves ($\approx 10\,s$) and it is not clear if the coupling would improve the overall performance.

On the other hand, a perspective for future work would be to search for the possibility to include the effects of homogeneous mixtures of air and water, like foam, into a two phase model and evaluate the role of this during a wave impact. The work presented in Sec. 2.4 would be an interesting initial configuration for future investigations. Moreover, the inclusion of a model that takes into account the phase change of air condensation or water evaporation would give further insights into the mechanism acting on a fluid impact.

Bibliography

[1] Carling Hay, Eric Morrow, Robert Kopp, and Jerry Mitrovica. Probabilistic reanalysis of twentieth-century sea-level rise. *Nature*, 517:481–4, 01 2015.

[2] Luke Jackson and Svetlana Jevrejeva. A probabilistic approach to 21st century regional sea-level projections using rcp and high-end scenarios. *Global and Planetary Change*, 146, 10 2016.

[3] Alexander Nauels, Malte Meinshausen, Matthias Mengel, Katja Lorbacher, and Tom Wigley. Synthesizing long-term sea level rise projections-the magicc sea level model v2.0. *Geoscientific Model Development*, 10:2495–2524, 06 2017.

[4] Dewi Le Bars, Sybren Drijfhout, and Hylke de Vries. A high-end sea level rise probabilistic projection including rapid antarctic ice sheet mass loss. *Environmental Research Letters*, 122, 03 2017.

[5] Robert Kopp, Robert DeConto, Daniel Bader, Carling Hay, Radley Horton, Scott Kulp, Michael Oppenheimer, David Pollard, and Benjamin Strauss. Evolving understanding of antarctic ice-sheet physics and ambiguity in probabilistic sea-level projections: Ambiguity in sea-level projections. *Earth's Future*, 5, 12 2017.

[6] P. Quevauviller, P. Ciavola, and E. Garnier. *Xynthia, February 2010: Autopsy of a Foreseable Catastrophe*, chapter 3, pages 111–148. John Wiley & Sons, Ltd, 2017.

[7] Matthew D. K. Priestley, Joaquim G. Pinto, Helen F. Dacre, and Len C. Shaffrey. The role of cyclone clustering during the stormy winter of 2013/2014. *Weather*, 72(7):187–192, 2017.

[8] G.E. Jarlan. A perforated vertical wall breakwater. *Dock and Harbour Authority*, pages 394–398, 1961.

[9] Shigeo Takahashi, Katsutoshi Tanimoto, and Seiichi Miyanaga. Uplift wave forces due to compression of enclosed air layer and their similitude law. *Coastal Engineering in Japan*, 28(1):191–206, 1985.

[10] Shigeo Takahashi. Hydrodynamic characteristics of wave-power-extracting caisson breakwater. *Coastal Engineering Proceedings*, 1(21):185, Jan. 1988.

[11] Fang He and Zhenhua Huang. Using an oscillating water column structure to reduce wave reflection from a vertical wall. *Journal of Waterway, Port, Coastal, and Ocean Engineering*, 142(2):04015021, 2016.

[12] Diego Vicinanza, Enrico Di Lauro, Pasquale Contestabile, Corrado Gisonni, Javier L. Lara, and Inigo J. Losada. Review of innovative harbor breakwaters for wave-energy conversion. *Journal of Waterway, Port, Coastal, and Ocean Engineering*, 145(4):03119001, 2019.

[13] Frank Neumann and Izan Le Crom. Pico owc - the frog prince of wave energy? recent autonomous operational experience and plans for an open real-sea test centre in semi-controlled environment. In *9th European Wave and Tidal Energy Conference (EWTEC)*, 5-9 Sep. 2011 2011. Southampton, UK.

[14] António F.O. Falcão, António J.N.A. Sarmento, Luís M.C. Gato, and Ana Brito-Melo. The pico owc wave power plant: Its lifetime from conception to closure 1986–2018. *Applied Ocean Research*, 98:102104, 2020.

[15] Y. Torre-Enciso, I. Ortubia, L.I. López de Aguileta, and J. Marqués. Mutriku wave power plant: from the thinking out to the reality. In *8th European Wave and Tidal Energy Conference (EWTEC)*, September 2009. Uppsala, Sweden.

[16] I. Hashem, H.S. Abdel Hameed, and M.H. Mohamed. An axial turbine in an innovative oscillating water column (owc) device for sea-wave energy conversion. *Ocean Engineering*, 164:536–562, 2018.

[17] Encarnacion Medina-Lopez, William Allsop, Aggelos Dimakopoulos, and Tom Bruce. *Conjectures on the Failure of the OWC Breakwater at Mutriku*, pages 592–603. 2015.

[18] Krisna A. Pawitan, Diego Vicinanza, William Allsop, and Tom Bruce. Front wall and in-chamber impact loads on a breakwater-integrated oscillating water column. *Journal of Waterway, Port, Coastal, and Ocean Engineering*, 146(5):04020037, 2020.

[19] Thomas Stevenson. *The Design and Construction of Harbours: A Treatise on Maritime Engineering*. Cambridge Library Collection - Technology. Cambridge University Press, 1840.

[20] Sainflou G. Essai sur les digues maritimes verticales. Technical report, École nationale des Ponts et Chaussées, 1928.

[21] A. de Rouville, P. Besson, and P. Petry. *État actuel des études internationales sur les efforts dus aux lames*. 1938.

[22] T. von Karman. The impact on seaplane floats during landing. Technical report, National Advisory Committee for Aeronautics Technical, 1929.

[23] R A Bagnold. Interim report on wave-pressure research. (includes plates and photographs). *Journal of the Institution of Civil Engineers*, 12(7):202–226, 1939.

[24] Taizo Hayashi and Masataro Hattori. Pressure of the breaker against a vertical wall. *Coastal Engineering in Japan*, 1(1):25–37, 1958.

[25] D.F. Denny. Further experiments on wave pressures. *Journal of the Institution of Civil Engineers*, 35(4):330–345, 1951.

[26] Weggel J. Richard and W. Hall C. Maxwell. Experimental study of breaking wave pressures. In *Offshore Technology Conference*, April 1970. Houston, Texas.

[27] H. Mitsuyasu. Shock pressure of breaking wave. 1:17, Jan. 1966.

[28] Yoshimi Goda. *Random Seas and Design of Maritime Structures*. WORLD SCIENTIFIC, 3rd edition, 2010.

[29] Katsutoshi Tanimoto Shigeo Takahashi and Ken ichiro Shimosako. Experimental study of impulsive pressures on composite breakwaters -fundamental feature of impulsive pressure and the impulsive pressure coefficient. Technical report, 1993.

[30] M. S. Longuet-Higgins and E. D. Cokelet. The deformation of steep surface waves on water. i. a numerical method of computation. *Proceedings of the Royal Society of London. Series A, Mathematical and Physical Sciences*, 350(1660):1–26, 1976.

[31] Kjeldsen S.S. and D.S. Myrhaug. Breaking waves in deep water and resulting wave forces. In *Offshore Technology Conference*, 1979. Houston, Texas.

[32] W.J. Easson and C.A. Greated. Breaking wave forces and velocity fields. *Coastal Engineering*, 8(3):233–241, 1984.

[33] Michel K. Ochi and Chen-Han Tsai. Prediction of impact pressure induced by breaking waves on vertical cylinders in random seas. *Applied Ocean Research*, 6(3):157–165, 1984.

[34] E. S. Chan and W. K. Melville. Deep-water plunging wave pressures on a vertical plane wall. *Proceedings of the Royal Society of London. Series A, Mathematical and Physical Sciences*, 417(1852):95–131, 1988.

[35] P.A. Blackmore and P.J. Hewson. Experiments on full-scale wave impact pressures. *Coastal Engineering*, 8(4):331–346, 1984.

[36] M. J. Cooker and D. H. Peregrine. *Violent Water Motion at Breaking-Wave Impact*, pages 164–176. 1990.

[37] MJ Cooker and DH Peregrine. A model for breaking wave impact pressures. *Coastal Engineering Proceedings*, 1(22), 1990.

[38] Masataro Hattori, Atsushi Arami, and Takamasa Yui. Wave impact pressure on vertical walls under breaking waves of various types. *Coastal Engineering*, 22(1):79 – 114, 1994. Special Issue Vertical Breakwaters.

[39] H Oumeraci, P Klammer, and HW Partenscky. Classification of breaking wave loads on vertical structures. *Journal of waterway, port, coastal, and ocean engineering*, 119(4):381–397, 1993.

[40] Adam Randolph Crawford. *Measurement and Analysis of Wave Loading on a Full Scale Coastal Structure*. PhD thesis, 1999.

[41] Michael James Alexis Walkden. *Model wave impulse loads on caisson breakwater aeration, scale and structural response*. PhD thesis, 1999.

[42] Hocine Oumeraci, William Allsop, M. Groot, R. Crouch, J. Vrijling, Andreas Kortenhaus, and Hessel Voortman. Probabilistic design tools for vertical breakwaters. Technical report, 01 2001.

[43] G.N Bullock, A.R Crawford, P.J Hewson, M.J.A Walkden, and P.A.D Bird. The influence of air and scale on wave impact pressures. *Coastal Engineering*, 42(4):291 – 312, 2001.

[44] Geoffrey Bullock, Charlotte Obhrai, Gerald Müller, Guido Wolters, Howell Peregrine, and Henrik Bredmose. *Field and Laboratory Measurement of Wave Impacts*, pages 343–355. 2003.

[45] G.N. Bullock, C. Obhrai, D.H. Peregrine, and H. Bredmose. Violent breaking wave impacts. part 1: Results from large-scale regular wave tests on vertical and sloping walls. *Coastal Engineering*, 54(8):602 – 617, 2007.

[46] O. Kimmoun, Y.M. Scolan, and Š. Malenica. Fluid structure interactions occuring at a flexible vertical wall impacted by a breaking wave. In *The Nineteenth International Offshore and Polar Engineering Conference*. International Society of Offshore and Polar Engineers, 2009.

[47] Claudio Lugni, Massimo Miozzi, Maurizio Brocchini, and Odd Faltinsen. Evolution of the air-cavity during a depressurized wave impact. part i: The kinematic flow field[j]. *Physics of Fluids - PHYS FLUIDS*, 22, 05 2010.

[48] C. Lugni, M. Brocchini, and O. M. Faltinsen. Evolution of the air cavity during a depressurized wave impact. ii. the dynamic field. *Physics of Fluids*, 22(5):056102, 2010.

[49] Giovanni Cuomo, William Allsop, Tom Bruce, and Jonathan Pearson. Breaking wave loads at vertical seawalls and breakwaters. *Coastal Engineering - COAST ENG*, 57:424–439, 04 2010.

[50] Bas Hofland, Mirek Kaminski, and Guido Wolters. Large scale wave impacts on a vertical wall. *Coastal Engineering Proceedings*, 1(32):structures–15, 2011.

[51] Atle Jensen. Solitary wave impact on a vertical wall. *European Journal of Mechanics - B/Fluids*, 73, 05 2018.

[52] T. Mai, C. Mai, A. Raby, and D.M. Greaves. Aeration effects on water-structure impacts: Part 2. wave impacts on a truncated vertical wall. *Ocean Engineering*, 186:106053, 2019.

[53] Ge Wei, James T. Kirby, Stephan T. Grilli, and Ravishankar Subramanya. A fully nonlinear boussinesq model for surface waves. part 1. highly nonlinear unsteady waves. *Journal of Fluid Mechanics*, 294:71–92, 1995.

[54] Patrick J. Lynett and Philip L.-F. Liu. A two-dimensional, depth-integrated model for internal wave propagation over variable bathymetry. *Wave Motion*, 36(3):221–240, 2002.

[55] Marcel Zijlema, Guus Stelling, and Pieter Smit. Swash: An operational public domain code for simulating wave fields and rapidly varied flows in coastal waters. *Coastal Engineering*, 58(10):992–1012, 2011.

[56] Sheguang Zhang, Dick K. P. Yue, and Katsuji Tanizawa. Simulation of plunging wave impact on a vertical wall. *Journal of Fluid Mechanics*, 327:221–254, 1996.

[57] Bingyue Song and Chongwei Zhang. Boundary element study of wave impact on a vertical wall with air entrapment. *Engineering Analysis with Boundary Elements*, 90:26–38, 2018.

[58] N. de Divitiis and L.M. de Socio. Impact of floats on water. *Journal of Fluid Mechanics*, 471:365–379, 2002.

[59] G. D. Xu, W. Y. Duan, and G. X. Wu. Simulation of water entry of a wedge through free fall in three degrees of freedom. *Proceedings of the Royal Society A: Mathematical, Physical and Engineering Sciences*, 466(2120):2219–2239, 2010.

[60] Edin Berberović, Nils P. van Hinsberg, Suad Jakirlić, Ilia V. Roisman, and Cameron Tropea. Drop impact onto a liquid layer of finite thickness: Dynamics of the cavity evolution. *Phys. Rev. E*, 79:036306, Mar 2009.

[61] H. G. Weller, G. Tabor, H. Jasak, and C. Fureby. A tensorial approach to computational continuum mechanics using object-oriented techniques. *Computers in Physics*, 12(6):620–631, 1998.

[62] Christian Windt, Josh Davidson, Pál Schmitt, and John V. Ringwood. On the assessment of numerical wave makers in cfd simulations. *Journal of Marine Science and Engineering*, 7(2), 2019.

[63] Niels G. Jacobsen, David R. Fuhrman, and Jørgen Fredsøe. A wave generation toolbox for the open-source cfd library: Openfoam®. *International Journal for Numerical Methods in Fluids*, 70(9):1073–1088, 2012.

[64] Pablo Higuera, Javier L. Lara, and Inigo J. Losada. Realistic wave generation and active wave absorption for navier–stokes models: Application to openfoam®. *Coastal Engineering*, 71:102 – 118, 2013.

[65] Paweł A. Wroniszewski, Joris C.G. Verschaeve, and Geir K. Pedersen. Benchmarking of navier–stokes codes for free surface simulations by means of a solitary wave. *Coastal Engineering*, 91:1 – 17, 2014.

[66] Bo T. Paulsen, H. Bredmose, H. B. Bingham, and N. G. Jacobsen. Forcing of a bottom-mounted circular cylinder by steep regular water waves at finite depth. *Journal of Fluid Mechanics*, 755:1–34, 2014.

[67] S. Hysing. A new implicit surface tension implementation for interfacial flows. *International Journal for Numerical Methods in Fluids*, 51(6):659–672, 2006.

[68] V. Vukčević, H. Jasak, and Š. Malenica. Decomposition model for naval hydrodynamic applications, part i: Computational method. *Ocean Engineering*, 121:37 – 46, 2016.

[69] Bjarke Eltard Larsen, David R. Fuhrman, and Johan Roenby. Performance of interfoam on the simulation of progressive waves, 2018.

[70] Niels Gjøl Jacobsen, Jørgen Fredsøe, and Jacob Hjelmager Jensen. Formation and development of a breaker bar under regular waves. part 1: Model description and hydrodynamics. *Coastal Engineering*, 88:182–193, 2014.

[71] Guido Lupieri and Giorgio Contento. Numerical simulations of 2-d steady and unsteady breaking waves. *Ocean Engineering*, 106:298–316, 2015.

[72] Brecht Devolder. *Hydrodynamic Modelling of Wave Energy Converter Arrays*. PhD thesis, Ghent University, 2017.

[73] Bjarke Eltard Larsen and David R. Fuhrman. On the over-production of turbulence beneath surface waves in reynolds-averaged navier–stokes models. *Journal of Fluid Mechanics*, 853:419–460, 2018.

[74] Z. H. Ma, D. M. Causon, L. Qian, C. G. Mingham, H. B. Gu, and P. Martínez Ferrer. A compressible multiphase flow model for violent aerated wave impact problems. *Proceedings of the Royal Society A: Mathematical, Physical and Engineering Sciences*, 470(2172):20140542, 2014.

[75] Rik Wemmenhove, Roel Luppes, Arthur E.P. Veldman, and Tim Bunnik. Numerical simulation of hydrodynamic wave loading by a compressible two-phase flow method. *Computers & Fluids*, 114:218 – 231, 2015.

[76] Inno Gatin, Shengnan Liu, Vuko Vukčević, and Hrvoje Jasak. Finite volume method for general compressible naval hydrodynamics. *Ocean Engineering*, 196:106773, 2020.

[77] Shengnan Liu, Inno Gatin, Charlotte Obhrai, Muk Chen Ong, and Hrvoje Jasak. Cfd simulations of violent breaking wave impacts on a vertical wall using a two-phase compressible solver. *Coastal Engineering*, 154:103564, 2019.

[78] PM Guilcher, G Oger, L Brosset, E Jacquin, N Grenier, and D Le Touzé. Simulation of liquid impacts with a two-phase parallel SPH model. In *Proceedings of 20th International Offshore and Polar Engineering Conference, June 20-26, Bejing, China*, 2010.

[79] Jean-Philippe Braeunig, L. Brosset, Frédéric Dias, and Jean-Michel Ghidaglia. Phenomenological study of liquid impacts through 2d compressible two-fluid numerical simulations. In *Proceedings of the Nineteenth (2009) International Offshore and Polar Engineering Conference*, pages 21–29, Osaka, Japan, June 2009. The International Society of Offshore and Polar Engineers (ISOPE).

[80] S. Marrone, A. Colagrossi, A. Di Mascio, and D. Le Touzé. Prediction of energy losses in water impacts using incompressible and weakly compressible models. *Journal of Fluids and Structures*, 54:802–822, 2015.

[81] Salvatore Marrone, Andrea Colagrossi, Andrea Di Mascio, and David Le Touzé. Analysis of free-surface flows through energy considerations: Single-phase versus two-phase modeling. *Phys. Rev. E*, 93:053113, May 2016.

[82] Xuezhou Lu, Jean-Marc Cherfils, Grégory Pinon, Elie Rivoalen, Olivier Kimmoun, and Jérôme Brossard. Sph numerical computations of wave impact onto a vertical wall with experimental comparisons. *Comptes Rendus. Mécanique*, 349(1):117–143, 2021.

[83] Jeffrey Lin, Carlo Scalo, and Lambertus Hesselink. Bulk viscosity model for near-equilibrium acoustic wave attenuation, 2017.

[84] Hrvoje Jasak. *Error Analysis and Estimation for the Finite Volume Method With Applications to Fluid Flows*. PhD thesis, 1996.

[85] Suraj S Deshpande, Lakshman Anumolu, and Mario F Trujillo. Evaluating the performance of the two-phase flow solver interFoam. *Computational Science & Discovery*, 5(1):014016, nov 2012.

[86] S. Márquez Damián. *An Extended Mixture Model for the Simultaneous Treatment of Short and Long Scale Interfaces*. PhD thesis, 03 2013.

[87] Johan Roenby, Henrik Bredmose, and Hrvoje Jasak. A computational method for sharp interface advection. *Open Science*, 3(11):160405, 2016.

[88] Johan Roenby, Henrik Bredmose, and Hrvoje Jasak. *IsoAdvector: Geometric VOF on general meshes*. 01 2018.

[89] Henning Scheufler and Johan Roenby. Accurate and efficient surface reconstruction from volume fraction data on general meshes. *Journal of Computational Physics*, 383:1 – 23, 2019.

[90] H. Rusche. *Computational fluid dynamics of dispersed two-phase flows at high phase fractions*. PhD thesis, Imperial College London (University of London), 2003.

[91] Luca Mangani Fadl Moukalled and Marwan Darwish. *The Finite Volume Method in Computational Fluid Dynamics: An Advanced Introduction with OpenFOAM® and Matlab*. Springer International Publishing, 2016.

[92] Tobias Holzmann. *Mathematics, Numerics, Derivations and OpenFOAM®*. 11 2019.

[93] Openfoam user guide. https://www.openfoam.com/documentation/user-guide/.

[94] Openfoamwiki. http://http://openfoamwiki.net/.

[95] P. Higuera. *Application of Computational Fluid Dynamics to Wave Action on Structures*. PhD thesis, School of Civil Engineering, University of Cantabria, Cantabria, Spain, 2015.

[96] C. M. Rhie and W. L. Chow. Numerical study of the turbulent flow past an airfoil with trailing edge separation. *AIAA Journal*, 21(11):1525–1532, 1983.

[97] S.T. Miller, H. Jasak, D.A. Boger, E.G. Paterson, and A. Nedungadi. A pressure-based, compressible, two-phase flow finite volume method for underwater explosions. *Computers & Fluids*, 87:132–143, 2013. USNCCM Moving Boundaries.

[98] R. H. Cole. *Underwater explosions.* Princeton,Princeton Univ. Press,, 1948.

[99] R. I. Issa. Solution of the implicitly discretised fluid flow equations by operator-splitting. *Journal of Computational Physics*, 62:40–65, January 1986.

[100] R.I Issa, A.D Gosman, and A.P Watkins. The computation of compressible and incompressible recirculating flows by a non-iterative implicit scheme. *Journal of Computational Physics*, 62(1):66–82, 1986.

[101] S.V. Patankar. *Numerical Heat Transfer and Fluid Flow*. Taylor & Francis, Boca Raton, 1980.

[102] Hemming A. Schäffer and Gert Klopman. Review of multidirectional active wave absorption methods. *Journal of Waterway, Port, Coastal, and Ocean Engineering*, 126(2):88–97, 2000.

[103] Takumi Ohyama and Kazuo Nadaoka. Development of a numerical wave tank for analysis of nonlinear and irregular wave field. *Fluid Dynamics Research*, 8(5):231–251, 1991.

[104] David R. Fuhrman, Per A. Madsen, and Harry B. Bingham. Numerical simulation of lowest-order short-crested wave instabilities. *Journal of Fluid Mechanics*, 563:415–441, 2006.

[105] Mark J. Cooker and D. H. Peregrine. Pressure-impulse theory for liquid impact problems. *Journal of Fluid Mechanics*, 297:193–214, 1995.

[106] Marc Batlle Martin, Grégory Pinon, Julien Reveillon, and Olivier Kimmoun. Computations of soliton impact onto a vertical wall: Comparing incompressible and compressible assumption with experimental validation. *Coastal Engineering*, 164:103817, 2021.

[107] Joseph-Louis Lagrange. *Mécanique Analytique*, volume 1. 1811.

[108] *On the Effect of Phase Transition On Impact Pressures Due to Sloshing*, volume All Days of *International Ocean and Polar Engineering Conference*, 06 2010. ISOPE-I-10-182.

[109] *Generalized Bagnold Model*, International Ocean and Polar Engineering Conference, 06 2013. ISOPE-I-13-331.

[110] Joseph Boussinesq. Théorie des ondes et des remous qui se propagent le long d'un canal rectangulaire horizontal, en communiquant au liquide contenu dans ce canal des vitesses sensiblement pareilles de la surface au fond. *J. Math. Pures Appl.*, 17(2):55–108, 1872.

[111] Jiin-Jen Lee, James E. Skjelbreia, and Fredric Raichlen. Measurement of velocities in solitary waves. *Journal of the Waterway, Port, Coastal and Ocean Division*, 108(2):200–218, 1982.

[112] Bjarke Eltard Larsen, David R. Fuhrman, and Johan Roenby. Performance of interfoam on the simulation of progressive waves. *Coastal Engineering Journal*, 61(3):380–400, 2019.

[113] B. Sumer, P. Jensen, L. Sørensen, J. Fredsøe, P. Liu, and S. Carstensen. Coherent structures in wave boundary layers. part 2. solitary motion. *Journal of Fluid Mechanics*, 646:207 – 231, 03 2010.

[114] P. Higuera, P. L.-F. Liu, C. Lin, W.-Y. Wong, and M.-J. Kao. Laboratory-scale swash flows generated by a non-breaking solitary wave on a steep slope. *Journal of Fluid Mechanics*, 847:186–227, 2018.

[115] Hermann Schlichting and Klaus Gersten. *Boundary-layer theory*. 1979.

[116] O Kimmoun, A Ratouis, and L Brosset. Sloshing and scaling: experimental study in a wave canal at two different scales. In *Proceedings of 20th International Offshore and Polar Engineering Conference, June*, pages 20–26, 2010.

[117] Marianne M. Francois, Sharen J. Cummins, Edward D. Dendy, Douglas B. Kothe, James M. Sicilian, and Matthew W. Williams. A balanced-force algorithm for continuous and sharp interfacial surface tension models within a volume tracking framework. *Journal of Computational Physics*, 213(1):141 – 173, 2006.

[118] William Allsop, Tom Bruce, John Alderson, Vincenzo Ferrante, Viviana Russo, Diego Vicinanza, and Matthias Kudella. Large scale tests on a generalised oscillating water column wave energy converter. 08 2014.

[119] K Hasselmann, T.P. Barnett, E. Bouws, H. Carlson, D.E. Cartwright, K. Enke, J.A. Ewing, H. Gienapp, D.E. Hasselmann, P. Kruseman, A. Meerburg, P. Müller, D.J. Olbers, K. Richter, W. Sell, and H. Walden. Measurements of wind-wave growth and swell decay during the joint north sea wave project (jonswap), 1973.

[120] P. Welch. The use of fast fourier transform for the estimation of power spectra: A method based on time averaging over short, modified periodograms. *IEEE Transactions on Audio and Electroacoustics*, 15(2):70–73, 1967.

[121] Giovanni Battista Rossi, Francesco Crenna, Vincenzo Piscopo, and Antonio Scamardella. Comparison of spectrum estimation methods for the accurate evaluation of sea state parameters. *Sensors*, 20(5), 2020.

[122] Arthur Schuster. On the investigation of hidden periodicities with application to a supposed 26 day period of meteorological phenomena. *Terrestrial Magnetism*, 3(1):13–41, 1898.

[123] Antonino Viviano, Stefania Naty, Enrico Foti, Tom Bruce, William Allsop, and Diego Vicinanza. Large-scale experiments on the behaviour of a generalised oscillating water column under random waves. *Renewable Energy*, 99:875–887, 2016.

[124] Antonino Viviano, Rosaria Ester Musumeci, Diego Vicinanza, and Enrico Foti. Pressures induced by regular waves on a large scale owc. *Coastal Engineering*, 152:103528, 2019.

[125] Krisna A. Pawitan, Aggelos S. Dimakopoulos, Diego Vicinanza, William Allsop, and Tom Bruce. A loading model for an owc caisson based upon large-scale measurements. *Coastal Engineering*, 145:1–20, 2019.

[126] Aggelos Dimakopoulos, Mark Cooker, Encarni Medina-Lopez, Daniele Longo, and Romain Pinguet. Flow characterisation and numerical modelling of owc wave energy converters. 09 2015.

[127] W. Sheng, Florent Thiebaut, Marie Babuchon, Joseph Brooks, Anthony Lewis, and Raymond Alcorn. Investigation to air compressibility of oscillating water column wave energy converters. volume 8, 06 2013.

[128] S. Anand, V. Jayashankar, S. Nagata, K. Toyota, M. Takao, and T. Setoguchi. Performance estimation of bi-directional turbines in wave energy plants. *Journal of Thermal Science*, 2007.

[129] D.S. Miller. *Internal Flow Systems*. 1978.

[130] M. Batlle Martin, G. Pinon, and J. Reveillon. Numerical assessment of wave induced loads on an oscillating water column carapace. In Taylor and Francis Group, editors, *Developments in Renewable Energies Offshore: Proceedings of the 4th International Conference on Renewable Energies Offshore*, 2020.

Computations of extreme wave impact events on wave energy converter attached to coastal protection structures

Keywords: Breaking waves, Fluid compressibility, Impact, Numerical simulation, OpenFOAM, Oscillating water column, Wave hydrodynamics

Abstract The present work aims to describe and evaluate the loads exerted by severe breaking waves onto coastal protection structures. To carry on with this investigation, the numerical tool-box OpenFOAM is employed and the problematic is regarded from different perspectives. First, the physics of an idealised impulsive event between a fluid and a solid is investigated using different configurations. The associated simulations are designed to study the role of air during these academic impact configurations. Secondly, a solitary wave is used to evaluate the performance of the solver to reproduce realistic wave breaking onto a vertical wall and evaluate the related impact pressure records. The computed results are validated against experimental data previously obtained at IRPHE, Marseille (France). Finally, an irregular sea state is simulated using large spatial and temporal scales to evaluate the induced wave loads on an oscillating water column structure. These simulations are compared and validated with experimental results obtained in the large flume tank (GWK) at Hanover (Germany).

Résumé Ce travail a pour objectif de décrire et évaluer les impacts de vagues extrêmes sur des structures de protection côtière. Dans le cadre de ces recherches, la suite logicielle OpenFOAM est utilisée et la problématique est étudiée suivant différentes perspectives. Dans un premier temps, la physique d'un événement impulsif idéalisé entre un fluide et un solide est étudiée en utilisant différentes configurations. Les simulations associées sont conçues pour étudier le rôle de l'air durant ces configurations d'impact académiques. Deuxièmement, une vague solitaire est utilisée pour évaluer la performance du solveur afin de reproduire des impacts de vague réalistes sur un mur vertical et d'évaluer les pressions d'impact associées. Les résultats numériques sont validés à l'aide de données expérimentales obtenues antérieurement à l'IRPHE, Marseille (France) . Enfin, un état de mer irrégulier est simulé en utilisant une large gamme d'échelles spatiales et temporelles afin d'évaluer les chargement induits par ces vagues sur une structure de colonne d'eau oscillante. Ces simulations sont comparées et validées avec des résultats expérimentaux obtenus dans le grand canal à houle GWK de Hannovre (Allemagne).